Calhoun: The NPS Institutional Archive

DSpace Repository

Theses and Dissertations | 1. Thesis and Dissertation Collection, all items

2001-09

Multi-block parallel Navier-Stokes simulation of unsteady wind tunnel and ground interference effects

Castro, Breno Moura

http://hdl.handle.net/10945/9726

This publication is a work of the U.S. Government as defined in Title 17, United States Code, Section 101. Copyright protection is not available for this work in the United States.

Downloaded from NPS Archive: Calhoun

Calhoun is the Naval Postgraduate School's public access digital repository for research materials and institutional publications created by the NPS community. Calhoun is named for Professor of Mathematics Guy K. Calhoun, NPS's first appointed -- and published -- scholarly author.

Dudley Knox Library / Naval Postgraduate School
411 Dyer Road / 1 University Circle
Monterey, California USA 93943

http://www.nps.edu/library

NAVAL POSTGRADUATE SCHOOL
Monterey, California

DISSERTATION

MULTI-BLOCK PARALLEL NAVIER-STOKES SIMULATION OF UNSTEADY WIND TUNNEL AND GROUND INTERFERENCE EFFECTS

by

Breno Moura Castro

September 2001

Dissertation Supervisor: Max F. Platzer

Approved for public release; distribution is unlimited.

REPORT DOCUMENTATION PAGE

Form Approved OMB No. 0704-0188

Public reporting burden for this collection of information is estimated to average 1 hour per response, including the time for reviewing instruction, searching existing data sources, gathering and maintaining the data needed, and completing and reviewing the collection of information. Send comments regarding this burden estimate or any other aspect of this collection of information, including suggestions for reducing this burden, to Washington Headquarters Services, Directorate for Information Operations and Reports, 1215 Jefferson Davis Highway, Suite 1204, Arlington, Va 22202-4302, and to the Office of Management and Budget, Paperwork Reduction Project (0704-0188) Washington DC 20503.

1. AGENCY USE ONLY (*Leave blank*)	2. REPORT DATE September 2001	3. REPORT TYPE AND DATES COVERED Doctor's Dissertation

4. TITLE AND SUBTITLE
MULTI-BLOCK PARALLEL NAVIER-STOKES SIMULATION OF UNSTEADY WIND TUNNEL AND GROUND INTERFERENCE EFFECTS

5. FUNDING NUMBERS

6. AUTHORS Breno Moura Castro

7. PERFORMING ORGANIZATION NAME(S) AND ADDRESS(ES)
Naval Postgraduate School
Monterey CA 93943-5000

8. PERFORMING ORGANIZATION REPORT NUMBER

9. SPONSORING/MONITORING AGENCY NAME(S) AND ADDRESS(ES)

10. SPONSORING/MONITORING AGENCY REPORT NUMBER

11. SUPPLEMENTARY NOTES The views expressed in this thesis are those of the author and do not reflect the official policy or position of the Department of Defense or the U.S. Government.

12a. DISTRIBUTION/AVAILABILITY STATEMENT
Approved for public release; distribution is unlimited.

12b. DISTRIBUTION CODE

13. ABSTRACT(*maximum 200 words*)

A numerical investigation of unsteady wind tunnel and ground interference effects is carried out in the time domain to study the transonic flutter characteristics of the NLR 7301 section inside a wind tunnel and the thrust generation characteristics of a NACA 0014 airfoil plunging near a ground plane. A parallelized, multi-block, deforming grid, unsteady flow-solver is coupled with a two-degree-of-freedom structural model.

For the transonic flutter problem, two types of porous-wall boundary-conditions are implemented and tested for the boundaries representing the tunnel walls. The type of porous boundary condition is found to influence significantly both steady and unsteady solutions. Results show that the free-flight flutter behavior may differ significantly from the behavior found in a porous wind tunnel because of the strong dependence on the tunnel porosity parameter and the proximity of the walls.

An analysis of the trailing edge boundary condition is performed for the airfoil in ground effect. The computations show that this boundary condition influences the solution only when non-linearities are present in the flow-field, although parameters averaged through a cycle of oscillation are not affected significantly. The same behavior is observed for the influence of the turbulence model on the fully-turbulent, unsteady computations. However, the best agreement with low Reynolds number, experimental data is obtained when the flow is assumed laminar and no turbulence model is applied.

14. SUBJECT TERMS
Transonic Flutter, Wind-Tunnel Interference, Flapping Wings, Airfoil in Ground Effect, Micro-Air Vehicles, Parallel Processing, Multi-Block Grids

15. NUMBER OF PAGES

16. PRICE CODE

17. SECURITY CLASSIFICATION OF REPORT	18. SECURITY CLASSIFICATION OF THIS PAGE	19. SECURITY CLASSIFICATION OF ABSTRACT	20. LIMITATION OF ABSTRACT
Unclassified	Unclassified	Unclassified	UL

NSN 7540-01-280-5500

Standard Form 298 (Rev. 2-89)
Prescribed by ANSI Std. 239-18 298-102

Approved for public release; distribution is unlimited.

MULTI-BLOCK PARALLEL NAVIER-STOKES SIMULATION OF UNSTEADY WIND TUNNEL AND GROUND INTERFERENCE EFFECTS

Breno Moura Castro
B.S., Instituto Tecnológico de Aeronáutica, Brazil, 1985
M.S., Instituto Tecnológico de Aeronáutica, Brazil, 1997

Submitted in partial fullfilment of the
requirements for the degree of

DOCTOR OF PHILOSOPHY IN AERONAUTICAL AND ASTRONAUTICAL ENGINEERING

from the

NAVAL POSTGRADUATE SCHOOL
September 2001

Author: _____
Breno Moura Castro

Approved by: _____
Max F. Platzer
Distinguished Professor of Aeronautics & Astronautics
Dissertation Supervisor and Committee Chair

_____
Garth Hobson
Professor of Aeronautics & Astronautics

_____
Oscar Biblarz
Professor of Aeronautics & Astronautics

_____
Clyde Scandrett
Associate Professor of Mathematics

_____
Daniel Collins
Professor Emeritus of Aeronautics & Astronautics

Approved by: _____
Max F. Platzer, Chair, Department of Aeronautics & Astronautics

Approved by: _____
Carson K. Eoyang, Associate Provost for Academic Affairs

ABSTRACT

A numerical investigation of unsteady wind tunnel and ground interference effects is carried out in the time domain to study the transonic flutter characteristics of the NLR 7301 section inside a wind tunnel and the thrust generation characteristics of a NACA 0014 airfoil plunging near a ground plane. A parallelized, multi-block, deforming grid, unsteady flow-solver is coupled with a two-degree-of-freedom structural model.

For the transonic flutter problem, two types of porous-wall boundary-conditions are implemented and tested for the boundaries representing the tunnel walls. The type of porous boundary condition is found to influence significantly both steady and unsteady solutions. Results show that the free-flight flutter behavior may differ significantly from the behavior found in a porous wind tunnel because of the strong dependence on the tunnel porosity parameter and the proximity of the walls.

An analysis of the trailing edge boundary condition is performed for the airfoil in ground effect. The computations show that this boundary condition influences the solution only when non-linearities are present in the flow-field, although parameters averaged through a cycle of oscillation are not affected significantly. The same behavior is observed for the influence of the turbulence model on the fully-turbulent, unsteady computations. However, the best agreement with low Reynolds number, experimental data is obtained when the flow is assumed laminar and no turbulence model is applied.

TABLE OF CONTENTS

I. INTRODUCTION **1**

A. TRANSONIC FLUTTER STUDIES 1

B. FLAPPING AIRFOIL STUDIES 5

C. COMMON ISSUES 10

D. DISSERTATION OVERVIEW 12

II. THEORETICAL BACKGROUND **15**

A. UNSTEADY AERODYNAMICS 15

1. Governing Equations 15

2. Turbulence Models 18

3. Transition Models 22

4. Numerical Technique 24

B. STRUCTURAL DYNAMICS 32

1. Governing Equations 32

2. Numerical Technique 33

III. BOUNDARY CONDITIONS AND MULTI-BLOCK PROCESSING **35**

A. THREE-BLOCK GRID 35

B. BOUNDARY CONDITIONS 37

1. Wind-Tunnel Problem 38

2. Airfoil in Ground Effect 40

3. Trailing Edge Boundary Condition 40

C. GRID MOTION 52

D. PARALLEL PROCESSING 54

IV. VALIDATION OF THE MODELS 59

A. DEFORMING GRIDS 59

1. Subsonic Flow Test 59

2. Transonic Flow Test 64

B. PRESCRIBED MOTION ANALYSIS 66

1. Single-Airfoil Pitch/Plunge Motion 67

2. Airfoil-in-Ground-Effect and Pure-Plunge Motion 70

V. RESULTS 73

A. FLAPPING AIRFOIL PROPULSION 73

1. Steady-State Computations 75

2. Oscillating Airfoil Computations 79

B. TRANSONIC FLUTTER 90

1. Steady-State Computations 92

2. Flutter Computations 95

VI. CONCLUSIONS AND RECOMMENDATIONS 107

APPENDIX A: DEFORMING GRID EQUATIONS 111

APPENDIX B: GEOMETRIC CONSERVATION LAW 115

APPENDIX C: JACOBIAN MATRICES 119

LIST OF REFERENCES 121

INITIAL DISTRIBUTION LIST 127

LIST OF FIGURES

1.1 Flapping Wing Configurations 9

1.2 Comparison of the Configurations 11

2.1 Paths of Integration for the Osher Scheme 28

2.2 Schematic of the Spring/Mass/Damper System 32

3.1 Schematic of the Three-Block Grid for the Flutter Problem 36

3.2 Schematic of the Three-Block Grid for the Airfoil-in-Ground-Effect Problem . . . 37

3.3 Boundary Conditions for the Flutter Problem 39

3.4 Boundary Conditions for the Airfoil-in-Ground-Effect Problem 41

3.5 Schematic of a C-Grid near the Trailing Edge 41

3.6 Grid around the NACA 0012 Airfoil 43

3.7 Steady-State Solutions for Averaged and Free TE 44

3.8 History of Lift and Drag Coefficients for the Pitch/Plunge Case 45

3.9 Comparison of Pressure Distributions for Averaged and Free TE 47

3.10 Comparison of Pressure Distributions for Averaged and Free TE, NACA 0012, $\hat{\alpha} = 10$ degrees, $M_\infty = 0.3$, $k = 1$, $Re_\infty = 1 \times 10^6$ 48

3.11 Variation of c_D against c_L for the Pitch/Plunge Case 49

3.12 Grid around the NACA 0014 Airfoil 49

3.13 History of Lift and Drag Coefficients for the Pure Plunge Case 50

3.14 Dynamic-Stall Boundary for the NACA 0012 Airfoil 52

3.15 Schematic of the Regions for Grid Motion 54

3.16 Comparison of Surface Pressure Coefficient for Solid Walls 56

3.17 Comparison of History of Angle of Attack for Porous Walls 56

4.1 Close-Up of the Single-Block Grid around the Airfoil 60

4.2 Portion of the Four-Block Grid around the Airfoil 61

4.3 Comparison of Euler Solutions for Single- and Four-Block Grids 62

4.4 Detail of the Four-Block Grid in Its Most Deformed Condition 63

4.5 Steady-State Pressure Distribution for the Four-Block Grid 63

4.6 Three-Block Grid near the NLR 7301 Airfoil 64

4.7 Deviation from the Fixed-Grid Solution 65

4.8 DFT Analysis of the Deviation 66

4.9 Vorticity Contours of Isogai et al. (left) and Present Work (right) 68

4.10 Thrust Coefficient and Propulsive Efficiency for the NACA 0012 Airfoil 69

4.11 Euler Multi-Block Grid near the Airfoil 71

4.12 Comparison of Euler and Potential Flow Solutions for a Biplane Configuration . . 72

5.1 Schematic of the Test Model for the Biplane Configuration 74

5.2 Three-Block Grid near the Airfoil Section 74

5.3 Pressure Coefficient Distributions for B-L and S-A Models 77

5.4 Pressure Coefficient Distributions for Laminar and Turbulent Flows 78

5.5 Entropy Contour Lines for the Laminar Solution 78

5.6 History of Aerodynamic Coefficients for the Laminar Flow Solution 79

5.7 Mach Contour Lines for $M_\infty = 0.3$ and $k = 2.0$ 81

5.8 Supersonic Pocket and Entropy Contours for $M_\infty = 0.3$ and $k = 2.0$ 81

5.9 Mach Contour Lines for $M_\infty = 0.1$ and $k = 2.0$ 82

5.10 Thrust Coefficient for $M_\infty = 0.1$ 83

5.11 Thrust Coefficient for the S-A Turbulence Model 84

5.12 Entropy Contour Lines for Laminar Flow, $M_\infty = 0.1$, and $k = 1.0$ 85

5.13 Entropy Contour Lines for S-A Turb. Model, $M_\infty = 0.1$, and $k = 2.0$ 87

5.14 Entropy Contour Lines for B-L Turb. Model, $M_\infty = 0.1$, and $k = 2.0$ 88

5.15 Propulsive Efficiency for the Biplane Configuration 89

5.16 Comparison between the Biplane and the Single-Airfoil Configurations 89

5.17 C-Type Grid near the NLR 7301 Airfoil 91

5.18 Surface Pressure Distribution for a Porous, Inviscid Boundary Condition at the Tunnel Walls 93

5.19 Surface Pressure Distribution for a Porous, Viscous Boundary Condition at the Tunnel Walls 94

5.20 Angle-of-Attack History for $\sigma = 0.25$, Porous, Inviscid BC, and S-A Turb. Model 96

5.21 Angle-of-Attack History for $\sigma = 0.25$, Porous, Inviscid BC, and B-L Turb. Model 97

5.22 Angle-of-Attack History for $\sigma = 0.25$, Porous, Viscous BC, and S-A Turb. Model 98

5.23 Angle-of-Attack History for $\sigma = 0.25$, Porous, Viscous BC, and B-L Turb. Model 98

5.24 Mach Contour Lines for Porosity $\sigma = 0.25$ and Porous, Inviscid Boundary Condition 100

5.25 Mach Contour Lines for Porosity $\sigma = 0.25$ and Porous, Viscous Boundary Condition 101

5.26 Angle-of-Attack History for $\sigma = 0.50$, Porous, Inviscid BC, and S-A Turb. Model 102

5.27 Variation of LCO Amplitudes with the Porosity Parameter 103

5.28 Variation of LCO Amplitudes with the Solid Blockage 104

5.29 Variation of Angle-of-Attack Amplitudes with Mach Number 105

LIST OF TABLES

5.1 Steady-State Drag Coefficients 76

5.2 Structural Parameters 96

5.3 Flutter Results 99

5.4 LCO Computations 103

LIST OF ABBREVIATIONS, ACRONYMS, AND SYMBOLS

BC = boundary condition

CFD = Computational Fluid Dynamics

LCO = limit-cycle oscillation

LHS = left-hand side

NPS = Naval Postgraduate School

RHS = right-hand side

TE = trailing edge

C_p = pressure coefficient

C_T = thrust coefficient per unit span, $T/(1/2\rho_\infty U_\infty^2 c)$

D_h = plunge-damping coefficient

D_α = pitch-damping coefficient

f = frequency in Hertz

h = plunge displacement (positive downward)

$\hat{h}$ = maximum half amplitude of plunge

I_α = moment of inertia about x_p

k = reduced frequency, $\omega c/U_\infty$

k_α = reduced natural pitching frequency, $\omega_\alpha c/U_\infty$

k_h = reduced natural plunging frequency, $\omega_h c/U_\infty$

K_h = spring constant for plunging

K_α = spring constant for pitching

L = lift

m = mass of the wing

M = pitching moment

$\mathbf{M}_\infty$ = free-stream Mach number

Pr = Prandtl number

Re = Reynolds number

S_α = static moment, $x_\alpha m$

t = time

T = thrust force

U_∞ = free-stream speed

u, w = Cartesian velocity components

x = coordinate along chord

x_p = leading edge to elastic axis distance

x_α = elastic axis to center of mass distance

$\dot{x}|_{wall}$ = velocity component of airfoil surface

$\dot{y}|_{wall}$ = velocity component of airfoil surface

y^+ = dimensionless normal wall distance

α = angle of incidence

$\bar{\alpha}$ = average angle of incidence

$\hat{\alpha}$ = maximum half amplitude of α

α_0 = spring-neutral angle of attack

δ_h = non-dimensional plunge-damping coefficient, $D_h/(2\sqrt{mK_h})$

δ_α = non-dimensional pitch-damping coefficient, $D_\alpha/(2\sqrt{I_\alpha K_\alpha})$

η = propulsive efficiency

ω = circular frequency, $\omega = 2\pi f$

ω_h = undamped natural bending frequency, $\sqrt{K_h/m}$

ω_α = undamped natural torsional frequency, $\sqrt{K_\alpha/I_\alpha}$

Φ = phase angle between pitch and plunge

σ = porosity parameter, Eq. (3.2)

τ = dimensionless time, ta_∞/c

$(\dot{\ })$ = differentiation with respect to t

$(\ )'$ = differentiation with respect to τ

$(\ )_c$ = corrected value

$(\ )_i$ = initial value

$|_{wall}$ = quantity on the surface of the airfoil

$(\ )_\infty$ = free-stream value

ACKNOWLEDGMENT

The author is profoundly grateful to his advisor, Prof. Max Platzer, an outstanding and inspirational teacher whose experience and knowledge were vital for this learning experience. Prof. Platzer labored unflaggingly to improve this dissertation. More than once he sacrificed time that he could have spent with his family to read, to discuss, and to correct the present work.

The author would also like to acknowledge Prof. Kevin D. Jones and Prof. John A. Ekaterinaris as co-advisors of this dissertation. Prof. Jones worked along with Prof. Platzer during the whole course of this effort and Prof. Ekaterinaris was responsible for beginning the development of the multi-block, parallel code. Their guidance was extraordinarily crucial in my accomplishing this work.

The author is also thankful to Dr. Stefan Weber for his brilliant help and advice during the early stages of this work and to Prof. Ismail Tuncer for the discussion about trailing-edge boundary conditions. Thanking Dr. Steven Allmaras for his insightful discussion about the Spalart-Allmaras turbulence model is also essential.

Gratitude is also due to Prof. Brij Agrawal for providing a couple of PC's to the Linux cluster and to Dr. Hong-Jen Chen for outstanding advice and references on writing a Ph.D. dissertation. Special thanks goes to Dr. Christian Taranti for all he did to help this author, especially in setting up the cluster of Linux PC's and to Prof. Ron Russell for editing this dissertation.

The author is immensely thankful to his wife, Mara, for her constant and invaluable support, advice, and love throughout the whole duration of this Ph.D. program.

Finally, this work is dedicated to my parents for their unconditional love and faithful support.

I. INTRODUCTION

The study of unsteady flow problems has become very important in the past few decades. Among many other problems, one can mention thrust and lift generation by means of oscillating wings, flutter, dynamic stall, blade-row interactions in axial compressors, and blade-vortex interactions on helicopter blades as examples of important unsteady aerodynamic problems. The problems of transonic flutter of an airfoil inside a wind tunnel and flapping wing propulsion of opposed-plunging airfoils are the primary interest of this work.

The main purpose of this introductory chapter is to give the reader an overview of the latest achievements related to these two problems and to summarize the contributions of the present work to the numerical computation of unsteady flows past a fluttering airfoil inside a wind tunnel and over a flapping airfoil in ground effect. Consequently, this chapter is divided into specific sections related to these two problems. It also includes a section about some of the details of an unsteady aerodynamics solver common to both problems.

A. TRANSONIC FLUTTER STUDIES

Historically, great efforts have been devoted to experimental and theoretical investigations of the transonic flutter characteristics of airfoils because the transonic dip associated with the flutter speed of typical aircraft wings poses a serious problem for flight safety. Developing theoretical models for unsteady flows has been pursued both analytically and numerically. But because of the strong nonlinear character of the governing equations (Navier-Stokes equations), one still must rely on experiments to understand some flow characteristics or to validate theoretical models. The dramatic advances in computer power in the past few years have made Computational Fluid Dy-

namics (CFD) very popular among engineers and researchers to overcome some of the difficulties of solving the Navier-Stokes equations.

Flutter is a phenomenon generated by the interaction between fluid flow and structure. Therefore, numerical solutions of flutter problems require the use of CFD coupled with Structural Dynamics (SD) solvers. Analytical solutions of the unsteady equations are available only for a few special cases with little practical application. Only very recently, some experimental data was generated with the potential for validating CFD/SD codes, for example the data presented by Schewe et al. [31, 44].

The study of flutter started because of the earlier development of fighter aircraft, especially during World War I. Some designers abandoned the classical biplane configuration, with its interplane bracing, in favor of the mono-plane wing with less torsional rigidity. With the development of faster aircraft, the aeroelastic behavior of the airplane became more important. One of the earliest books published on this subject was written by Bisplinghoff, Ashley, and Halfman [9] in 1955. It was a compilation of the theoretical and experimental tools available at that time for flutter studies. The analytical models were mainly based on the small disturbances concept.

The first significant use of CFD to perform flutter calculations is due to Ballhaus and Goorjian [5] in the late 1970's. They studied the single-degree pitch stability of an NACA 64A006 profile near $M_\infty = 0.88$. The main concern was to predict correctly the motion of the shock with oscillation of the profile, particularly the phase lag with respect to the oscillatory angle-of-attack.

Since then, the use of CFD/SD solvers to analyze flutter problems in the time domain became more and more frequent. For instance, the phenomenon of stall flutter was studied by Ekaterinaris and Platzer [17]. They used a thin-layer Navier-Stokes solver including a transition model with a simplified criterion for the transition onset. The numerical solution with the transition model

showed that the small laminar/transitional separation bubble forming during the pitch-up motion has a decisive effect on the near-wall flow and the development of unsteady loads.

A time-domain analysis of low-speed airfoil flutter was done by Jones and Platzer [25] in 1996. A time-stepping aeroelastic code was used to perform computations for two-airfoil systems. The configurations studied were a two-airfoil tandem and an airfoil in ground effect. Because of the excellent agreement with past results, their code can be applied as a feedback loop to stabilize flutter of a trailing airfoil actively, to investigate wake interference in rotary-wing flowfields, and to simulate flutter in ground effect.

Transonic flutter computations were the subject of several papers published by Beran et al. [6, 10, 36]. The main interest of their investigations was the airfoil flutter boundaries. They used two Euler solvers to calculate the flutter onset for a pitch-and-plunge airfoil at transonic speeds. They applied the Hopf-bifurcation analysis to determine the flutter onset and found that this method is precise and efficient for grids typical of inviscid, transonic airfoil calculations.

Navier-Stokes computations for flutter of an airfoil section were conducted by Weber et al. [54] and Weber et al. [55]. In the former work, a flutter study of turbomachinery blades was conducted by using a full Navier-Stokes code. In the latter, Weber et al. [55] used a thin-layer Navier-Stokes solver to perform Limit Cycle Oscillation (LCO) computations for the NLR 7301 airfoil. Comparisons of this unbounded flow calculation with experimental results obtained by means of a wind tunnel test suggested significant wall interference effects. Castro et al. [11] found that the inclusion of the wind tunnel walls in the modeling of the problem can significantly improve the agreement of numerical and experimental results for steady as well as unsteady computations.

The importance of tunnel interference is well recognized [35], but reliable quantitative estimates are still lacking. For instance, Khalid and Mokry [30] have presented inviscid calculations for tunnel wall interference effects in steady flow over a NACA 0012 airfoil in 2-D transonic flow. How-

ever, no Navier-Stokes studies seem to have been done to analyze unsteady transonic interference effects.

This dissertation is a continuation of the work presented in [11] in which it was found that both the porosity and the way of applying the corresponding boundary condition influenced the results of both steady and unsteady computations for the NLR 7301 airfoil inside a wind tunnel at transonic speeds. In that work, modeling the porosity of the tunnel wall required a very careful construction of the grid in which the cells were approximately equally spaced at the wall regions. This was necessary because some grid cells were treated as solid walls while others were treated as holes in order to achieve the desired porosity. For example, a 50% porosity was modeled by treating four consecutive grid cells as holes, the next four as solid walls, and so on. The drawback of this approach was that a very limited number of possible values of porosity could be simulated due to the finite number of grid cells at the wind tunnel walls. In fact, only porosity values of 25%, 50%, and 75% were feasible. Furthermore, the plenum chamber pressure was not included in the model.

Comparisons with experimental results obtained in the DLR-Göttingen wind tunnel [31, 44] have demonstrated that inclusion of wind-tunnel effects is the key to obtaining better agreement of both the steady-state pressure distribution and the flutter characteristics with the experiment.

A primary goal of the present investigation was to improve the porous wind-tunnel wall model used in the previous study, specifically, providing solution uniqueness and including the plenum pressure. As earlier mentioned, the previous model provided a number of ways to achieve the same porosity, each resulting in a different solution. Furthermore, it was desirable to eliminate the requirement for equally spaced gridding along the tunnel walls. In the present work, the approach presented by Mokry et al. [35] is used. The normal velocity at the porous wall is set proportional to the pressure difference between the plenum chamber and the test section wall. This

model allows a much more continuous variation of flow parameters and does not require an equally spaced grid along the walls.

In this dissertation, the effect of tunnel wall interference on transonic flutter/limit-cycle prediction is investigated in further detail. To this end, parametric studies of porosity, tunnel height, and Mach number are conducted. Numerical solutions are obtained for an airfoil free to oscillate in two-degrees-of-freedom in transonic flow and the results are compared with the measurements of Knipfer et al. [31].

The problem of transonic flutter of an airfoil inside a wind tunnel is solved because there is neither an analytical nor an experimental method of eliminating measurement interference caused by wind tunnel walls in the transonic regime.

B. FLAPPING AIRFOIL STUDIES

Flapping wing propulsion has been used by birds and insects for many millennia but barely by mankind. Although the concept of obtaining thrust by means of a plunging airfoil was explained by Knoller [32] in 1909 and by Betz [7] in 1912, very few efforts have been made to explore or to study this alternative to the more conventional use of propellers.

The first experimental demonstration of the feasibility of flapping wing propulsion was performed by Katzmayr [29] in 1922. The first solution for incompressible flow past flapping airfoils was presented by Birnbaum [8] in 1924. Then, in 1936, Garrick [19] solved the problem of a sinusoidally plunging airfoil, using Theodorsen's theory [48], for the whole range of reduced frequencies. This solution was based on the linear theory and does not hold for detached flows typical of high reduced frequencies.

One of the earliest numerical models for a 3-D flapping wing was developed by Lan [33] in 1979. He used an unsteady quasi-vortex-lattice to calculate the propulsive efficiency and thrust for some swept and rectangular planforms by varying the phase angles between the pitching and plunging motions. It was shown that aerodynamically interacting tandem wings, as used by the dragonfly, can produce high thrust with high efficiency when the pitching is in advance of the flapping and the hind wing leads the fore wing with some optimum phase angle. Linear theory was also used in this case, therefore, detached flows are not captured by this model.

With the advent of CFD, the problem with detached flows could be overcome. It became possible to study important unsteady phenomena, such as the dynamic stall. Among the recent investigations done on this subject, the work of Platzer et al. [42, 43, 53] deserves special attention. They applied a thin-layer Navier-Stokes solver improved with a transition model based on Gostelow et al. [20] and determined the dynamic stall boundaries for the NACA 0012 airfoil. Furthermore, they investigated the need of including a transition model into the CFD solver and also the characteristics of dynamic stall and flapping airfoil propulsion. On the prediction of dynamic stall, Jones and Platzer [26] showed that the delay in the dynamic stall onset is related to the dynamic pressure lag.

Platzer et al. [23, 28, 22, 51, 52] also studied the problem of flapping wing propulsion in close detail. Numerically, they used both an unsteady panel code method (UPOT) coupled with a boundary-layer solver and a thin-layer Navier-Stokes solver for their computations. Experimentally, a low-speed wind tunnel and also a water tunnel were used. Among other conclusions, they showed that some configurations of two airfoils can produce better propulsive efficiency than a single flapping wing. As an example of such configurations, the flapping/stationary airfoil combination in tandem provided a 40% augmentation in propulsive efficiency.

The work performed by Isogai et al. [21] is also worth mentioning. They studied the effects of dynamic stall on propulsive efficiency and thrust of a flapping NACA 0012. It was determined that a phase angle between the pitch and plunge motions of 90 degrees would yield optimum values of propulsive efficiency and thrust. A similar result was obtained experimentally by Anderson [3] and Anderson et al. [2]. Using a model for the NACA 0012 immersed in a water tunnel, it was found that the highest propulsive efficiencies were obtained for a phase angle of approximately 75 degrees between pitch and plunge and motions with high effective angles of attack. This indicates that the presence of the dynamic stall vortices might not always be detrimental to thrust generation.

More recently, Dickinson et al. [14] experimentally studied the characteristics of flight of an insect wing. It was found that the most important mechanisms in insect flight are what they called "rotational circulation" and "wake capture." In the latter mechanism, the wing benefits from the shed vorticity of the previous stroke. They effectively demonstrated that the wing can produce positive lift by interacting with its own wake.

Ramamurti and Sandberg [40] also studied the problem of an oscillating NACA 0012. With a finite element incompressible flow solver, they investigated the effects of varying the phase angle between pitch and plunge motions. Their results show good agreement with the experiments of Anderson [3] for the thrust coefficient, and it was found that phase angles between pitch and plunge around 90 degrees deliver the best propulsive efficiency.

Some of the flapping wing configurations investigated in recent years are presented in Fig. 1.1. The single airfoil (a) has been the subject of many studies. The opposed-plunge (c) combination was investigated both numerically and experimentally by Jones and Platzer [28] and Lund et al. [34]. The numerical investigation was done using an unsteady potential flow code modified to compute incompressible flow over two airfoils oscillating in plunge with a phase angle of 180 degrees. This code, called USPOT, was originally developed by Pang [37] in 1988. It is im-

portant to recall that the flow solution for two airfoils arranged in a biplane fashion, oscillating in plunge with a phase angle of 180 degrees, is equivalent to the flow over a single airfoil oscillating near a ground plane. This remains true even for viscous flow solutions as long as an inviscid flow tangency condition is enforced along the ground plane. In their experimental investigation, Jones and Platzer [28] built and tested a biplane configuration. Therefore, the single airfoil in ground effect solution developed in this dissertation can be compared with their experimental results. The experimental part was conducted in the Naval Postgraduate School low-speed wind tunnel.

Apparently, the only Navier-Stokes computations for the opposed-plunge, or biplane, configuration have been done by Tuncer and Kaya [50]. Their approach consists of applying C-grids for each airfoil and over-setting them with a Cartesian grid in a "Chimera" fashion. It appears that no computations were done for such a configuration using a deforming grid approach. Therefore, one of the purposes of this dissertation is to analyze this problem using the same thin-layer Navier-Stokes solver used for investigating the transonic flutter of an airfoil with wind tunnel wall interference.

The problem of an airfoil oscillating in ground effect is investigated in this dissertation because the micro-air vehicle developed at the Naval Postgraduate School uses a biplane wing configuration for thrust generation. This configuration is known to produce more thrust per wing than the single wing configuration and allows a much better mechanical balance.

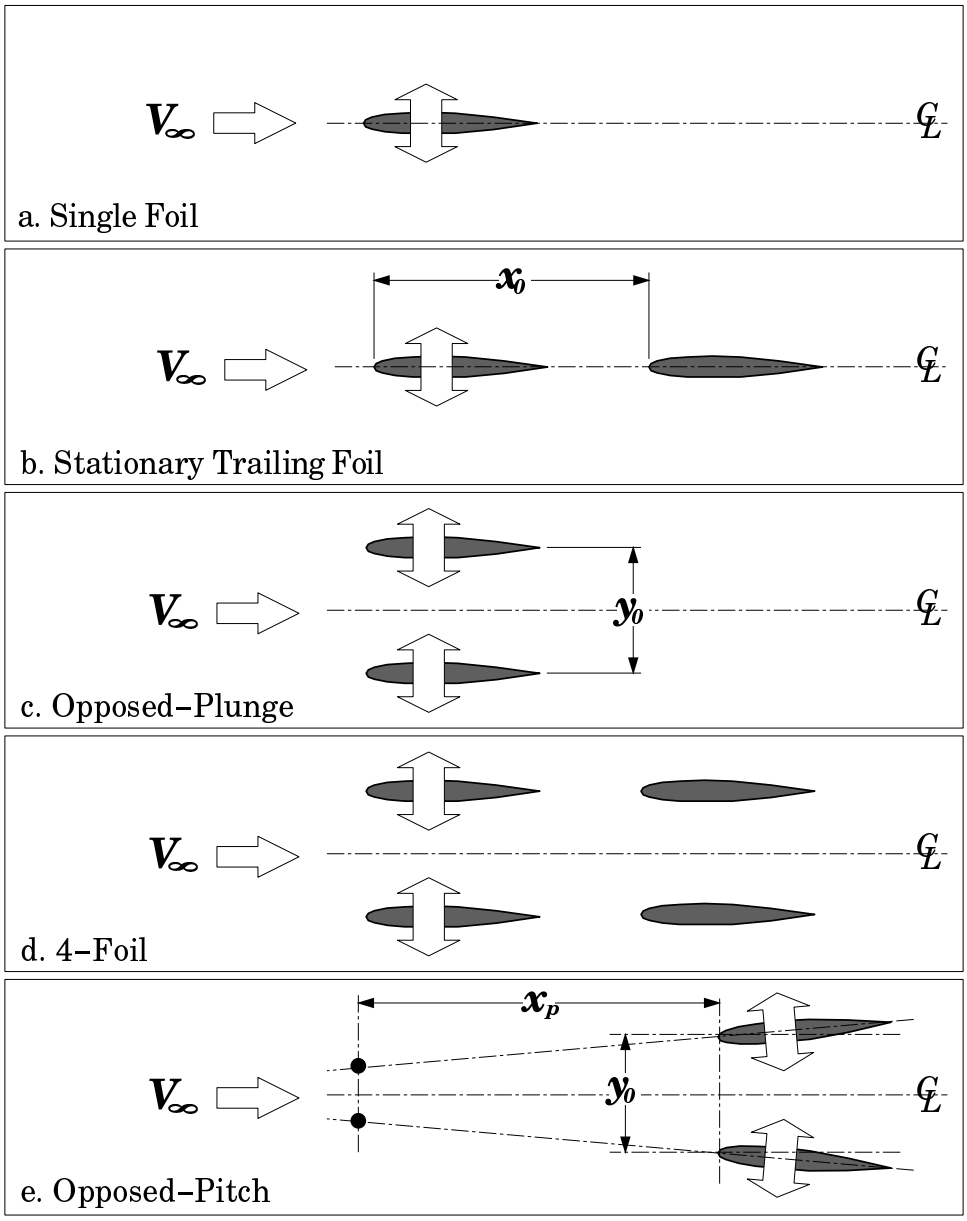

Figure 1.1. Flapping Wing Configurations

C. COMMON ISSUES

The flow solver and the aeroelastic models used in the present investigation have been tested and validated extensively in previous studies for a variety of flow conditions. For example, the flow solver and the turbulence models have been tested for subsonic flow [43, 16, 18] and for transonic flow [15]. The aeroelastic model has been implemented and tested in [27] for inviscid flow calculations and in [55] for viscous, transonic flow.

The transition modeling capability of the code was demonstrated in [55, 43]. Nevertheless, because previous results of [55] showed that transition only slightly improved the numerical results, transition modeling was not used in the present investigation, assuming fully turbulent flow.

The influence of the different turbulence models available for the present code in the numerical predictions of transonic flutter was also studied by Weber et al. [55]. It is known that turbulence models are calibrated only for steady-state flows. Nevertheless, it is common practice to apply them for unsteady flows without any further modification. It was found during this work that, for one-equation turbulence models applied to moving grid problems, some modifications in their implementation is necessary. Specifically, the time metrics should be included in the computation of the contravariant velocity used in the convective terms, and a time-accurate integration of the transport equation should be performed. This modification was discussed with Dr. Steven Allmaras [1] and represents one of the contributions of the present investigation.

The ability of the multi-block version of the flow solver to predict accurately the flow over a stationary airfoil in a wind tunnel by including porous wall effects was demonstrated in the previous work [11].

The problems of flutter of an airfoil inside a wind tunnel and of an oscillating airfoil near a wall can be numerically solved in a very similar manner. For the former, two wall boundary conditions should be applied both above and below the airfoil. For the latter, only one wall boundary

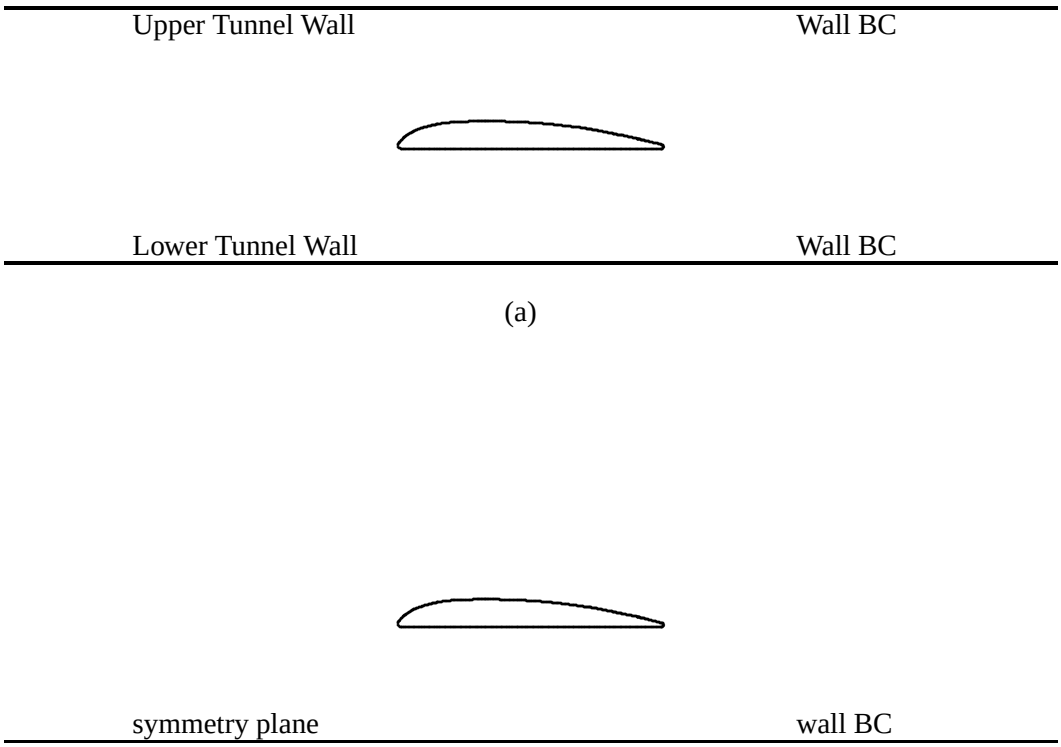

Figure 1.2. Comparison of the Configurations

condition is necessary below the airfoil. For the upper boundary, free-stream boundary conditions are applied. Therefore, the same solver, only with minor changes owing to specific characteristics of each configuration, can be used for numerical computations of both problems.

Time-accurate unsteady computations require large computing times until a reasonable number of cycles is reached. Computational efficiency can be improved by taking advantage of parallel architectures. The computational domain is divided into three blocks to enable discretization of the full geometry, for both problems under investigation. This makes the approach suitable for parallel computation. Therefore, a newly developed parallel version of the code uses three Pentium II 400 MHz PC's to carry out the computations, assigning one block to each processor. The boundary conditions are transferred from one machine to another via a specific library called

Message Passing Interface (MPI). The cluster of Linux PC's is effective in performing the parallel computations and is also effective in reducing the wall-clock time.

D. DISSERTATION OVERVIEW

The theoretical background for the computational codes used in this work is presented in Chapter II. The thin-layer Navier-Stokes equations in conservative, unsteady, generalized coordinate, and nondimensional form are discussed along with some important issues, such as the numerical scheme, turbulence models, deforming grids, and transition models. The necessary adjustments for working with moving and changing grids are pointed out. A brief explanation of the two-degree-of-freedom structural dynamics model is also given in Chapter II.

Some more specific topics concerning the present work are presented in Chapter III. It contains an explanation of why a three-block grid configuration is used and how a parallelized version of the program is implemented. The treatment of boundary conditions, one of the most important issues concerning unsteady aerodynamics, is also discussed in Chapter III. Specific boundary conditions for both the transonic flutter in the wind tunnel and the airfoil in ground effect configuration are explained in more detail. Furthermore, a combined pitch/plunge motion is imposed to a NACA 0012 airfoil in order to evaluate the performance of two different boundary conditions at the trailing edge.

The validations of the computational code used in this work are presented in Chapter IV, specifically with respect to the moving or deforming grid capability of the solver. A transonic steady-state computation is performed to show that the program does not generate large deviations from the solution when moving grid points are crossing shock waves. A subsonic numerical test is conducted to show that a multi-grid discretization yields a similar solution as a single-grid approach.

At the end of this chapter, a comparison with a potential flow solver solution is done for a biplane, opposed-plunge configuration. The purpose of this chapter is to show that the theory presented in Chapters II and III is adequate for treating deforming grid problems.

The results obtained for the two problems under investigation are presented in Chapter V. In the first section of this chapter, the details about the results for the flapping airfoil in ground effect configuration are discussed. A NACA 0014 airfoil is allowed to oscillate in the pure plunge mode near a wall. The influence of some parameters, such as the Reynolds and Mach numbers is investigated. Fully turbulent computations are done for the Spalart-Allmaras and Baldwin-Lomax turbulence models. A fully laminar simulation is performed for a Reynolds equal to 10,000 as well. The second part of this chapter is dedicated to the transonic flutter with tunnel wall interference of the NLR 7301 airfoil. The influence of the porous wall boundary condition is studied in close detail. The porosity parameter is found to change the steady-state solutions significantly. Therefore, porosity parameter's influence on the limit cycle oscillations is also evaluated. Because the Mach number is close to the transonic dip, this parameter is varied in order to evaluate the changes in the flutter characteristics of the NLR 7301 section. The height of the wind tunnel test section is increased to assess correlations of wind tunnel tests with unbounded flow situations.

Finally, the conclusions of the present work for the two problems under investigation and the recommendations for future studies are discussed in Chapter VI.

THIS PAGE INTENTIONALLY LEFT BLANK

II. THEORETICAL BACKGROUND

A. UNSTEADY AERODYNAMICS

1. Governing Equations

The solution for the problem of an unsteady, compressible, and viscous flow of a Newtonian fluid is obtained by solving the Navier-Stokes (N-S) equations. They are presented in matrix, non-dimensional, and Cartesian coordinate form in Eq. (2.1):

$$\frac{\partial Q}{\partial t} + \frac{\partial F}{\partial x} + \frac{\partial G}{\partial z} = Re^{-1}\left(\frac{\partial R}{\partial x} + \frac{\partial S}{\partial z}\right) \tag{2.1}$$

where $Q = (\rho, \rho u, \rho w, e)^T$ is the dependent variable and represents a vector which components are the flow state variables.

The reference values for non-dimensionalization are the chord length $\tilde{c}$, the free stream density $\tilde{\rho}_\infty$, the free stream speed-of-sound $\tilde{a}_\infty$, the time $\tilde{c}/\tilde{a}_\infty$, and the specific energy $\tilde{\rho}_\infty \tilde{a}_\infty^2$.

The fluxes F, G, R, and S are given by:

$$F = \begin{Bmatrix} \rho u \\ \rho u^2 + p \\ \rho u w \\ (e+p)u \end{Bmatrix}, \qquad G = \begin{Bmatrix} \rho w \\ \rho u w \\ \rho w^2 + p \\ (e+p)w \end{Bmatrix},$$

$$R = \begin{Bmatrix} 0 \\ \tau_{xx} \\ \tau_{xz} \\ \tau_{xx}u + \tau_{zx}w - q_x \end{Bmatrix}, \quad S = \begin{Bmatrix} 0 \\ \tau_{zx} \\ \tau_{zz} \\ \tau_{xz}u + \tau_{zz}w - q_z \end{Bmatrix}; \tag{2.2}$$

where:

$$\tau_{xx} = \lambda\left(\frac{\partial u}{\partial x} + \frac{\partial w}{\partial z}\right) + 2\mu\frac{\partial u}{\partial x}, \quad \tau_{xz} = \mu\left(\frac{\partial u}{\partial z} + \frac{\partial w}{\partial x}\right), \quad \tau_{zz} = \lambda\left(\frac{\partial u}{\partial x} + \frac{\partial w}{\partial z}\right) + 2\mu\frac{\partial w}{\partial z},$$

$$q_x = -k\frac{\partial T}{\partial x}, \qquad q_z = -k\frac{\partial T}{\partial z}, \qquad \lambda = -2\mu/3\,. \tag{2.3}$$

Pressure is related to the other variables through the equation of state for an ideal gas

$$p = \rho R T\,. \tag{2.4}$$

The N-S equations have analytical solutions only for a few simple problems. Usually, their solution involves a numerical procedure using a digital computer. This technique is called Computational Fluid Dynamics (CFD) and can be performed either with the Finite-volume method or the Finite-difference method. Both methods require the generation of a computational grid to discretize the flow-field. The grid can be adaptive to the boundaries of the domain where the N-S equations are being solved. Such a situation demands the N-S equations to be written in generalized coordinates (τ, ξ, and ζ):

$$\hat{Q}_\tau + \hat{F}_\xi + \hat{G}_\zeta = Re^{-1}(\hat{R}_\xi + \hat{S}_\zeta) \ , \tag{2.5}$$

where:

$$\begin{aligned} \hat{Q} &= J^{-1}Q & J &= (x_\xi z_\zeta - x_\zeta z_\xi)^{-1} \\ \hat{F} &= \hat{\xi}_t Q + \hat{\xi}_x F + \hat{\xi}_z G & \hat{R} &= \hat{\xi}_x R + \hat{\xi}_z S \\ \hat{G} &= \hat{\zeta}_t Q + \hat{\zeta}_x F + \hat{\zeta}_z G & \hat{S} &= \hat{\zeta}_x R + \hat{\zeta}_z S \end{aligned} \ , \tag{2.6}$$

and

$$\begin{aligned} \hat{\xi}_t &= J^{-1}\xi_t = x_\zeta z_\tau - x_\tau z_\zeta & \hat{\zeta}_t &= J^{-1}\zeta_t = x_\tau z_\xi - x_\xi z_\tau \\ \hat{\xi}_x &= J^{-1}\xi_x = z_\zeta & \hat{\zeta}_x &= J^{-1}\zeta_x = -z_\xi \\ \hat{\xi}_z &= J^{-1}\xi_z = -x_\zeta & \hat{\zeta}_z &= J^{-1}\zeta_z = x_\xi \end{aligned} \ . \tag{2.7}$$

Equation (2.5) represents the Navier-Stokes equations in conservative, non-dimensional form and is written in terms of the computational domain variables. They are also valid for moving or deforming grids because the Jacobian, J, is considered to be a function of time (see Appendix A for details).

A common simplification to the Navier-Stokes equations is the thin-layer approximation where the term $\hat{R}_\xi$ on the RHS of Eq. (2.5) is neglected in comparison with $\hat{S}_\zeta$:

$$\partial_\tau \hat{Q} + \partial_\xi \hat{F} + \partial_\zeta \hat{G} = Re^{-1}\partial_\zeta \hat{S} \ . \tag{2.8}$$

Substituting Eq. (2.2) into Eq. (2.6):

$$\hat{Q} = J^{-1}\begin{Bmatrix} \rho \\ \rho u \\ \rho w \\ e \end{Bmatrix} \qquad \hat{F} = J^{-1}\begin{Bmatrix} \rho U \\ \rho u U + \xi_x p \\ \rho w U + \xi_z p \\ (e+p)U - \xi_t p \end{Bmatrix}$$

$$\hat{G} = J^{-1}\begin{Bmatrix} \rho W \\ \rho u W + \zeta_x p \\ \rho w W + \zeta_z p \\ (e+p)W - \zeta_t p \end{Bmatrix} \qquad \hat{S} = J^{-1}\begin{Bmatrix} 0 \\ \mu m_1 u_\zeta + (\mu/3) m_2 \zeta_x \\ \mu m_1 w_\zeta + (\mu/3) m_2 \zeta_z \\ \mu m_1 m_3 + (\mu/3) m_2 m_4 \end{Bmatrix} \quad , \tag{2.9}$$

where:

$$\begin{aligned} m_1 &= \zeta_x^2 + \zeta_z^2 \\ m_2 &= \zeta_x u_\zeta + \zeta_z w_\zeta \\ m_3 &= \partial_\zeta (u^2 + w^2)/2 + [(\gamma - 1)Pr]^{-1} \partial_\zeta (a^2) \\ m_4 &= \zeta_x u + \zeta_z w \end{aligned} \quad . \tag{2.10}$$

The terms U and W are the contravariant velocity components given by:

$$\begin{aligned} U &= \xi_t + \xi_x u + \xi_z w \\ W &= \zeta_t + \zeta_x u + \zeta_z w \end{aligned} \quad . \tag{2.11}$$

Pressure is related to the other variables through the equation of state for an ideal gas:

$$p = (\gamma - 1)\left[e - \rho(u^2 + w^2)/2\right] \ . \tag{2.12}$$

2. Turbulence Models

Turbulence models are introduced to solve the closure problem generated by time averaging the N-S equations. They are divided into categories, such as Algebraic, One-Equation, and Two-

Equation models. The method used in this work is implemented with one Algebraic turbulence model called Baldwin-Lomax (B-L) and one One-Equation model called Spalart-Allmaras (S-A).

The effects of turbulence are translated in terms of an eddy viscosity coefficient (μ_t) and new heat flux terms. The fluid viscosity μ is replaced by $\mu_l + \mu_t$, where μ_l represents the laminar viscosity, and $k/c_p = \mu/Pr$ by $k/c_p = \mu_l/Pr + \mu_t/Pr_t$.

a. Baldwin-Lomax Turbulence Model

The Baldwin-Lomax turbulence model, presented in [4], represents a two-layer algebraic eddy viscosity model in which the term μ_t is described by:

$$\mu_t = \begin{cases} (\mu_t)_{inner}, & y \leq y_{crossover} \\ (\mu_t)_{outer}, & y > y_{crossover} \end{cases} \tag{2.13}$$

where y is the normal distance from the wall and $y_{crossover}$ is the smallest value of y at which values from the inner and outer equations are equal.

The equations for the inner sub-layer are based on a Prandtl-Van Driest formulation:

$$(\mu_t)_{inner} = \rho \ell^2 |\omega| \tag{2.14}$$

where:

$$\begin{aligned} \ell &= \kappa y[1 - e^{-y^+/A^+}] \\ |\omega| &= \sqrt{\left(\frac{\partial w}{\partial x} - \frac{\partial u}{\partial z}\right)^2} \\ y^+ &= \frac{\rho_w u_\tau y}{\mu_w} = \frac{\sqrt{\rho_w \tau_w} y}{\mu_w} \end{aligned} \tag{2.15}$$

The following equations are used for the outer region:

$$(\mu_t)_{outer} = K C_{cp} \rho F_{wake} F_{kleb}(y) \tag{2.16}$$

where K is the Clauser constant, C_{cp} is an additional constant, and

$$
\begin{aligned}
F_{wake} &= min(y_{max}F_{max}, C_{wk}y_{max}U_{dif}^2/F_{max}) \\
F(y) &= y|\omega|[1-e^{-y^+/A^+}] \\
F_{kleb}(y) &= \left[1+5.5\left(\frac{C_{kleb}y}{y_{max}}\right)^6\right]^{-1} \\
U_{dif} &= (\sqrt{u^2+w^2})_{max} - (\sqrt{u^2+w^2})_{min}
\end{aligned}
\tag{2.17}
$$

The variables y_{max} and F_{max} are determined from the function $F(y)$. In wakes, the exponential term of this function is set equal to zero. The function $F_{kleb}(y)$ is the Klebanoff intermittency factor. U_{dif} is the difference between maximum and minimum total velocities in the profile for a fixed x station. The second (min) term in the equation for U_{dif} is taken as zero for wakes. These equations avoid the necessity of finding the outer edge of the boundary layer.

The constants in the equations for the B-L model are given below:

$$
\begin{aligned}
A^+ &= 26 & \kappa &= 0.4 \\
C_{cp} &= 1.6 & K &= 0.0168 \\
C_{kleb} &= 0.3 & Pr &= 0.72 \\
C_{wk} &= 0.25 & Pr_t &= 0.9
\end{aligned}
\tag{2.18}
$$

b. Spalart-Allmaras Turbulence Model

The S-A turbulence model is suggested in [45]. Reynolds-averaged Navier-Stokes equations and a transport equation are solved for this turbulence model. The formulation for the eddy viscosity ν_t is given by:

$$
\begin{aligned}
&-\overline{u_iu_j} = 2\nu_t S_{ij} \quad S_{ij} \equiv \left(\frac{\partial U_i}{\partial x_j} + \frac{\partial U_j}{\partial x_i}\right) \\
&\nu_t = \tilde{\nu} f_{v1} \qquad f_{v1} = \frac{\chi^3}{\chi^3 + c_{v1}^3} \qquad \chi \equiv \frac{\tilde{\nu}}{\nu}
\end{aligned}
\tag{2.19}
$$

where ν is the molecular viscosity, $\tilde{\nu}$ is the working variable and obeys the transport equation for this model:

$$\begin{aligned} \frac{D\tilde{\nu}}{Dt} &= c_{b1}[1-f_{t2}]\tilde{S}\tilde{\nu} + \frac{1}{\sigma}\left[\nabla\cdot((\nu+\tilde{\nu})\nabla\tilde{\nu}) + c_{b2}(\nabla\tilde{\nu})^2\right] \\ &\quad - \left[c_{w1}f_w - \frac{c_{b1}}{\kappa^2}f_{t2}\right]\left[\frac{\tilde{\nu}}{d}\right]^2 + f_{t1}\Delta U^2 \end{aligned} \tag{2.20}$$

and

$$\begin{aligned} &\tilde{S} \equiv S + \frac{\tilde{\nu}}{\kappa^2 d^2} f_{v2} \qquad f_{v2} = 1 - \frac{\chi}{1+\chi f_{v1}} \\ &f_w = g\left[\frac{1+c_{w3}^6}{g^6+c_{w3}^6}\right]^{1/6} \quad g = r + c_{w2}(r^6 - r) \qquad r \equiv \frac{\tilde{\nu}}{\tilde{S}\kappa^2 d^2} \end{aligned} \tag{2.21}$$

S represents the magnitude of the vorticity and d is the distance to the closest wall. The boundary condition for the wall is obtained by setting $\tilde{\nu} = 0$. The functions f_{t2} and f_{t1} are expressed by:

$$\begin{aligned} f_{t2} &= c_{t3}\, exp(-c_{t4}\chi^2) \\ f_{t1} &= c_{t1}\, g_t\, exp\left(-c_{t2}\frac{\omega_t^2}{\Delta U^2}[d^2 + g_t^2 d_t^2]\right) \\ g_t &\equiv min(0.1, \Delta U/\omega_t \Delta x) \end{aligned} \tag{2.22}$$

where d_t is the distance from the field point to the trip, which is on the wall, ω_t is the wall vorticity at the trip, ΔU is the difference between the velocity at the field point and the velocity at the trip, and Δx is the grid spacing along the wall at the trip.

The constants used for this model are

$$\begin{array}{ccc} c_{b1} = 0.1355 & c_{w1} = c_{b1}/\kappa^2 + (1+c_{b2})/\sigma & c_{t1} = 1.0 \\ c_{b2} = 0.622 & c_{w2} = 0.3 & c_{t2} = 2.0 \\ \sigma = 2/3 & c_{w3} = 2.0 & c_{t3} = 1.1 \\ \kappa = 0.41 & c_{v1} = 7.1 & c_{t4} = 2.0 \end{array} \tag{2.23}$$

The constants used in this turbulence model are calibrated for steady flows. In this work, the constants are assumed to be good for unsteady flows as well. This is a necessary assumption because there are no calibrations for unsteady flows so far. More importantly, the coding of this turbulence model assumes that the grid is not changing, i.e., the grid is not a function of time.

In other words, this turbulence model, as it is usually coded, is calibrated for steady flows and is not changing-grid compatible. The latter is because the contravariant velocities are coded, in the turbulence model subroutine, simply as:

$$U = \xi_x u + \xi_z w \quad \text{and} \quad W = \zeta_x u + \zeta_z w \tag{2.24}$$

For the turbulence model to be moving- or deforming-grid compatible, it must use the following equation for the contravariant velocities:

$$U = \xi_t + \xi_x u + \xi_z w \quad \text{and} \quad W = \zeta_t + \zeta_x u + \zeta_z w \tag{2.25}$$

The terms ξ_t and ζ_t represent changes in the grid-conforming coordinates with time and are not related to the fact that the flow is unsteady. There might be a situation in which the flow is steady and the grid is changing, such as in an adaptive grid solution, and those time metrics should be included in the equations of the turbulence models.

In a personal communication with Dr. Steven Allmaras [1], he confirmed that the changes made to the conservation equations (mass, momentum, energy), to incorporate unsteady and moving grids, should be duplicated for the S-A model. Another issue mentioned by Dr. Allmaras was the time integration. Most turbulent codes, as well as the present one, use a decoupled relaxation (or time integration) between the conservation equations and the turbulence model. This decoupled time integration introduces a first-order error (O(Δt)) into the results. This error can become significant for high frequencies. A solution for this problem would be implementing a subiteration process at each time step.

3. Transition Models

The transition from laminar to turbulent flow is a highly important issue on flow calculations because it has a strong influence on the predictions of losses, separation, and stall. Transition also

has a significant effect on the computed values of wall shear stresses and surface heat transfer. Transition criteria used today in CFD codes are based mainly on the work of Gostelow et al. [20].

Transition models start with the prediction of the transition onset location and, then, move on to the evaluation of the transition length. In this work, transition onset location is predicted using Michel's Criterion [12] and the transition length is evaluated based on the model proposed by Gostelow et al. [20].

a. Michel's Criterion

This criterion assumes that transition is initiated when the Reynolds number based on the momentum thickness, Re_θ, and the Reynolds number based on x, Re_x, satisfy the equation:

$$Re_\theta = 1.174\left(1+\frac{22,400}{Re_{x_{tr}}}\right)Re_{x_{tr}}^{0.46} \quad \text{where} \quad Re_\theta = U_e\theta/\nu_\infty \ . \tag{2.26}$$

Equation (2.26) is solved for x_{tr} and this value is used as x_t in the Gostelow et al. [20] model.

b. Gostelow et al.

The idea behind this model is that the turbulent viscosity should be weighted by an intermittency function to provide a smooth transition from laminar to turbulent flow. This is done according to Eq. (2.27):

$$\mu_{trans} = \gamma(x)\,\mu_{turb} \ . \tag{2.27}$$

The intermittency function in the transitional region is given by

$$\gamma(x) = 1 - \exp\left[-n\int_{x_t}^{x}\frac{\sigma}{\tan\varepsilon}\left(\frac{dx}{U}\right)\int_{x_t}^{x}\tan\varepsilon\,dx\right] \tag{2.28}$$

where σ is the spot propagation parameter, ε is the spot spreading half angle, and λ_θ is the pressure

gradient parameter and they are described by:

$$\varepsilon = 4 + \frac{22.14}{0.79 + 2.72\exp(47.63\lambda_\theta)}\,, \tag{2.29}$$

$$\sigma = 0.03 + \frac{0.37}{0.48 + 3.0\exp(52.9\lambda_\theta)}\,, \tag{2.30}$$

and

$$\lambda_\theta = \frac{\theta^2/\nu}{dU/dx} \tag{2.31}$$

where θ is the boundary-layer momentum thickness and U is the outer-edge velocity. The spot generation rate, n, is inferred from the dimensionless breakdown-rate parameter, N, where:

$$n = \frac{\nu N}{\sigma \lambda_{\theta_t}^3}\,, \tag{2.32}$$

$$N = \begin{cases} 0.86 \times 10^{-3}\exp(2.134\lambda_{\theta_t}\ln(q_t) - 59.23\lambda_{\theta_t} - 0.564\ln(q_t)), & \text{for } \lambda_{\theta_t} \leq 0 \\ N(\lambda_\theta = 0) \times \exp(-10\sqrt{\lambda_{\theta_t}}), & \text{for } \lambda_{\theta_t} > 0 \end{cases}\,, \tag{2.33}$$

and where q_t denotes the free-stream turbulence.

The spot-propagation-rate and the spot spreading half-angle asymptotically approach a maximum value for high negative values of λ_θ, but n is allowed to increase to infinity for high negative values of λ_{θ_t}, where λ_{θ_t} is the pressure gradient at the transition onset location, x_t.

The value of the intermittency parameter, $\gamma(x)$, is zero for $x \leq x_t$, and increases downstream from the transition point, asymptotically to a maximum value of unity, which corresponds to fully-turbulent flow. The value of x_t is usually given by Michel's criterion.

4. Numerical Technique

The Thin-Layer Navier-Stokes (TLNS) equations are discretized using an alternate direction implicit (ADI), third-order accurate in space, second-order accurate in time, finite-volume scheme, which can be represented by:

$$
\begin{aligned}
\left[I + h_\xi(\nabla_\xi \hat{A}^+_{i,k} + \Delta_\xi \hat{A}^-_{i,k})^p\right] \Delta\hat{Q}^*_{i,k} &= -\hat{r}^p_{i,k} \\
\left[I + h_\zeta(\nabla_\zeta \hat{B}^+_{i,k} + \Delta_\zeta \hat{B}^-_{i,k} - Re^{-1}\delta_\zeta \hat{M}_{i,k})^p\right] (\hat{Q}^{p+1}_{i,k} - \hat{Q}^p_{i,k}) &= \Delta\hat{Q}^*_{i,k}
\end{aligned}
\tag{2.34}
$$

where:

$$
\begin{aligned}
\hat{r}^p_{i,k} = \quad & (\hat{Q}^p_{i,k} - \hat{Q}^n_{i,k}) + h_\xi(\hat{F}_{i+1/2,k} - \hat{F}_{i-1/2,k})^p \\
& + h_\zeta(\hat{G}_{i,k+1/2} - \hat{G}_{i,k-1/2})^p - Re^{-1} h_\zeta(\hat{S}_{i,k+1/2} - \hat{S}_{i,k-1/2})^p
\end{aligned}
\tag{2.35}
$$

The variables $\hat{A}$, $\hat{B}$, and $\hat{M}$ are the flux Jacobian matrices and are defined as $\hat{A} = \partial\hat{F}/\partial\hat{Q}$, $\hat{B} = \partial\hat{G}/\partial\hat{Q}$, and $\hat{M} = \partial\hat{S}/\partial\hat{Q}$, respectively. A flux splitting, according to Steger and Warming [46], is applied to matrices $\hat{A}$ and $\hat{B}$, where $\hat{A} = \hat{A}^+ + \hat{A}^-$ and $\hat{B} = \hat{B}^+ + \hat{B}^-$.

The h quantities are defined as $h_\xi = \Delta\tau/\Delta\xi$ and $h_\zeta = \Delta\tau/\Delta\zeta$. ∇, Δ, and δ are the forward, backward, and central difference operators, respectively.

The variables $\hat{F}_{i+1/2,k}$, $\hat{G}_{i,k+1/2}$, and $\hat{S}_{i,k+1/2}$ are numerical fluxes. The superscript $(.)^n$ denotes the physical time step and the superscript $(.)^p$ is related to Newton sub-iterations within each physical time step, which are used to improve time accuracy. These sub-iterations minimize the linearization and factorization errors and help drive the left-hand side of Eq. (2.34) to zero.

Inviscid numerical fluxes, $\hat{F}_{i+1/2,k}$ and $\hat{G}_{i,k+1/2}$, are evaluated by means of the Osher's third-order accurate, upwind-biased scheme [13]. Linearization of the left-hand side of Eq. (2.34) is performed by evaluating the flux Jacobian matrices, $\hat{A}$ and $\hat{B}$, with the Steger and Warming flux-vector splitting [46]. The viscous numerical flux $\hat{S}_{i,k+1/2}$ is computed with second-order central differences. Furthermore, a Total Variation Diminishing (TVD) flux limiter suggested by Rai and Chakravarthy [39] is applied to minimize numerical oscillations at shocks developed at transonic speeds. Grid movement and deformation compatibility is obtained by using the methodology presented by Tamura and Fugii [47].

a. Steger and Warming Flux Vector Splitting

The flux vectors $\hat{F}(Q)$ and $\hat{G}(Q)$ can be split into two parts. This is accomplished by considering the fact that the Jacobian matrices associated with the fluxes have a complete set of linear independent eigenvectors and, then, can be split into subvectors. The equations for the flux $\hat{F}$ are given below and the ones for flux $\hat{G}$ are similar.

$$\hat{F} = \frac{\partial \hat{F}}{\partial \hat{Q}} \hat{Q} = \hat{A}\hat{Q} = \Sigma \Lambda \Sigma^{-1} \hat{Q} \,, \tag{2.36}$$

where:

$$\Lambda = \begin{bmatrix} \lambda_1 & 0 & 0 & 0 \\ 0 & \lambda_2 & 0 & 0 \\ 0 & 0 & \lambda_3 & 0 \\ 0 & 0 & 0 & \lambda_4 \end{bmatrix} = \begin{bmatrix} u & 0 & 0 & 0 \\ 0 & u & 0 & 0 \\ 0 & 0 & u+c & 0 \\ 0 & 0 & 0 & u-c \end{bmatrix} \tag{2.37}$$

Any eigenvalue λ_l can be written as:

$$\lambda_l = \lambda_l^+ + \lambda_l^- \tag{2.38}$$

where:

$$\lambda_l^+ = \frac{\lambda_l + |\lambda_l|}{2} \quad \text{and} \quad \lambda_l^- = \frac{\lambda_l - |\lambda_l|}{2} \tag{2.39}$$

Therefore, matrix Λ can be split into to other diagonal matrices,

$$\Lambda = \Lambda^+ + \Lambda^- \tag{2.40}$$

where the diagonal entries of Λ^+ and Λ^- are λ_l^+ and λ_l^-, respectively.

Finally, applying Eq. (2.40) to Eq. (2.36), the numerical flux $\hat{F}$ can be expressed

as:

$$\hat{F} = \Sigma(\Lambda^+ + \Lambda^-)\Sigma^{-1}\hat{Q}$$
$$\hat{F} = (\hat{A}^+ + \hat{A}^-)\hat{Q} \tag{2.41}$$

where:

$$\hat{A}^+ = \Sigma\Lambda^+\Sigma^{-1}\ , \quad \hat{A}^- = \Sigma\Lambda^-\Sigma^{-1}\ , \text{and} \quad \hat{A} = \hat{A}^+ + \hat{A}^- \tag{2.42}$$

b. Osher Upwind Scheme

A detailed explanation of the Osher scheme is presented in [13]. Nevertheless, some comments must be made to better explain the interaction of the Osher method with the methodology for treating deforming grids. In order to facilitate notation, the hats on the fluxes will be dropped.

For a first-order Osher scheme, the numerical fluxes are updated using:

$$Q_i^{n+1} = Q_i^n - \frac{\Delta\tau}{\Delta\xi}\left[\int_{Q_{i-1}}^{Q_i} A^+ dQ + \int_{Q_i}^{Q_{i+1}} A^- dQ\right] \tag{2.43}$$

The integrals of Eq. (2.43) are evaluated on the subpaths shown in Fig. 2.1 according to:

$$\begin{aligned}\int_{Q_{i-1}}^{Q_i} A^+ dQ + \int_{Q_i}^{Q_{i+1}} A^- dQ = \quad & F(\xi, Q_{i+1}) - F(\xi, Q_i) \\ & + \int_{Q_{i-1}}^{Q_{i-2/3}} A^+ \left(\frac{dQ}{ds}\right)_1 ds + \int_{Q_{i-2/3}}^{Q_{i-1/3}} A^+ \left(\frac{dQ}{ds}\right)_2 ds \\ & + \int_{Q_{i-1/3}}^{Q_i} A^+ \left(\frac{dQ}{ds}\right)_3 ds - \int_{Q_i}^{Q_{i+1/3}} A^+ \left(\frac{dQ}{ds}\right)_4 ds \\ & - \int_{Q_{i+1/3}}^{Q_{i+2/3}} A^+ \left(\frac{dQ}{ds}\right)_5 ds - \int_{Q_{i+2/3}}^{Q_{i+1}} A^+ \left(\frac{dQ}{ds}\right)_6 ds\end{aligned} \tag{2.44}$$

The point where the metrics are evaluated can be chosen. For instance, one can define:

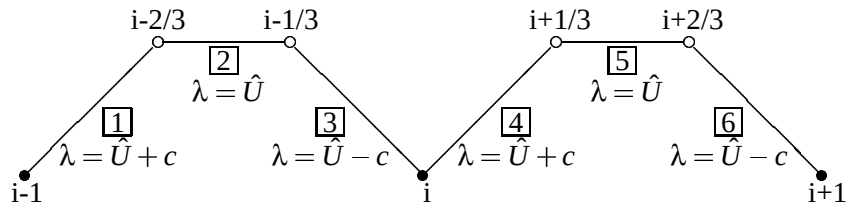

Figure 2.1. Paths of Integration for the Osher Scheme

$$
\begin{aligned}
F(\xi, Q) &= F(\xi_{i-1/2}, Q) \qquad \text{when evaluating} \qquad \textstyle\int_{Q_{i-1}}^{Q_i} A^+ dQ \\
F(\xi, Q) &= F(\xi_{i+1/2}, Q) \qquad \text{when evaluating} \qquad \textstyle\int_{Q_i}^{Q_{i+1}} A^- dQ
\end{aligned}
\tag{2.45}
$$

The choice of the mid-point of the interval, $\xi_{i\pm 1/2}$, is quite convenient because it requires only about half of the computations for each time step. This is possible because some terms that are evaluated in the calculation of the numerical flux, for a particular interval, are equal to terms evaluated for the previous one. Thus, these terms do not need to be evaluated again, saving computational time. This is called telescopic property and is explained in more detail in [13]. Another consequence of using mid-point metrics is that it also allows the numerical scheme to satisfy the conservation in the discretized form of the equations, which is one of the requirements for a moving grid solution.

For a third-order accurate Osher scheme, Eq. (2.43) is changed to:

$$
\begin{aligned}
Q_i^{n+1} \quad = \quad & -\Delta\tau \left[\frac{Q_i^p - Q_i^n}{\Delta\tau} + \frac{F_{i+1/2}^p - F_{i-1/2}^p}{\Delta\xi} \right] \\
& - \frac{\Delta\tau}{2\Delta\xi} [\Delta F^+(Q_{i-1}, Q_i, \xi_{i+1/2}) - \Delta F^+(Q_{i-2}, Q_{i-1}, \xi_{i-1/2})]^p \\
& + \frac{\Delta\tau}{2\Delta\xi} [\Delta F^-(Q_{i+1}, Q_{i+2}, \xi_{i+1/2}) - \Delta F^-(Q_i, Q_{i+1}, \xi_{i-1/2})]^p
\end{aligned}
\tag{2.46}
$$

c. TVD Flux Limiter

The TVD scheme used in the present work is based on [39]. The fluxes ΔF^+ and ΔF^- on Eq. (2.46) are modified to achieve the TVD property. The flux limiters are obtained with

the help of an entropy function, defined as:

$$V(Q) = -\rho log(p/\rho^{\gamma}) \tag{2.47}$$

The idea behind this flux limiter is to change the fluxes when the gradient of this entropy function exceeds a certain limit, which is what occurs when a shock wave exists. Then, the gradient of the entropy function described by Eq. (2.47) can be expressed as:

$$V_Q = \nabla_Q V = -\frac{(\gamma-1)}{p}\left[e + \frac{p}{\gamma-1}\left(-\gamma-1+log\frac{p}{\rho^{\gamma}}\right), -\rho u, -\rho v, \rho\right]^T \tag{2.48}$$

The modification of the fluxes is done for each subpath. Defining $DV_Q^{(m)}$ as the change in the entropy function along he subpath m,

$$DV_Q^{(m)} = (V_Q)_{i+m/3} - (V_Q)_{i+(m-1)/3}\ , \quad m = 1,2,3 \tag{2.49}$$

and the modified fluxes $(\Delta\bar{F}^{+})^{(m)}$ and $(\Delta\bar{F}^{-})^{(m)}$ are given by:

$$[\Delta\bar{F}^{+}(Q_{i-1},Q_i,\xi)]^{(m)} = [\Delta F^{+}(Q_i,Q_{i+1},\xi)]^{(m)} \times max[0, min(\phi, N/D)] \tag{2.50}$$

where

$$\begin{aligned} &1.0 \leq \phi \leq 2.0 \\ &N = < [\Delta F^{+}(Q_{i-1},Q_i,\xi)]^{(m)}, [DV_Q(Q_i,Q_{i+1},\xi)]^{(m)} > \\ &D = < [\Delta F^{+}(Q_i,Q_{i+1},\xi)]^{(m)}, [DV_Q(Q_i,Q_{i+1},\xi)]^{(m)} > \end{aligned} \tag{2.51}$$

and

$$[\Delta\bar{F}^{-}(Q_i,Q_{i+1},\xi)]^{(m)} = [\Delta F^{-}(Q_{i-1},Q_i,\xi)]^{(m)} \times max[0, min(\phi, N/D)] \tag{2.52}$$

where

$$\begin{aligned} &1.0 \leq \phi \leq 2.0 \\ &N = < [\Delta F^{-}(Q_i,Q_{i+1},\xi)]^{(m)}, [DV_Q(Q_{i-1},Q_i,\xi)]^{(m)} > \\ &D = < [\Delta F^{-}(Q_{i-1},Q_i,\xi)]^{(m)}, [DV_Q(Q_{i-1},Q_i,\xi)]^{(m)} > \end{aligned} \tag{2.53}$$

The variables N and D represent the inner product of the vectors contained within the symbols $< >$.

d. Deforming-Grid Compatibility

The N-S equations represented by Eq. (2.8) are compatible with deforming- and moving-grid problems, as shown in Appendix A. Theoretically, the N-S equations can handle problems in which both ξ_t and ζ_t are different from zero. Computationally, the numerical scheme must be conservative both in time and space in order to guarantee deforming-grid compatibility.

Thomas and Lombard [49] suggest the use of the Geometric Conservation Law (GCL) for solving problems involving a changing or deforming grid. As shown in Appendix A, the GCL is analytically satisfied by the unsteady N-S equations written in generalized coordinates form. Nonetheless, in order to satisfy the GCL numerically, the metrics associated with computations of the numerical fluxes must be calculated using a conservative scheme. They suggest the following conservative scheme for the 3-D metrics:

$$\begin{aligned} \hat{\xi}_x &= (y_\eta z)_\zeta - (y_\zeta z)_\eta \qquad & \hat{\eta}_x &= (y_\zeta z)_\xi - (y_\xi z)_\zeta \\ \hat{\zeta}_x &= (y_\xi z)_\eta - (y_\eta z)_\xi & & etc. \end{aligned} \tag{2.54}$$

For 2-D metrics, Eq. (2.54) is reduced to the form presented in Eq. (2.7) and the scheme is automatically conservative in space. Therefore, the numerical scheme used in the present work is conservative in space. Thomas and Lombard [49] also suggest the inclusion of an extra term in the discretized equations to achieve moving-grid compatibility. According to their approach, the Osher scheme presented in section b would become:

$$\begin{gathered} \left[IJ^{-1} + h_\xi(\nabla_\xi \tilde{A}^+_{i,k} + \Delta_\xi \tilde{A}^-_{i,k})^p\right] \Delta Q^*_{i,k} = -r^p_{i,k} \\ \left[IJ^{-1} + h_\zeta(\nabla_\zeta \tilde{B}^+_{i,k} + \Delta_\zeta \tilde{B}^-_{i,k} - Re^{-1}\delta_\zeta \tilde{M}_{i,k})^p\right] (Q^{p+1}_{i,k} - Q^p_{i,k}) = IJ^{-1}\Delta Q^*_{i,k} \end{gathered} \tag{2.55}$$

where:

$$
\begin{aligned}
r^p_{i,k} = \quad & J^{-1}(Q^p_{i,k} - Q^n_{i,k}) + \Delta(J^{-1})Q^n_{i,k} + h_\xi(\hat{F}_{i+1/2,k} - \hat{F}_{i-1/2,k})^p \\
& + h_\zeta(\hat{G}_{i,k+1/2} - \hat{G}_{i,k-1/2})^p - Re^{-1}h_\zeta(\hat{S}_{i,k+1/2} - \hat{S}_{i,k-1/2})^p
\end{aligned}
\tag{2.56}
$$

Now, the $(\tilde{.})$ terms represent Jacobians with respect to Q, or $\partial(.)/\partial Q$, instead of $\hat{Q}$ and the term $\Delta(J^{-1})$ is obtained by the GCL (see Appendix B):

$$
\Delta(J^{-1}) = -\Delta\tau[(\hat{\xi}_t)^n_\xi + (\hat{\zeta}_t)^n_\zeta] \tag{2.57}
$$

One of the differences between Eq. (2.55) and Eq. (2.34) is the way they are solved. The former solves for Q while the latter solves for $\hat{Q}$. The other difference is the extra term $\Delta(J^{-1})Q^n_{i,k}$ in the RHS of Eq. (2.55). The presence of this term is due merely to the fact that one of the equations is solved for Q while the other is solved for $\hat{Q}$. This can be seen by expanding the term $\partial\hat{Q}/\partial\tau$:

$$
\frac{\partial\hat{Q}}{\partial\tau} = \frac{\partial(J^{-1}Q)}{\partial\tau} = Q\frac{\partial(J^{-1})}{\partial\tau} + (J^{-1})\frac{\partial Q}{\partial\tau} \tag{2.58}
$$

Writing Eq. (2.58) in discrete form:

$$
\frac{\Delta\hat{Q}}{\Delta\tau} = Q\frac{\Delta(J^{-1})}{\Delta\tau} + (J^{-1})\frac{\Delta Q}{\Delta\tau} \tag{2.59}
$$

Multiplying Eq. (2.59) by $\Delta\tau$ and using a finite difference approximation:

$$
\hat{Q}^p_{i,k} - \hat{Q}^n_{i,k} = Q^n\Delta(J^{-1}) + (J^{-1})^n(Q^p_{i,k} - Q^n_{i,k}) \tag{2.60}
$$

Substituting Eq. (2.60) into Eq. (2.35), one obtains Eq. (2.56), which is the method based on the GCL suggested by Thomas and Lombard [49]. Therefore, Eq. (2.34) is mathematically equivalent to Eq. (2.55). In order for them to be numerically equivalent, according to the work of Tamura and Fujii [47], the scheme must also be conservative in time. This feature is achieved by carefully choosing the Jacobian to be used in Eq. (2.35). They suggest using:

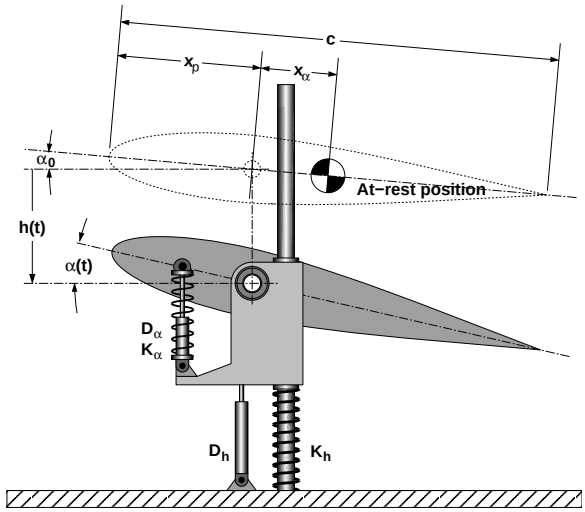

Figure 2.2. Schematic of the Spring/Mass/Damper System

$$(J^{-1})' = \frac{1}{2}\left[(J^{-1})^n + (J^{-1})^{n+1}\right] \tag{2.61}$$

B. STRUCTURAL DYNAMICS

Structural dynamics modeling is based on a two-degree-of-freedom spring/mass/damper system, shown in Fig. 2.2, to simulate the bending and twisting of a wing section.

1. Governing Equations

The equations governing a two-degree-of-freedom motion of structure are:

$$\begin{aligned} m\ddot{h} - S_\alpha\ddot{\alpha} + D_h\dot{h} + m\omega_h^2 h &= L \\ -S_\alpha\ddot{h} + I_\alpha\ddot{\alpha} + D_\alpha\dot{\alpha} + I_\alpha\omega_\alpha^2(\alpha - \alpha_0) &= M \end{aligned} \tag{2.62}$$

where the dots represent differentiation with respect to time.

Equations (2.62) are nondimensionalized using reference length $\tilde{c}$, reference velocity $\tilde{a}_\infty$,

reference mass $\tilde{\rho}_\infty \pi(\tilde{c}/2)^2$, and reference inertia $\tilde{\rho}_\infty \pi(\tilde{c}/2)^2 \tilde{c}^2$. Rewriting Eq. (2.62) in matrix notation:

$$[M]\{X\}'' + [D]\{X\}' + [K]\{X\} = \{F\} \tag{2.63}$$

where:

$$[M] = \begin{bmatrix} m & -S_\alpha \\ -S_\alpha & I_\alpha \end{bmatrix} \qquad [D] = \begin{bmatrix} 2\delta_h m M_\infty k_h & 0 \\ 0 & 2\delta_\alpha I_\alpha M_\infty k_\alpha \end{bmatrix}$$

$$\{K\} = \begin{bmatrix} m M_\infty^2 k_h^2 & 0 \\ 0 & I_\alpha M_\infty^2 k_\alpha^2 \end{bmatrix} \qquad \{X\} = \begin{Bmatrix} h \\ \alpha - \alpha_0 \end{Bmatrix} \tag{2.64}$$

and

$$\{F\} = \frac{2}{\pi} M_\infty^2 \begin{Bmatrix} c_L \\ c_m \end{Bmatrix} \tag{2.65}$$

where the primes denote differentiation with respect to dimensionless time, $\tau = \tilde{t}\tilde{a}_\infty/\tilde{c}$, and the other parameters (i.e., m, I_α, etc.) are now nondimensional.

2. Numerical Technique

Equation (2.63) is a system of two, coupled, second-order, ordinary differential equations. Coupling is obtained through the terms containing S_α and the dependence of c_L and c_m on h and α. The system is nonlinear through the nonlinearity of c_L and c_m. Linearization is introduced by treating c_L and c_m as constants, computed from the previous time-step of the flow solution.

Simulations with single-degree-of-freedom may be performed by setting $S_\alpha = 0$ and either $m = \infty$ and $\omega_h = 0$ or $I_\alpha = \infty$ and $\omega_\alpha = 0$ for pitching-only or plunging-only motions, respectively.

Equation (2.63) is advanced in time by solving for the second derivative of the dependent variable X:

$$\{X\}'' = [M]^{-1}\{F\} - [M]^{-1}[K]\{X\} - [M]^{-1}[D]\{X\}' \tag{2.66}$$

Rewriting the result as a system of two, coupled, first-order equations:

$$\begin{cases} \{X\}' = \{Y\} \\ \{Y\}' = [M]^{-1}\{F\} - [M]^{-1}[K]\{X\} - [M]^{-1}[D]\{Y\} \end{cases} \tag{2.67}$$

Finally, time integration is performed using a first-order accurate explicit Euler scheme. The use of higher order methods does not improve the quality of the solution because the time steps required for the stability of the unsteady N-S equations yield very high resolution in time for Eq. (2.63).

III. BOUNDARY CONDITIONS AND MULTI-BLOCK PROCESSING

This chapter examines some background necessary for solving the problems investigated in this dissertation. It is presented as a separate chapter because some of the material is quite specific for the layout of the grids used throughout this investigation. Furthermore, this chapter contains an important discussion about all the boundary conditions necessary for the multi-block grid computations. This chapter also includes information that is essential in order to apply the theory discussed in Chapter II.

A. THREE-BLOCK GRID

Modeling of the wind tunnel geometry requires a mesh that is very long in the streamwise direction, compared to its height. Accurate computation of the boundary layer is most easily performed on a C-grid. However, construction of a single-block, C-grid would require a highly skewed grid and an excessive number of grid points in regions far from the airfoil. Furthermore, maintaining grid orthogonality close to the walls using a single-block grid would be impossible. These problems can be minimized by using a three-block grid, shown schematically in Fig. 3.1, where the governing equations are solved in each block, separately.

A similar situation occurs with respect to the airfoil-in-ground-effect computations. Because the ground plane is close to the airfoil section, the use of a single-block, C-grid would require a very skewed mesh in the vertical direction. Once again, a three-block grid approach can be used instead of a single-block grid, as shown in the schematic in Fig. 3.2.

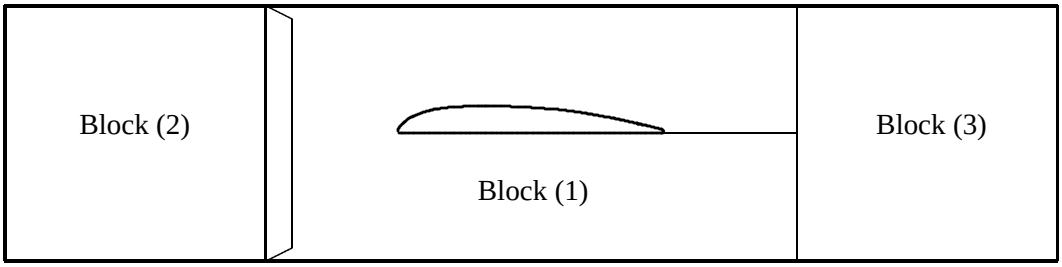

Figure 3.1. Schematic of the Three-Block Grid for the Flutter Problem

The two problems of this dissertation require two different layouts for the three-block grids. The transonic flutter problem asks for the layout presented in Fig. 3.1. The blocks are placed in line. The first, or block (1), is placed around the airfoil. The second, or block (2), discretizes the region upstream of the first block and the third, or block (3), completes the downstream domain. For the airfoil in ground effect, the layout used is shown in Fig. 3.2. The main block, or block (1), represents the region around the airfoil and also the wake behind it. The second, or block (2), fills the region upstream of the first one. The third, or block (3), completes the domain above the first two blocks.

In both problems, solving the N-S equations in all three blocks is not necessary. Blocks (2) and (3) are always coarse enough to allow the use of Euler equations. Therefore, N-S equations are solved only in block (1) for both problems.

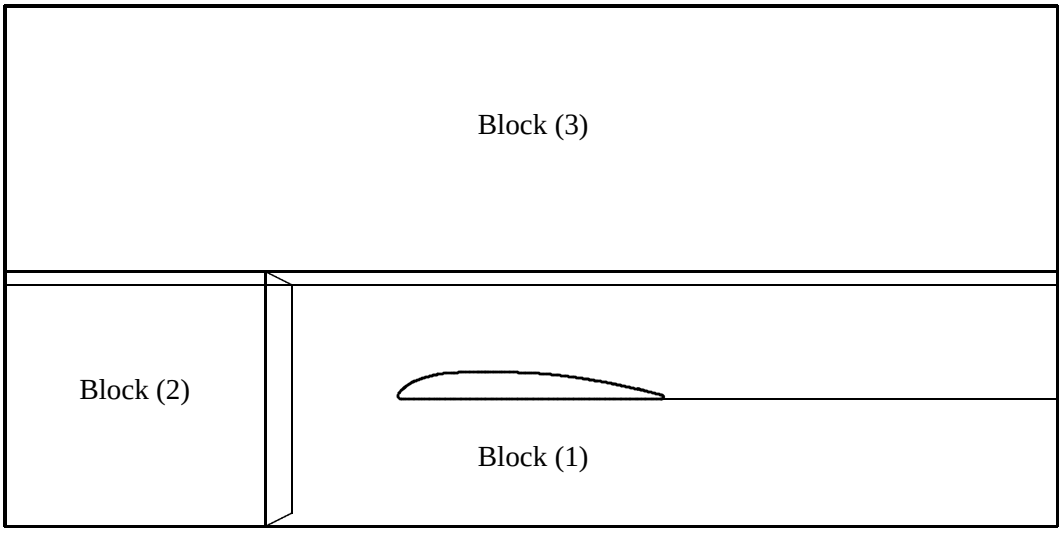

Figure 3.2. Schematic of the Three-Block Grid for the Airfoil-in-Ground-Effect Problem

B. BOUNDARY CONDITIONS

This section describes the boundary conditions used for the two different problems solved in the present work. The boundary condition for the surface of the airfoil is the same for both problems and is described next. The boundary conditions that are specific for each problem are described in the sections associated with each problem.

For inviscid flow solutions, the viscous terms on the RHS of Eq. (2.1) are set to zero, and the flow-tangency boundary condition is used at the surface of the airfoil. For Navier-Stokes solutions, the no-slip condition is applied. Density and pressure are extrapolated to the surface for both Euler and Navier-Stokes solutions.

For unsteady motions, the flow-tangency and no-slip conditions are modified to include the local motion of the airfoil, which also contributes to the pressure on the surface. Therefore, the momentum equation normal to the surface (ζ direction) is solved to predict the pressure for a

viscous flow more accurately

$$\partial_\zeta p|_{wall} = -\frac{1}{\nabla^2\zeta}\left[\rho\partial_t \left\{ \begin{array}{c} \dot{x}|_{wall} \\ \\ \dot{y}|_{wall} \end{array} \right\} \cdot \nabla\zeta + \partial_\zeta \rho|_{wall} \nabla\xi \cdot \nabla\zeta \right] \tag{3.1}$$

where $\dot{x}|_{wall}$ and $\dot{y}|_{wall}$ are the components of the airfoil velocity. Furthermore, $\nabla\xi \cdot \nabla\zeta = 0$ when assuming that the grid is orthogonal at the surface. If the airfoil is stationary, the normal pressure gradient vanishes in agreement with boundary-layer theory.

1. Wind-Tunnel Problem

The flow at the wind tunnel sections blocks (2) and (3) is assumed to be inviscid and the Euler equations are solved in these domains. The tunnel walls are assumed to be porous, and two types of porous wall boundary conditions are applied. First, the porous boundary condition is applied according to the formulation presented by Mokry et al. [35] (Chapter 2.0 WALL BOUNDARY CONDITION). Pressure, density, and x-direction velocity, u, are extrapolated from the interior points of the grid. The z-direction velocity, w, is obtained according to Eq. (3.2)

$$\frac{w}{U_\infty} = \sigma \, \frac{p - p_{plenum}}{\rho_\infty U_\infty^2} \tag{3.2}$$

where σ is the porosity parameter of the wall and p_{plenum} is the pressure at the plenum chamber. For $\sigma = 0$, for example, this boundary condition is the same as the flow tangency condition and the wall is treated as being completely solid.

The porous-wall boundary condition can be further modified to account for viscous effects present at this region of the walls as follows. The tangential velocity at the wall is set equal to zero, $u = 0$, and the normal velocity, w, is still obtained according to Eq. (3.2). In this work, this model is denoted as the porous, viscous boundary condition.

This treatment for the porous-wall boundary condition is quite different from the one adopted in the previous work [11]. In that study, the porous boundary was modeled by treating some grid

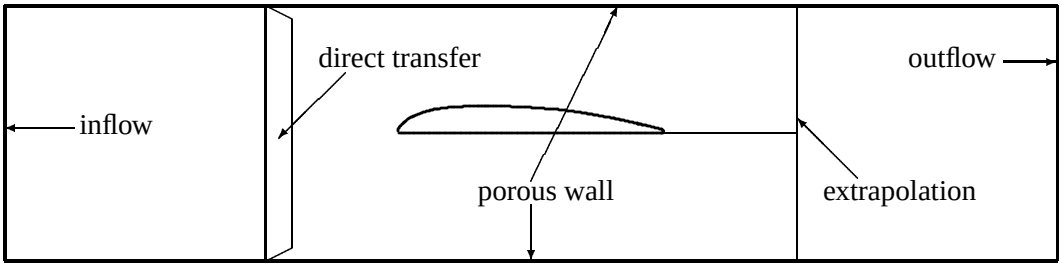

Figure 3.3. Boundary Conditions for the Flutter Problem

cells as solid walls (applying flow tangency) and the others as holes (extrapolating the velocity vector from the interior points). For the previous approach, the grid needed to be approximately uniformly spaced at the porous region. Furthermore, only certain discrete choices in the porosity were allowed. Values of porosity, such as 17%, were quite difficult to apply due to the limited number of grid cells along the porous region of the walls. The new model is not dependent on the streamwise grid spacing at the walls and also allows for a continuous variation on the porosity parameter.

Inflow and outflow boundary conditions are imposed in blocks (2) and (3), respectively. For the inflow boundary, flow properties such as pressure, temperature, and velocity are specified while the density is extrapolated from the neighbor interior points. Static pressure is specified for the outflow boundary condition and all other properties are extrapolated from the interior. Extrapolations in both cases are performed by using Riemann invariants.

The boundaries on the left of domain (1) and right of domain (2) are updated by means of an overlapping region, as shown in Fig. 3.3. There is an overlapping between the blocks and the flow variables are transferred directly from one domain to the other. The boundary conditions at the right of domain (1) are updated via linear extrapolation from domain (3) and vice-versa.

2. Airfoil in Ground Effect

The flow at the grid blocks (2) and (3) is assumed to be inviscid and the Euler equations are solved in these domains. The ground plane is assumed to be a symmetry plane. Therefore, it can be modeled as a solid wall where the symmetry boundary condition is given by Eq. (3.3).

$$\left[\frac{\partial q}{\partial n}\right]_{\text{wall}} = 0 \tag{3.3}$$

where n represents the normal direction at the wall.

The types of boundary conditions used for all boundaries of the three-block grid are shown in Fig. 3.4. Inflow boundary conditions are applied to the points on the left boundaries of blocks (2) and (3) and also to the upper boundary of block (3). Outflow boundary conditions are specified to the points on the right boundary of blocks (1) and (3).

The boundaries on the left of domain (1) and right of domain (2) are updated by means of an overlapping region, as shown in Fig. 3.4. There is an overlapping of the blocks and the flow variables are transferred directly from one domain to the other. The same type of boundary condition is used between blocks (1) and (3), and between (2) and (3). Because of the overlapping regions, direct transfer of the flow variables (ρ,ρu,ρw,e) can be used.

3. Trailing Edge Boundary Condition

The trailing edge (TE) boundary condition is a crucial issue in both steady-state and unsteady computations. A schematic of a C-grid near the trailing edge is shown in Fig. 3.5. The cut is the region of the computational domain corresponding to points for which $(1 \leq i \leq i_l, k = 1)$ and $(i_u \leq i \leq i_{max}, k = 1)$. These points are coincident in the physical domain. The trailing edge point in the physical domain corresponds to the points $(i = i_l)$ and $(i = i_u)$ in the computational domain. The points along the cut, including the trailing edge, are shown separated in Fig. 3.5 just for clarity.

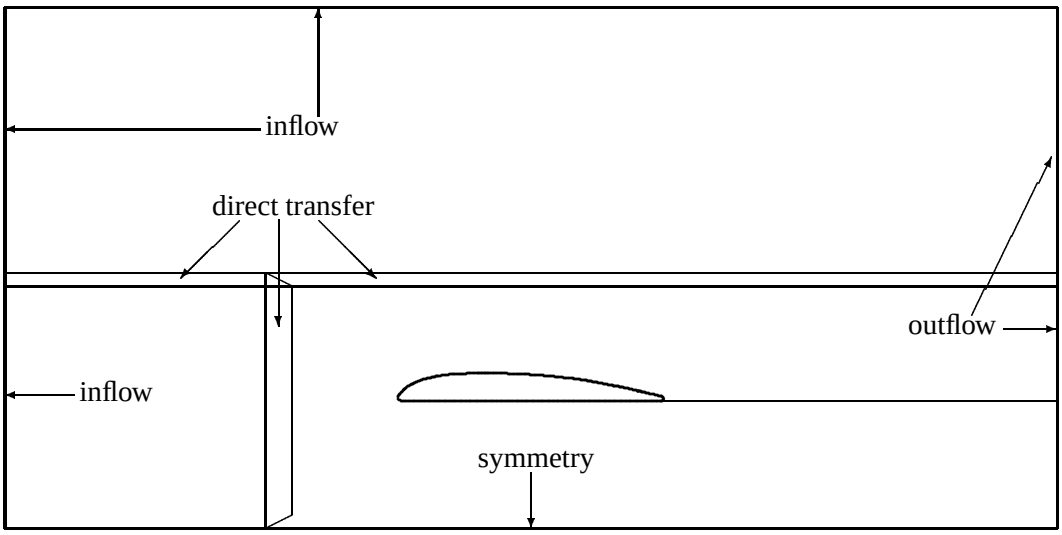

Figure 3.4. Boundary Conditions for the Airfoil-in-Ground-Effect Problem

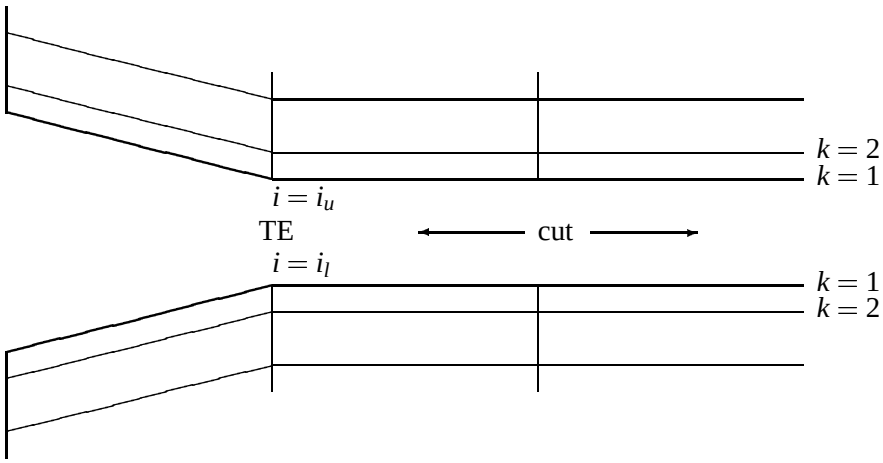

Figure 3.5. Schematic of a C-Grid near the Trailing Edge

The boundary condition at the cut of a C-grid can be done either explicitly or implicitly. In the present method, this boundary condition is computed explicitly, after the flow tangency or the no-slip condition is applied to the surface of the airfoil. The flow variables at the cut, $k = 1$, are calculated by averaging the upper and lower neighboring points for $k = 2$. Some options exist when one must decide how to implement the explicit boundary condition at the trailing edge. Three possibilities for this implementation exist:

- use the averaged value from points at $(i_u, 2)$ and $(i_l, 2)$;
- treat the trailing edge as two different points (no averaging);
- use the averaged value from points at $(i_u, 1)$ and $(i_l, 1)$.

The first option is the most obvious because it is just an extension of the boundary condition applied at the cut of the C-grid. However, the first option is not the most suitable one because it does not enforce the no-slip or the flow-tangency condition at the trailing edge. These boundary conditions are overwritten when computing the average of the off-surface points ($k = 2$). In this work, the second alternative is called the "free TE boundary condition." The no-slip or the flow-tangency condition is applied to the TE. However, because the TE is treated as two different points in the computational domain, a discontinuity may occur at the TE since the two points are the same in the physical domain. The last option, called averaged TE, appears to be the most consistent one for the present work because, in terms of discretization of the physical domain, the points of the cut corresponding to the TE are the same. Furthermore, it is guaranteed that the no-slip condition or the flow-tangency condition is maintained at the TE since these conditions are applied for $k = 1$ before averaging.

The influence of applying the free or the averaged TE is investigated. A single NACA 0012 airfoil oscillating in a combined pitch and plunge motion is used to determine the difference in the

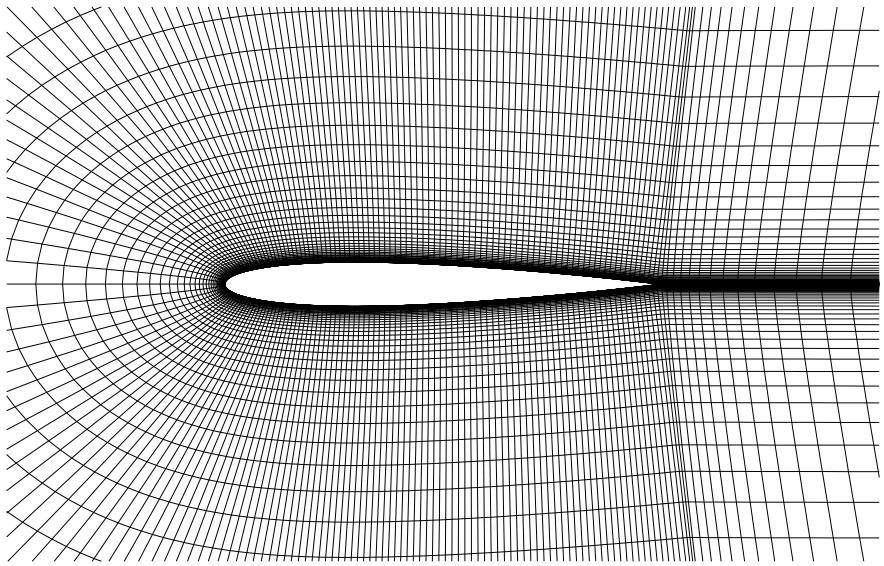

Figure 3.6. Grid around the NACA 0012 Airfoil

solutions for both TE conditions. The reduced frequency of the motion is set to $k = 1.0$ and the pitch and plunge half amplitudes are $\hat{\alpha} = 10$ degrees and $\hat{h} = 1.0$, respectively. Pitch leads plunge by $\phi = 90$ degrees. The pivot point for the pitch motion is chosen to be the half chord or $x_p = 0.5$. The free-stream Mach and Reynolds numbers are $M_\infty = 0.3$ and $Re_\infty = 10^6$, respectively. The B-L turbulence model is applied for the fully turbulent computations. The C-grid is presented in Fig. 3.6 and its dimensions are $i_{max} = 281$ and $k_{max} = 81$.

The non-dimensional equations of motion are given by:

$$h = \hat{h} sin(M_\infty k\tau) \qquad \alpha = \hat{\alpha} sin(M_\infty k\tau + \phi) \tag{3.4}$$

Steady-state computations are performed for $\alpha = 0$ degrees, employing both the averaged and free TE boundary conditions. The pressure distributions over the surface of the airfoil are presented in Fig. 3.7. The match is extremely good for the two solutions. However, no conclusion

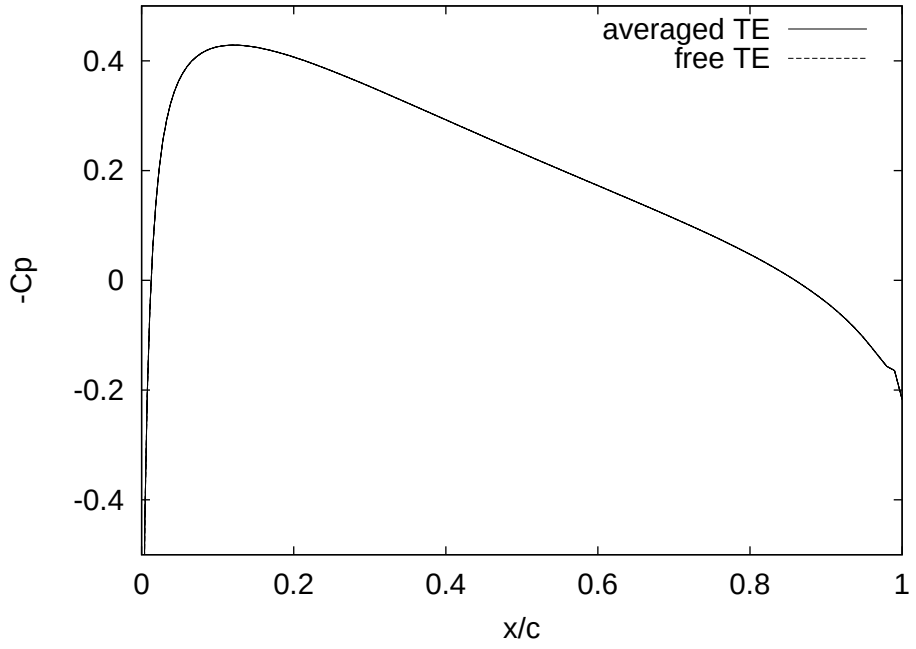

Figure 3.7. Steady-State Solutions for Averaged and Free TE

is drawn from the steady-state case because the flow is symmetric, and this might be the reason for the excellent match.

The motion parameters for the oscillation of the airfoil have been chosen because they force a relatively high induced angle of attack, therefore, allowing dynamic stall to occur. The time history of the aerodynamic coefficients is presented in Fig. 3.8 for both types of boundary conditions. Clearly, the solution is not periodic. For the same type of boundary condition, the curve for the lift coefficients, for example, does not behave periodically.

The pressure distributions for various positions along the cycle are shown in Fig. 3.9. The left-hand side of this figure corresponds to positions along the up stroke and the right-hand side to the down stroke. Although some pressure distributions are not in close agreement for the two TE conditions, the development of the dynamic stall is not dramatically different. In order to better clarify this point, entropy contours during the upstroke part of the motion of the airfoil are shown

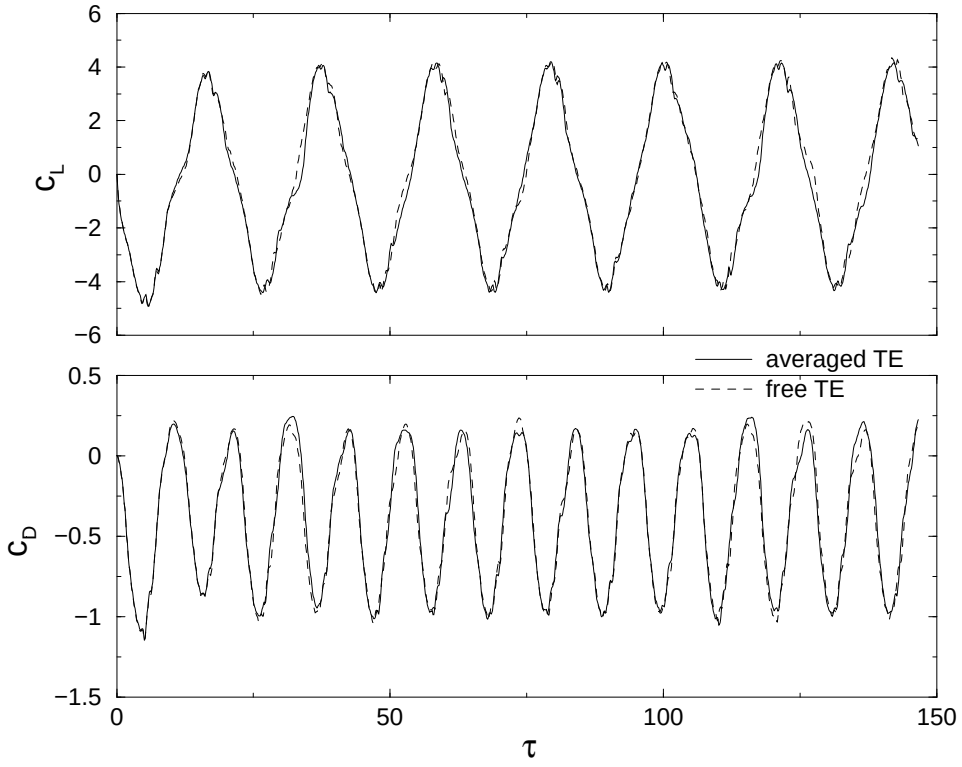

Figure 3.8. History of Lift and Drag Coefficients for the Pitch/Plunge Case

in Fig. 3.10. The vortices generated during the motion are well captured. The left-hand side of Fig. 3.10 represents the averaged TE boundary condition. The free TE boundary condition is represented on the right-hand side. Although the vortices do not match perfectly for the two types of TE boundary condition, their sizes are comparable and the speed with which they convect downstream is approximately the same. Note, also, that the flow is not periodic. This can be seen in Fig. 3.11 in which the variation of the drag coefficient is shown against the lift coefficient. Clearly, the solution is not periodic. However, it stays inside a confined area although it wanders from place to place in that area. This behavior is represented in the Chaos Theory by the Torus Attractor, which is defined, for example, by Petree [38]. This attractor appears to be the same for both types of TE boundary condition. Furthermore, a computation of the thrust coefficient and propulsive efficiency showed that these parameters are virtually the same for both TE conditions ($c_T = 0.40$ and $\eta = 0.21$). As a conclusion from this case, the type of TE boundary condition is apparently not influential when one is interested in quantities that represent an average along the cycle. On the other hand, the fine details of the flow-field, as the development of the dynamic stall, are strongly affected by the type of boundary condition at the trailing edge.

A case with no dynamic stall was also run to evaluate the TE boundary condition. A NACA 0014 airfoil oscillating in pure plunge is computed. The reduced frequency of the motion is $k = 0.4$ with a half amplitude of $\hat{h} = 0.4$. The free-stream Mach and Reynolds numbers are $M = 0.3$ and $Re = 10^6$, respectively. The flow is assumed fully turbulent and the B-L turbulence model is used. The domain is discretized by a 321×91 C-grid shown in Fig. 3.12.

When steady-state computations are performed, they deliver the same solution for both types of TE boundary condition. This is similar to the NACA 0012 airfoil case. Unsteady simulations are also computed for the two types of TE boundary condition. The history of the unsteady lift and drag aerodynamic coefficients is presented in Fig. 3.13. The agreement between the solutions

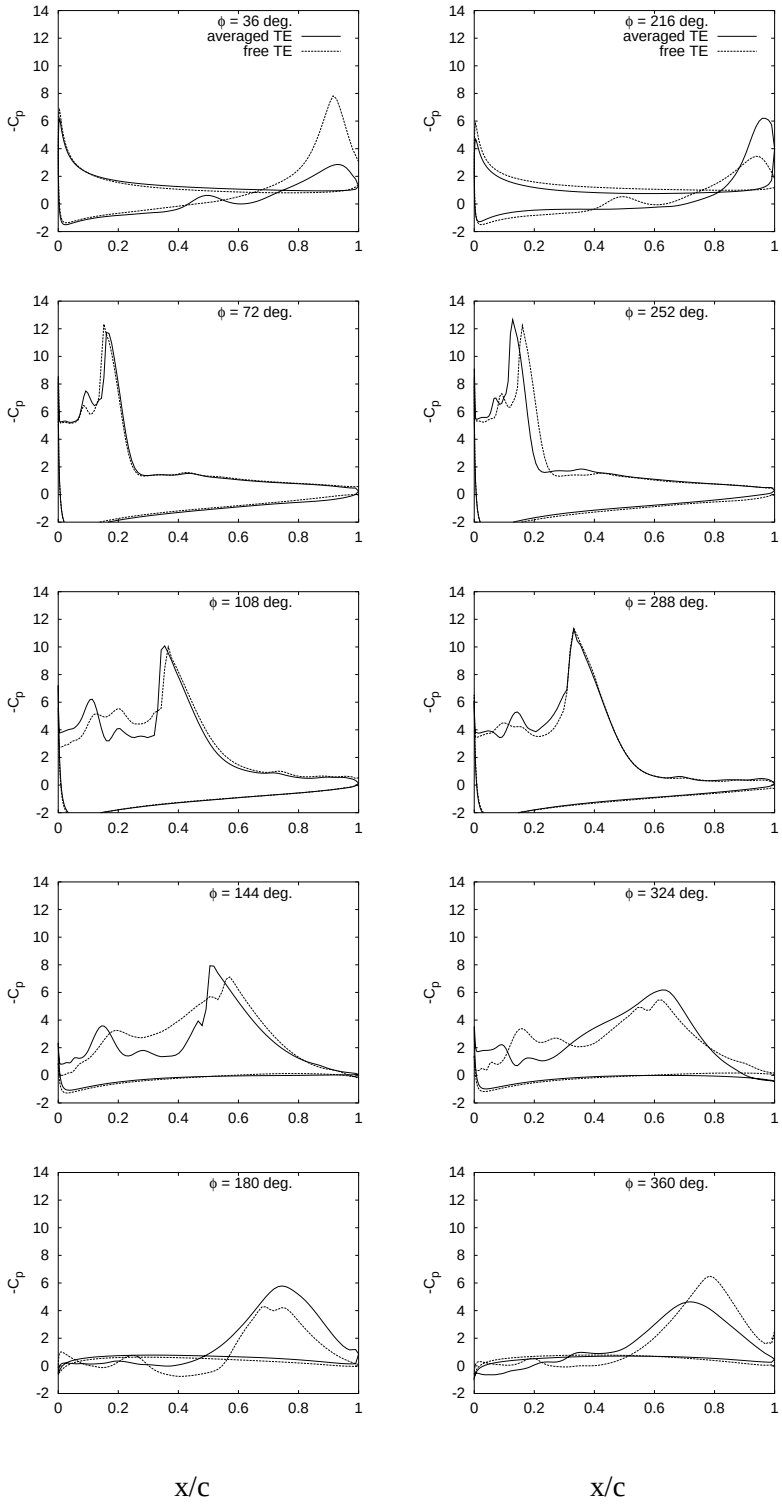

Figure 3.9. Comparison of Pressure Distributions for Averaged and Free TE

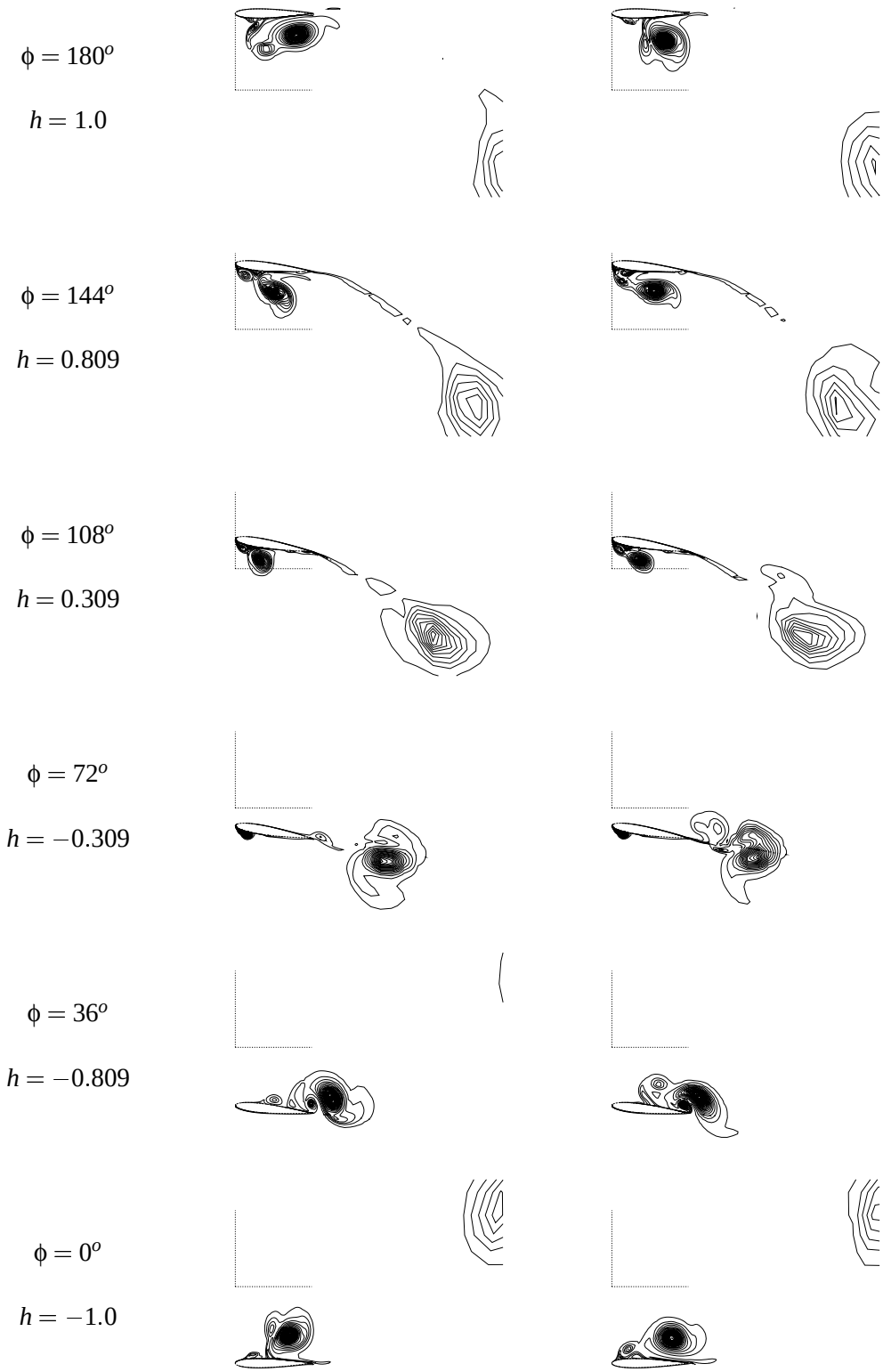

Figure 3.10. Comparison of Pressure Distributions for Averaged and Free TE, NACA 0012, $\hat{\alpha} = 10$ degrees, $M_\infty = 0.3$, $k = 1$, $Re_\infty = 1 \times 10^6$

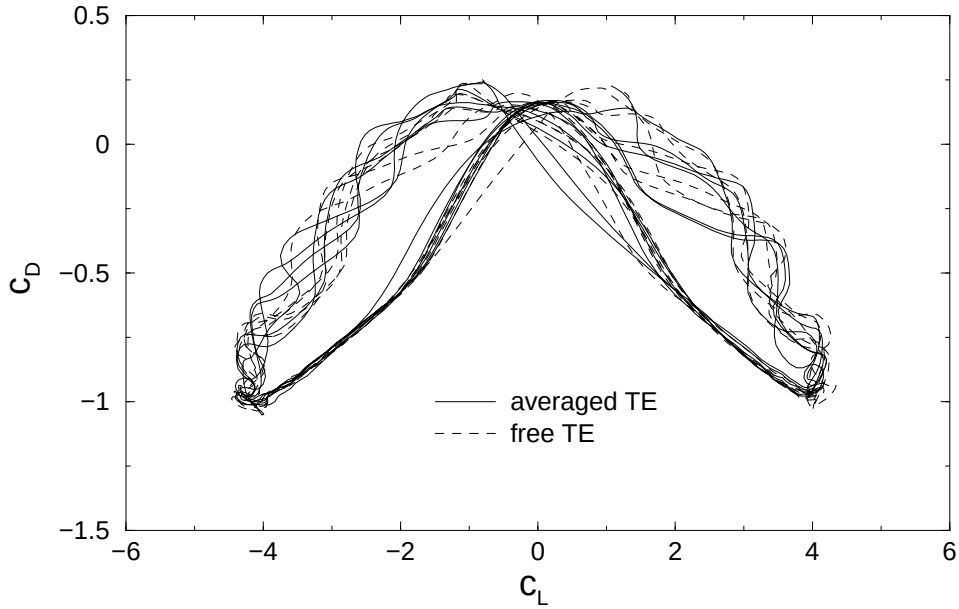

Figure 3.11. Variation of c_D against c_L for the Pitch/Plunge Case

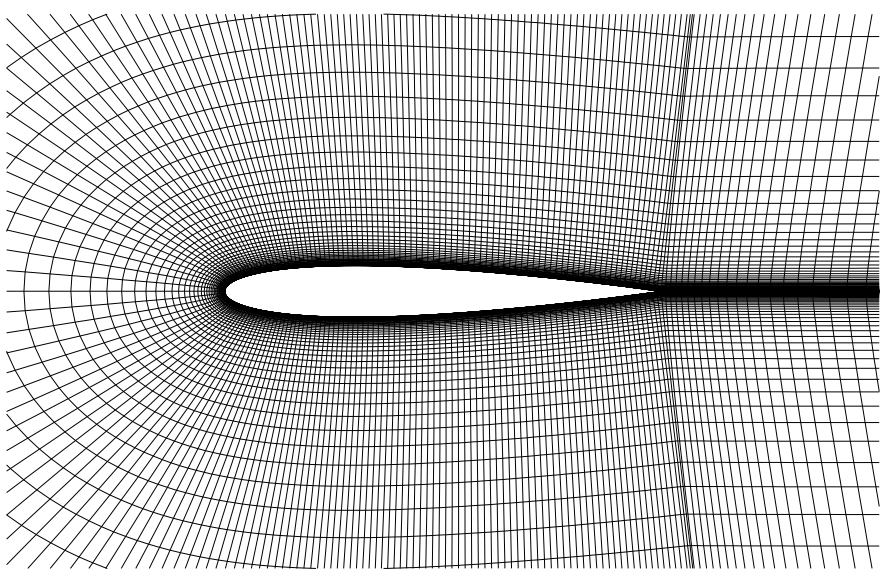

Figure 3.12. Grid around the NACA 0014 Airfoil

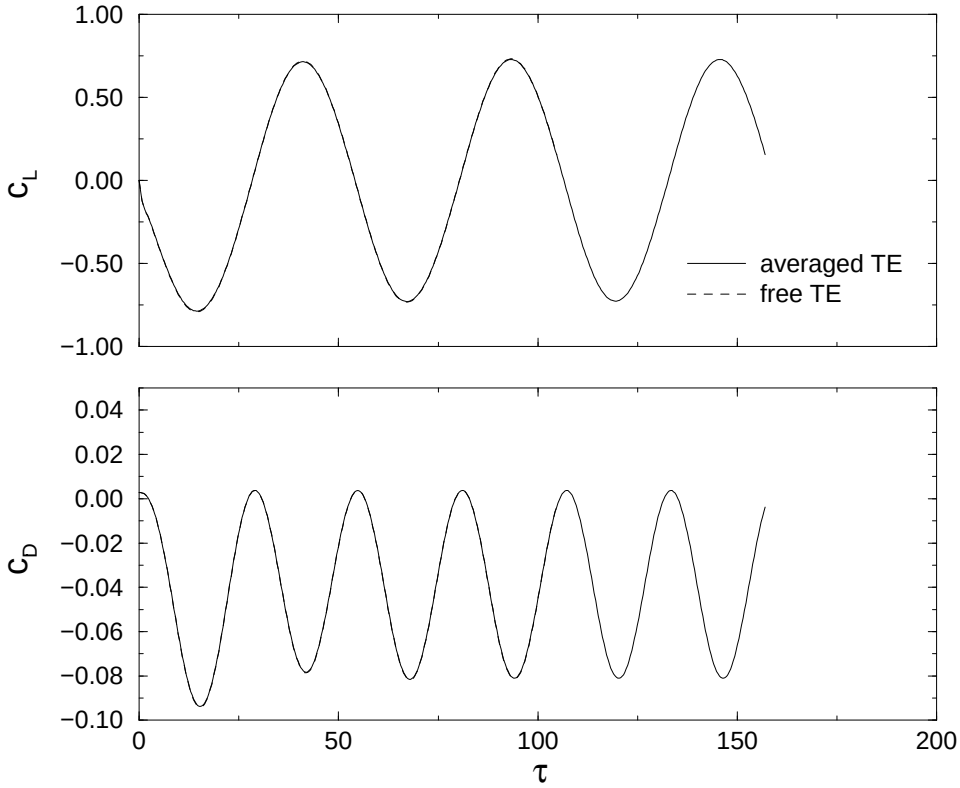

Figure 3.13. History of Lift and Drag Coefficients for the Pure Plunge Case

for the two different boundary conditions is quite good. The thrust coefficient is $c_T = 0.041$ and the propulsive efficiency is $\eta = 0.73$ for both cases. Therefore, in situations where there is no dynamic stall, the difference of applying an averaged TE or a free TE boundary condition is negligible.

Although dynamic stall was computed somewhat differently for the two types of TE boundary condition, the effect on the predicted thrust coefficient, the propulsive efficiency, and the convection speed of the dynamic vortices was minimal. Therefore, the averaged TE boundary condition is used throughout the course of this work.

Another important computation with the averaged TE boundary condition was performed to assess the influence of this boundary condition on the dynamic-stall boundary suggested by Tuncer et al. [53]. They computed the unsteady flow over a NACA 0012 airfoil oscillating in pure plunge

and varied the reduced frequency and the amplitude of the motion to determine the onset of dynamic stall. Their computations, using a free TE boundary condition, showed that the dynamic-stall boundary is given by the equation:

$$\hat{h}k = 0.35 \tag{3.5}$$

Two computations with $k = 1.0$ were performed for $\hat{h} = 0.3$ and $\hat{h} = 0.4$. The first, corresponding to $\hat{h}k = 0.3$, predicted no separation of the flow, in agreement with the dynamic stall boundary given by Eq. 3.5. The second, corresponding to $\hat{h}k = 0.4$, calculated a separated flow during the motion of the airfoil, confirming that the averaged TE boundary condition also delivers the dynamic-stall boundary described by Eq. 3.5.

A second set of computations was performed for the averaged TE boundary condition but, this time, for the NACA 0014 airfoil. The objective was to determine the influence of the shape of the airfoil on the dynamic-stall boundary represented by Eq. 3.5. The reduced frequency was kept equal to $k = 1.0$ while the amplitude of the pure plunge motion, $\hat{h}$, was varied. For $\hat{h} = 0.4$, no separation of the flow was predicted, suggesting that the dynamic-stall boundary might have changed for the NACA 0014 airfoil. A computation with $\hat{h} = 0.5$ showed that the flow was detached from the airfoil surface. These computations are shown schematically in Fig. 3.14, along with the dynamic-stall boundary of Eq. 3.5. Therefore, clearly, the shape of the airfoil has a significant influence on the onset of dynamic stall. For the NACA 0014, the dynamic-stall boundary should be further investigated and it appears that it will be given by:

$$\hat{h}k \geq 0.4 \tag{3.6}$$

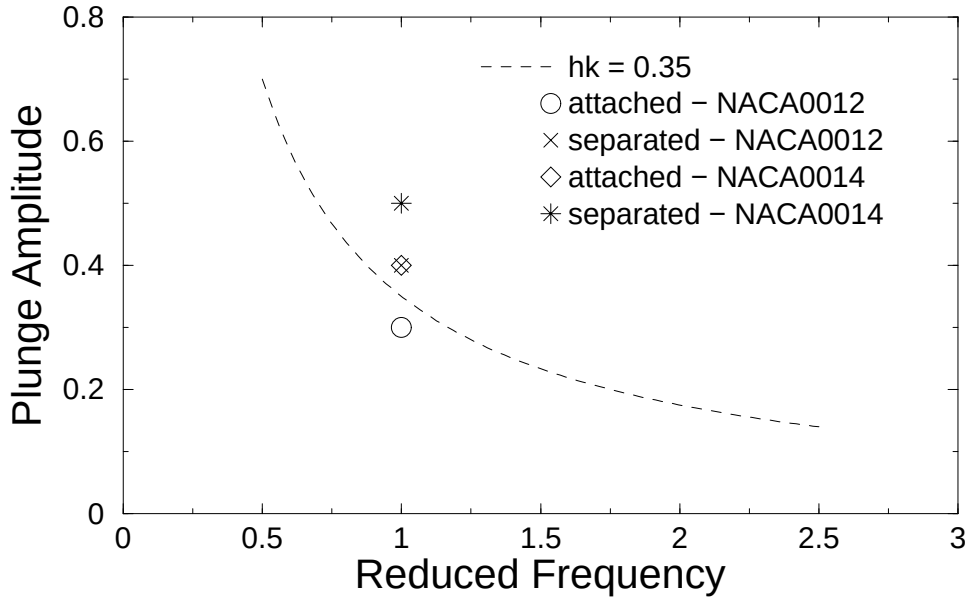

Figure 3.14. Dynamic-Stall Boundary for the NACA 0012 Airfoil

C. GRID MOTION

One of the problems considered in this dissertation is the numerical prediction of the flow around an oscillating airfoil inside a wind tunnel. This problem requires the use of deforming grids; however, problems arise when adjusting the grid, which accounts for the motion of the airfoil. The wind tunnel walls are fixed at all times while the airfoil is moving. Therefore, the grid must be deformed within every time step in order to adjust to the relative movement between the airfoil and the walls.

The required deformation of the grid is obtained by dividing the whole domain of the C-type grid around the airfoil block (1) into four regions. These regions are distributed along the main block as shown in Fig. 3.15. The first region is called A_p and corresponds to the portion of the block that is close to the surface of the airfoil and that is used to capture the viscous flow effects. In this region, the mesh does not deform but simply rotates and translates as a solid body, following the

same rotation and translation of the airfoil. This means that no geometric change of the grid cells in the region A_p occurs. Another region, denoted C, is the one close to the wind tunnel walls and to the blocks (2) and (3) overlapping sections. This region also remains fixed at all times and, therefore, the grid points do not change in time for an observer sitting on the wind tunnel walls.

The region A_w corresponds to the "wake" following region A_p. The A_w is adjusted to the movement of the airfoil. The adjustment is done using an algebraic grid generator that redistributes the grid points. Linear interpolation for the grid points along a constant ζ line is applied. This procedure takes into account that the displacement of a grid point in the region A_w is proportional to the relative displacement of the corresponding points (same ζ coordinate) in regions A_p and C. Finally, while the relative location of regions A_w and A_p with respect to the tunnel walls changes, region B (where the grid deformation is the largest) is adjusted to provide a smooth grid between regions A and C. This adjustment, again, is accomplished by the algebraic grid generator, but now linear interpolation is performed along constant ξ lines.

The same approach is applied for block (1) of the airfoil-in-ground-effect configuration. Blocks (2) and (3) stay fixed throughout the unsteady computations and block (1) must be adjusted to the relative movement between the airfoil and the ground plane. This adjustment is done exactly as described for the wind-tunnel case.

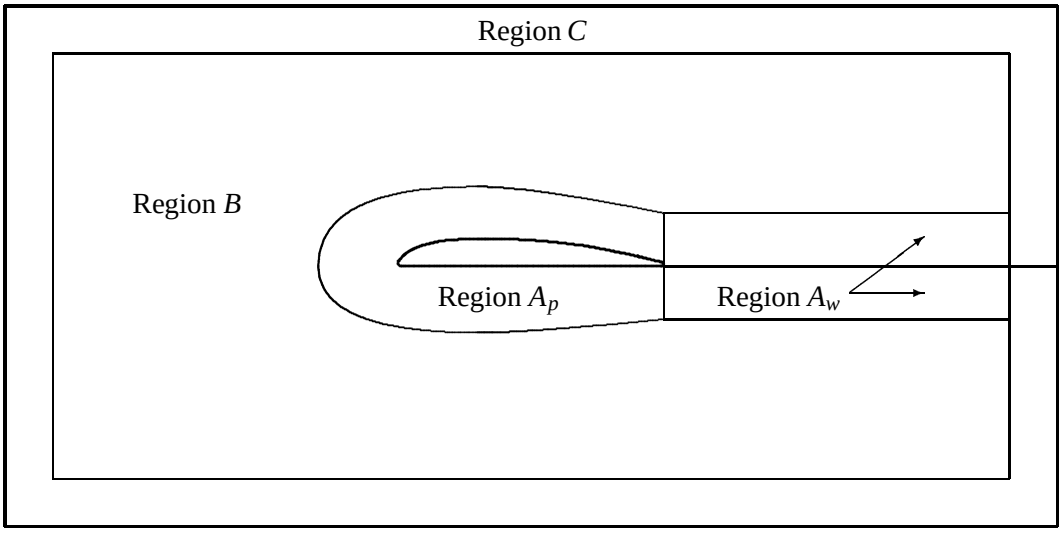

Figure 3.15. Schematic of the Regions for Grid Motion

D. PARALLEL PROCESSING

The strategy of dividing the domain into blocks also has the advantage of allowing the use of parallel processing. Each one of the three blocks is solved in a separate computer and data from the grid points located on the common boundaries are exchanged.

Data related to the boundaries of each block must be transferred to the neighboring blocks to be used as boundary conditions. Data are transferred by a standard library called Message Passing Interface (MPI). The standard library used in the present work is the Local Access Multimachine (MPI/LAM) from the University of Notre Dame.

The parallel version of the Navier-Stokes solver used in the present work is based on the code validated and used by several other researchers (for instance: Ekaterinaris and Menter [16], Ekaterinaris and Platzer [17], Sanz and Platzer [43], and Tuncer and Platzer [51]). Then, subroutines dedicated only for data passing between neighboring blocks were added to the previous version of the code to make it parallel processing capable.

The blocks are defined during the grid-generation phase. They do not need to be of equal dimensions. Actually, because N-S equations are solved in block (1) and Euler equations are solved in blocks (2) and (3), the first block tends to be larger than the other two. This characteristic of the parallel code allows the use of different machines to compose the cluster. For example, block (2) is usually the smallest one. If block (1) is an N-S block with 300x100 points and block (2) is 60x50, the former is 10 times larger than the latter. Therefore, one can use a machine much slower to compute block (2) as the machine used for block (1).

A task performed in the present work was evaluating the ability of the parallel version of the solver to reduce the computational time required for convergence of a particular problem. A simulation for an NLR 7301 airfoil inside a solid-wall wind tunnel was run and a reduction of approximately 10% in the time required to achieve 5,000 iterations was found. Note that the three-block grid used in this case was not favorable for a substantial reduction in the computational time, since the size of the first block corresponded to approximately 85% of the total number of grid cells. Furthermore, thin layer Navier-Stokes equations were solved in it while Euler equations were solved in the other two blocks. Consequently, a 10% reduction in the computational time is quite satisfactory for this particular case and demonstrates the feasibility of the parallel version of the code. The pressure distribution obtained with the parallel code for a steady-state problem is shown in Fig. 3.16. This case is a NLR 7301 airfoil inside a wind tunnel with solid walls. It can be seen that the parallel solution matches the single processor solution well.

An unsteady case was also run in order to check the parallel version of the code. The results of unsteady computations for a porous wind tunnel wall case are shown in Fig. 3.17. The agreement between the parallel and single processor solutions is also very good.

For the parallel version of the code, the three blocks are solved simultaneously, each one in a different node of the PC cluster. The values of the flow variables at the boundaries are always

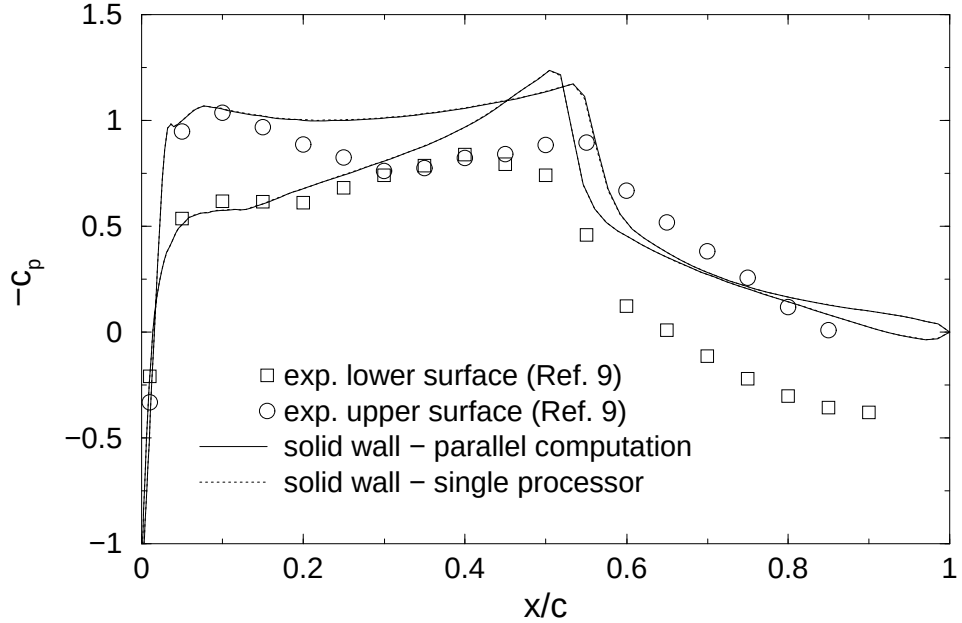

Figure 3.16. Comparison of Surface Pressure Coefficient for Solid Walls

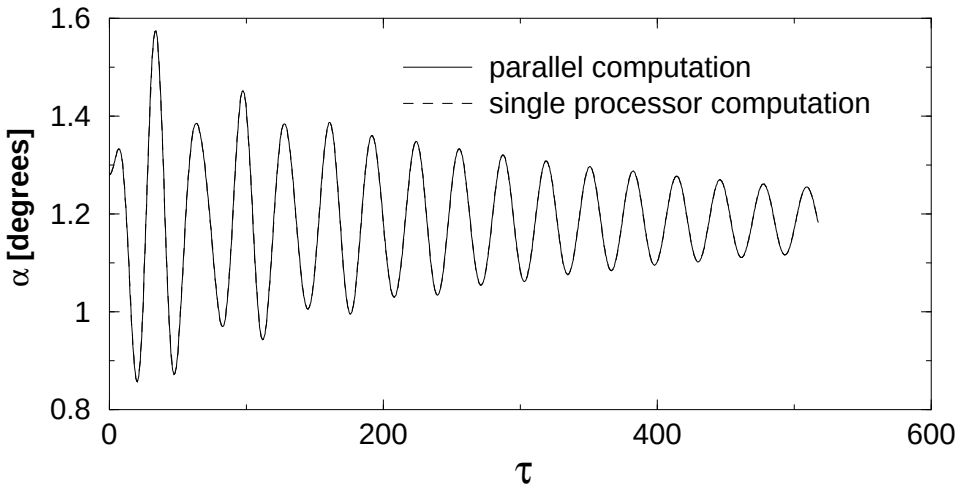

Figure 3.17. Comparison of History of Angle of Attack for Porous Walls

exchanged among the nodes *before* the beginning of each iteration, for all blocks. Therefore, the exchanged boundary conditions are all at the same computational time. On the other hand, for the single processor solution, the blocks are solved sequentially. The boundary conditions for block (2), for example, are transferred from block (1) *after* its solution is advanced one time step. This means that the boundary conditions are not exactly at the same computational time. Despite this subtle difference in the way the two codes work, they yielded virtually the same solution. This shows that, for a reasonably small time step, whether the boundary conditions are exchanged at the exact same computational time or not is not influential.

THIS PAGE INTENTIONALLY LEFT BLANK

IV. VALIDATION OF THE MODELS

A. DEFORMING GRIDS

The problems studied in this work need a solver that can handle deforming grids. The first question that naturally comes to mind is how this methodology handles constant changes in the coordinates of the grid points. In order to answer this question, two tests are designed. They entail a subsonic and a transonic flow, respectively. Both tests show that the present method can perform computations with deforming grids with a negligible deviation of the solution.

The next two subsections explain in detail how these two tests are performed and the results obtained in each test are shown.

1. Subsonic Flow Test

This test is designed to demonstrate the ability of this method to perform unsteady computations with a deforming grid for subsonic flow. The problem is the pure plunge oscillation of a NACA 0014 airfoil. The airfoil is moving with a free-stream Mach number $M_\infty = 0.3$ and a reduced frequency $k = 0.5$. The half amplitude of the plunge motion is $0.4c$.

First, an unsteady inviscid solution is performed using a single grid around the airfoil. This grid moves along with the airfoil as a solid body. Therefore, the grid is moving but not deforming. The grid used for the computations is a C-grid with 281 points in the ξ direction and 51 in the ζ direction. The single-block grid is shown in Fig. 4.1.

Second, another solution is computed using a four-block grid. The main block is a C-grid that contains the airfoil. The second block is an H-grid placed just upstream of the main block. The

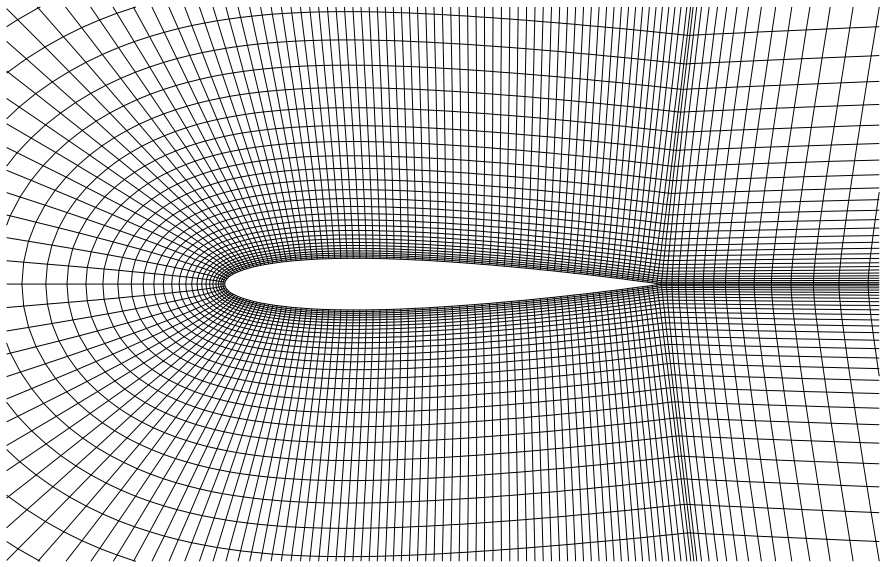

Figure 4.1. Close-Up of the Single-Block Grid around the Airfoil

third block is placed right on top of the first two. The fourth block is a mirror image of the third with respect to the chord plane of the airfoil. This grid is shown in Fig. 4.2. Blocks two, three, and four stay fixed at all times. The only block allowed to deform, in order to accommodate the motion of the airfoil, is the main one. The outer boundary of this block stays fixed in order to exchange boundary conditions with the other blocks.

The comparison of the two solutions is shown in Fig. 4.3. The solution for the single-block grid is represented by the dashed line and the solution for the four-block grid corresponds to the solid line. Despite a very large deformation of the first block in the four-block solution, the agreement with the single-block solution is quite reasonable. The maximum deviations for the lift, drag, and moment coefficients are around 2.1%, 3.5%, and 2.7%, respectively.

The upper and lower boundaries of the first block for the four-block grid were placed at $h = 0.7$ and $h = -0.7$, respectively. The highest and lowest positions for the airfoil correspond to

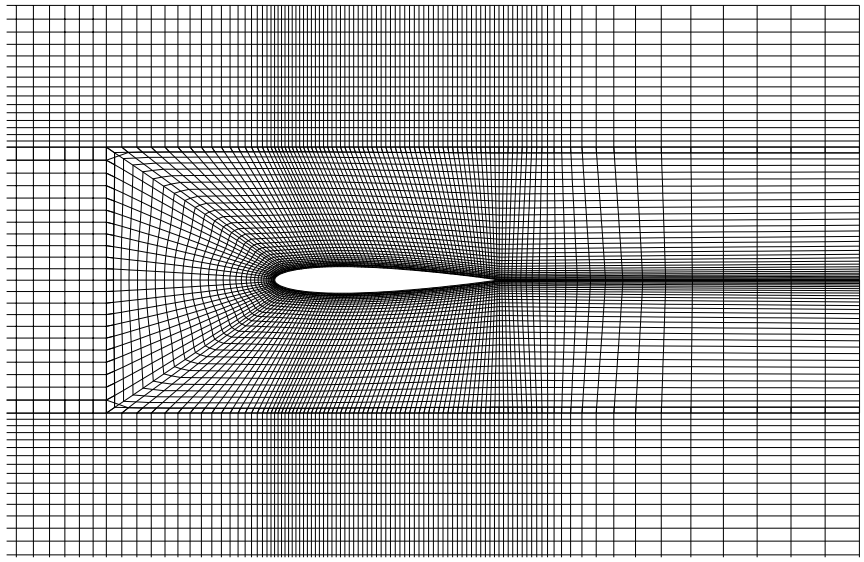

Figure 4.2. Portion of the Four-Block Grid around the Airfoil

$h = 0.4$ and $h = -0.4$, respectively. This means that the deformation of the first block is quite large. To better illustrate this point, the four-block grid with the airfoil in its lowest position ($h = -0.4$) is shown in Fig. 4.4. A steady-state solution for the airfoil at $h = -0.4$ is evaluated and compared to a similar computation for $h = 0$ (undeformed grid) in Fig. 4.5. The solver is not able to predict a symmetric solution for $h = -0.4$, as it is for $h = 0$, due to the large deformation of the grid. This deviation of the steady-state solution for $h = -0.4$ may explain the difference between the single-block and the four-block solutions for the unsteady problem.

Despite the large deformation of the grid, this method was able to keep the difference between the single-block and the four-block solutions lower than 4%. It is important to note that the four-block grid used here is just an extension of the three-block grid used to solve the airfoil-in-ground-effect problem.

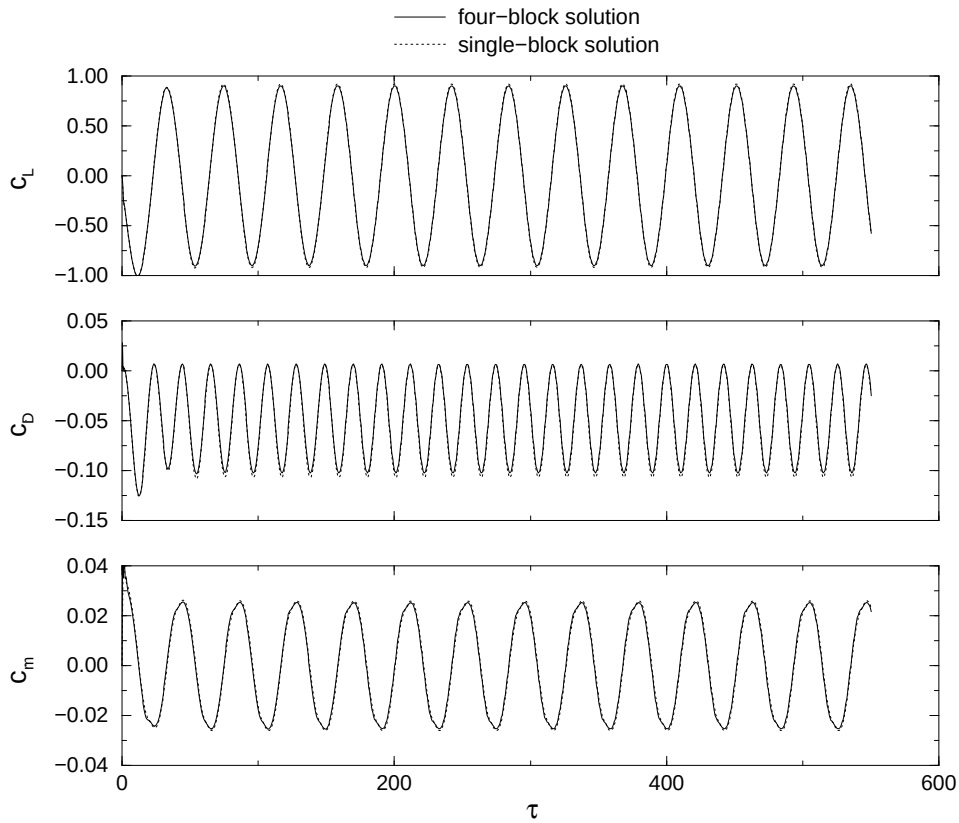

Figure 4.3. Comparison of Euler Solutions for Single- and Four-Block Grids

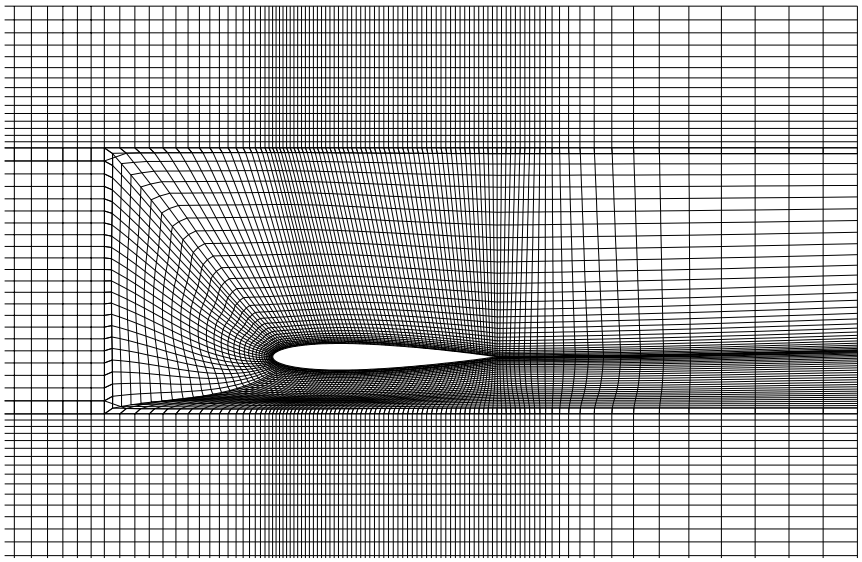

Figure 4.4. Detail of the Four-Block Grid in Its Most Deformed Condition

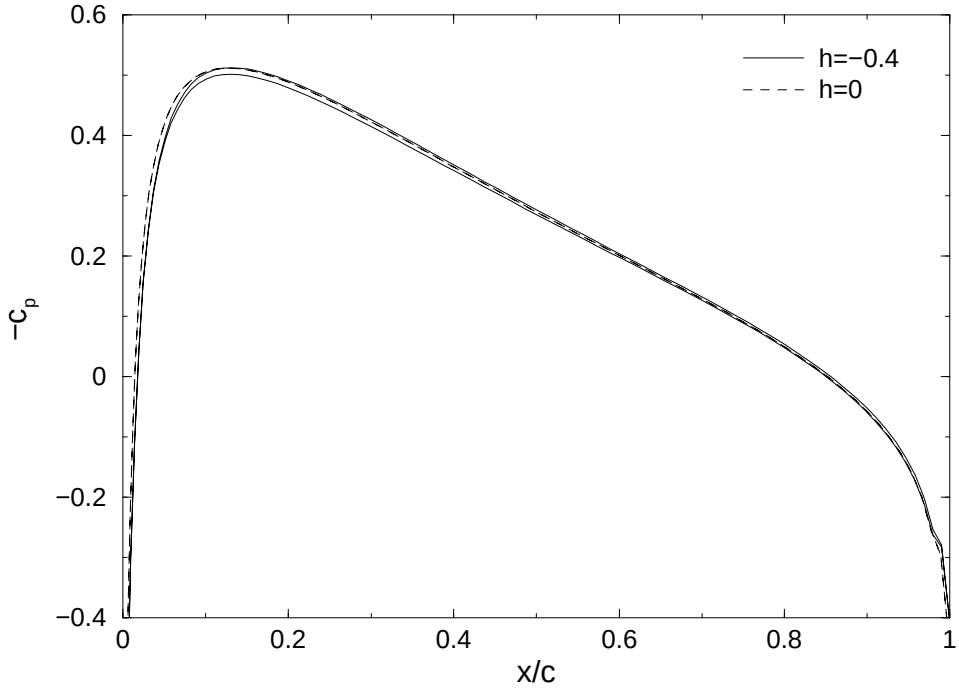

Figure 4.5. Steady-State Pressure Distribution for the Four-Block Grid

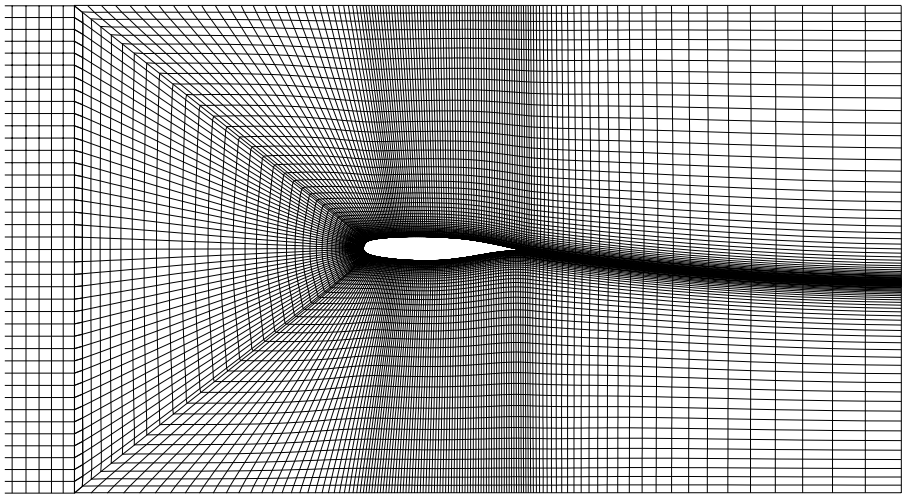

Figure 4.6. Three-Block Grid near the NLR 7301 Airfoil

2. Transonic Flow Test

This test is intended to determine the performance of this method for a transonic flow problem in which only the grid is changing. Two different solutions are computed. One for a fixed grid and another for a deforming grid.

The problem solved is the transonic flow around the NLR 7301 airfoil inside a wind tunnel. The flow is steady at a Mach number of $M = 0.768$, a Reynolds number of $Re = 1.727 \times 10^6$, and an angle of attack of $\alpha = 1.28$ degrees. The walls of the wind tunnel are considered as being completely solid. The grid used is shown in Fig. 4.6. It is a three-block grid and the dimensions of the first, second, and third blocks are 281×81, 41×41, and 41×61, respectively.

To validate the handling of the deforming grid, the test is performed where the boundary of region B in block (1) remains fixed, but the interior points of B perform sinusoidal oscillations. Grid points in blocks (2) and (3) as well as the ones in regions A_p, A_w, and C of block (1) remain

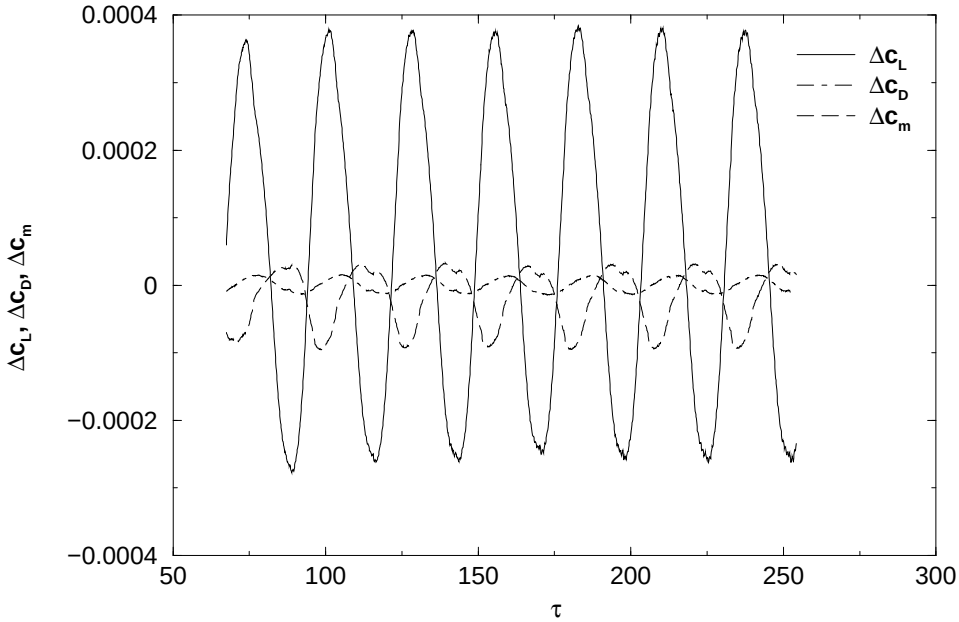

Figure 4.7. Deviation from the Fixed-Grid Solution

fixed. The reduced frequency of the oscillation of grid points in region B is set to $k = 0.3$ and the maximum amplitude to $\Delta h = 0.05$.

This test is initialized from a steady-state solution for a solid wind tunnel wall boundary condition at a non-dimensional time of $\tau = 46.72$. Ideally, the solution should remain constant after the oscillation of the grid points in region B has started. Nonetheless, because of numerical errors and the movement of grid points across a shock wave, some variation of the aerodynamic coefficients should be expected. The results for the test are shown in Fig. 4.7. The amplitudes of the deviation of the aerodynamic coefficients are $\Delta c_L = 3.2 \times 10^{-4}$, $\Delta c_D = 1.6 \times 10^{-5}$, and $\Delta c_m = 6.4 \times 10^{-5}$.

The results of a DFT analysis on the deviations is presented in Fig. 4.8. One can see that the non-dimensional frequency of the signal is computed as $\hat{f} = 0.0375$. This corresponds to a reduced frequency of $k = 0.307$, which is approximately the reduced frequency in which the grid was oscillating. The amplitudes of the oscillations are approximately three orders of magnitude

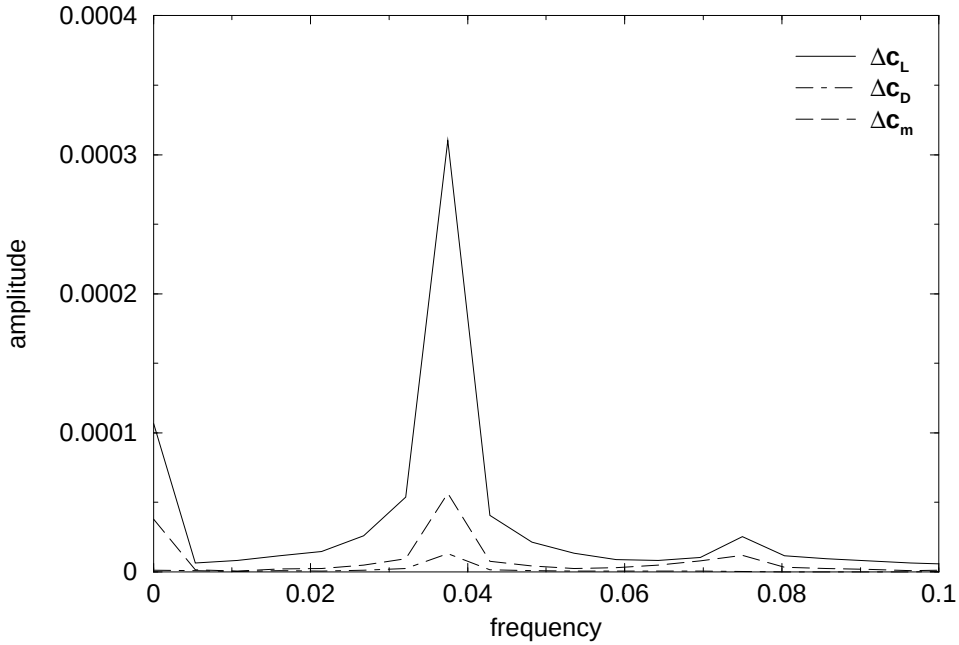

Figure 4.8. DFT Analysis of the Deviation

smaller than the oscillations of the aerodynamic coefficients during the limit-cycle oscillations. These small-amplitude oscillations are considered to be acceptable.

This result for the error between the fixed and deforming grid solution was found to be consistent with the results obtained in similar tests performed in [47]. This means that the present method is capable of handling deforming grids with an acceptable degree of accuracy.

B. PRESCRIBED MOTION ANALYSIS

First in this section, the results of the present solver are compared with computations of Isogai et al. [21] and Tuncer et al. [53] for a single NACA 0012 in a pitch/plunge motion. The parameters of the motion of the airfoil were chosen in such a way that separation occurs and dynamic vortices are developed. The second part of this section contains a comparison with the unsteady potential flow solver USPOT for an NACA 0014 airfoil in ground effect. Euler solutions are computed

and the good agreement with predictions of USPOT shows that the present code can handle moving and deforming grids with a reasonable degree of accuracy. The results also show a significant influence of the free-stream Mach number on the aerodynamic coefficcients computed for the airfoil in ground effect.

1. Single-Airfoil Pitch/Plunge Motion

The results of the present code are compared to the ones obtained by Isogai et al. [21] for a pitch/plunge motion of a NACA 0012 airfoil. The reduced frequency is constant and equal to $k = 1.0$ for all computations. The half amplitudes are $\hat{\alpha} = 10$ degrees and $\hat{h} = 1.0$ for the pitch and plunge motions, respectively. The phase angle between pitch and plunge motions is varied from $\phi = 30$ degrees to $\phi = 150$ degrees. The free-stream Mach and Reynolds numbers are set to $M_\infty = 0.3$ and $Re_\infty = 10^5$, respectively. The fully turbulent flow is computed by using the B-L turbulence model. The grid used is the same presented in Fig. 3.6.

The vorticity contours are presented in Fig. 4.9 for $\phi = 90$ degrees. This case differs only by the free-stream Reynolds number from the one used in Section III.B.3, in which the trailing edge boundary condition is discussed. The results obtained by Isogai et al. [21] are on the LHS and the present results are on the RHS of Fig. 4.9. The agreement between the two solutions is good. The location of the primary vortex is predicted very closely in both solutions. The prediction of a secondary vortex occurs in both cases. Even a small separation near the trailing edge is picked up by both solvers. Note that the contours are not the same for both results. The contour lines of Isogai et al. are not defined in [21], hence, it is difficult to reproduce the same contours.

In their research, Isogai et al. [21] compared their results with Tuncer et al. [53]. They varied the phase angle between pitch and plunge and calculated the thrust coefficient and the propulsive efficiency. Their results for these two parameters are compared to the present code computations in

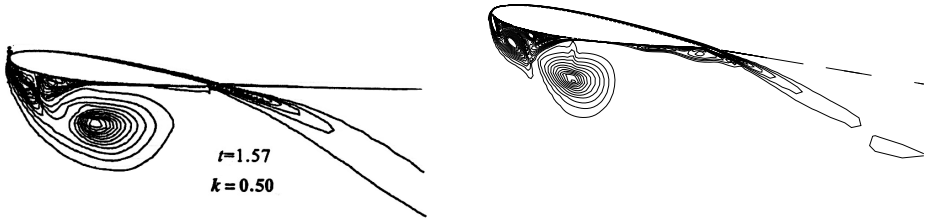

Figure 4.9. Vorticity Contours of Isogai et al. (left) and Present Work (right)

Fig. 4.10. In the present work, the reduced frequency of the motion is equal to $k = 1.0$, the plunge amplitude is $\hat{h} = 1.0$, and the Reynolds numbers are $Re_\infty = 10^5$ and $Re_\infty = 10^6$. Note that, because of a different nondimensionalization, the reduced frequency and the plunge amplitude of [21] are $k = 0.5$ and $\hat{h} = 2$, respectively.

The present results, shown in Fig. 4.10, contain error bars due to the non-periodicity of the computed solution. The thrust coefficient and the propulsive efficiency are not the same for each cycle and the variation of these parameters through ten cycles is represented by the error bars. It is important to note that the maximum induced angle of attack is symmetric with respect to a phase angle equal to $\phi = 90$ degrees. For instance, the maximum induced angle of attack for $\phi = 30$ degrees is the same as for $\phi = 150$ degrees. The present results show a similar behavior for the thrust coefficient and propulsive efficiency. The curve through the mean values of these paramaters is almost symmetric with respect to $\phi = 90$ degrees, although the variation around the mean value is not symmetric.

An attempt to compare results with Ramamurti and Sandberg [40] was made but, because of the large values of amplitudes of the motion and reduced frequency, the present code was unable to compute a meaningful solution. The value of the Strouhal number used in their computation is

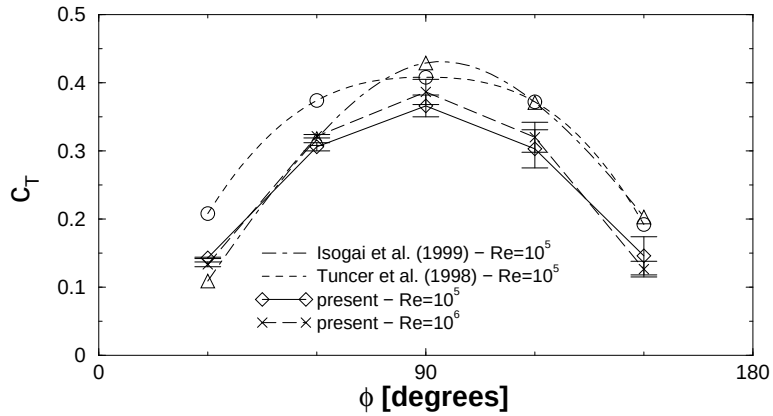

(a) Thrust Coefficient

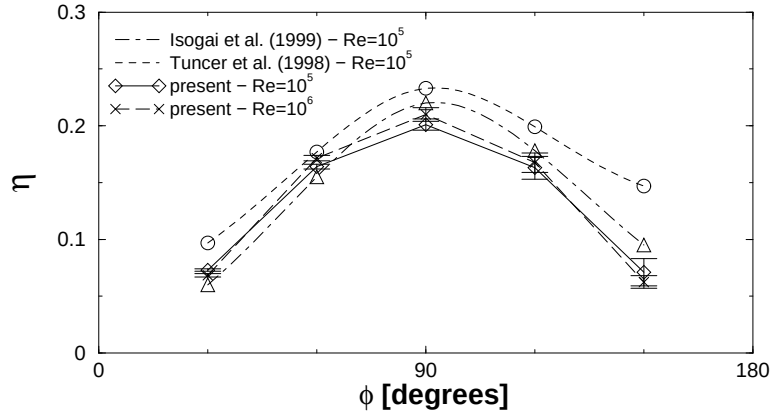

(b) Propulsive Efficiency

Figure 4.10. Thrust Coefficient and Propulsive Efficiency for the NACA 0012 Airfoil

around $Sr = 0.6$, which corresponds to a reduced frequency $k = 3.8$. The amplitudes of the motion are $\hat{\alpha} = 15$ degrees and $\hat{h} = 1.0$. With this combination of parameters, the present code predicts locally supersonic flow even for a free-stream Mach number of $M_\infty = 0.1$. Because Ramamurti and Sandberg [40] used an incompressible Navier-Stokes solver for their computations, no comparison with their results could be done.

2. Airfoil-in-Ground-Effect and Pure-Plunge Motion

A final validation of the present code is performed for a biplane configuration. This computation shows that the equations for deforming grids can compute the flow over an oscillating airfoil in ground effect accurately.

Euler solutions for a pure plunging NACA 0014 biplane are compared with the one obtained by using an unsteady potential flow solver called USPOT [37]. The reduced frequency of the oscillation is $k = 0.5$. The half amplitude of the motion is $\hat{h} = 0.4$. The separation between the wings is $l = 1.4$. For the present solution, only one wing is modeled and the presence of the second wing is simulated by a symmetry plane. The distance from the wing to the symmetry plane is, then, $d = 0.7$.

The Euler solutions were run for Mach numbers of $M_\infty = 0.2$ and $M_\infty = 0.3$. The multi-block grid used is shown in Fig. 4.11. The dimensions for blocks (1), (2), and (3) are 289×41, 41×39, and 165×51, respectively. The solutions for the two Mach numbers are presented in Fig. 4.12 and compared with the USPOT solution. The incompressible flow solution computed by USPOT corresponds to a Mach number of $M_\infty = 0$. The Euler solutions for $M_\infty = 0.2$ and $M_\infty = 0.3$ show a maximum lift coefficient higher than the one predicted by USPOT. Nonetheless, clearly, the tendency is to approach the incompressible solution as the Mach number diminishes. The same

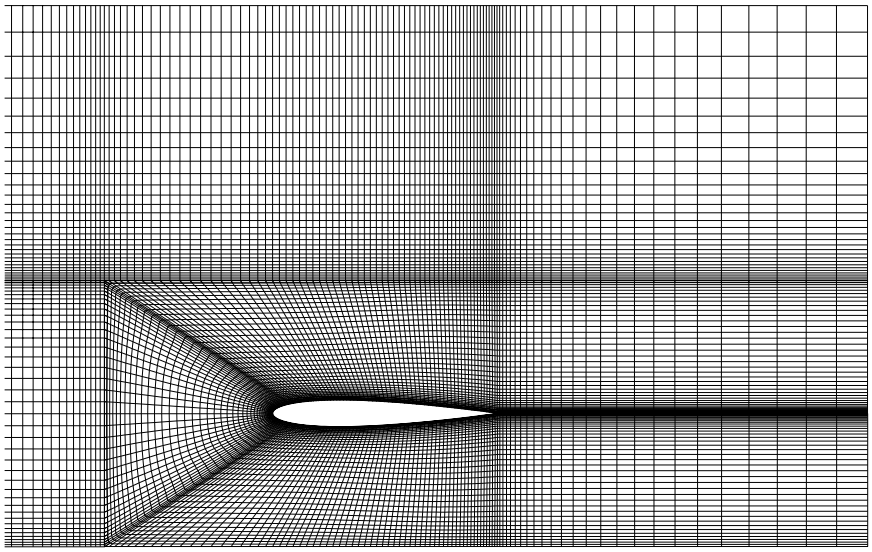

Figure 4.11. Euler Multi-Block Grid near the Airfoil

behavior is observed with respect to the drag coefficient. The minimum values for the Euler drag coefficients tend to move toward the USPOT solution as the Mach number decreases.

The influence of the Mach number on the aerodynamic coefficients is known to be quite significant for wings in extreme ground effect, as discussed by Rozhdestvensky [41]. For wings in extreme ground effect, meaning distances from the ground lower than 10% of the chord, the aerodynamic coeffients vary with the parameter $(1-M_\infty)^{-1}$ and not $(1-M_\infty)^{-1/2}$. Even though the smallest distance from the airfoil to the ground during the oscillation is $d = 0.3$, the influence of the Mach number is still significant.

This computation shows that the solution obtained with the compressible, deforming-grid code is in good agreement with the solution calculated for the unsteady potential flow. Therefore, the present solver shows that it can perform accurately for a deforming grid situation. Furthermore,

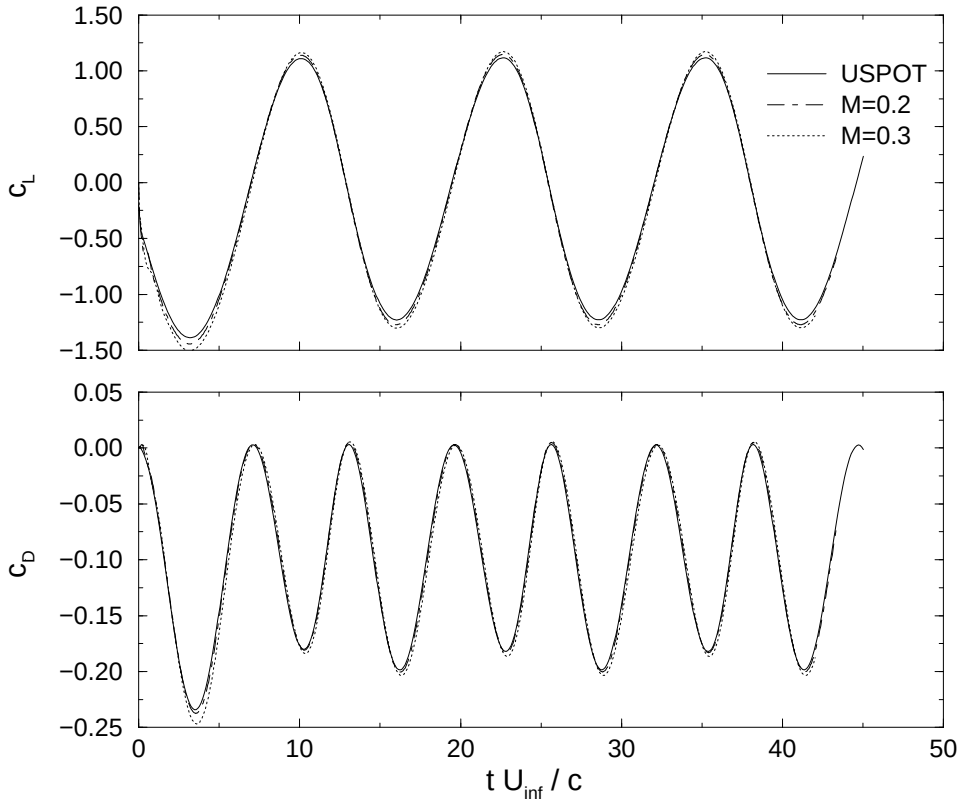

Figure 4.12. Comparison of Euler and Potential Flow Solutions for a Biplane Configuration

the solution shows a significant influence of the Mach number on the unsteady flow characteristics of the biplane or airfoil-in-ground-effect configuration.

V. RESULTS

A. FLAPPING AIRFOIL PROPULSION

The biplane model studied at the Naval Postgraduate School is presented in Fig. 5.1. It has two sets of wings with a chord of $\tilde{c} = 0.064m$. The wings oscillate sinusoidally in an opposed plunge manner. The mean separation between the two planes is $\tilde{l} = 0.0896m$, which yields a non-dimensional value of $l = \tilde{l}/\tilde{c} = 1.4$. This configuration, as explained in Chapter III, can be modeled by only one airfoil oscillating above a symmetry plane, similar to a wing in ground effect. The non-dimensional mean distance from the airfoil section to the symmetry plane is, then, $d = 0.7$. The amplitude of the motion of the airfoil corresponds to a non-dimensional value of $\hat{h} = 0.4$. This enables a minimum clearance of $d - \hat{h} = 0.3$ from the symmetry plane.

This configuration was tested by Lund [34] and the experiments were conducted inside a low-speed, open-section wind tunnel with speeds varying from $U_\infty = 0$ to $U_\infty = 9.5m/s$. The Reynolds number varied from $Re_\infty = 0$ to $Re_\infty = 45,000$ and the Mach number from $M_\infty = 0$ to $M_\infty = 0.028$. The frequency of the oscillation of the wings was set to discrete values of $f = 3, 5,$ and 7 Hz.

The numerical computations were performed in a three-block grid in which block (1) corresponds to a 289×81 C-grid, block (2) is a 61×29 H-grid, and block (3) is represented by a 152×51 H-grid. A close-up of the grid around the airfoil is presented in Fig. 5.2. The S-A and B-L turbulence models were used to perform fully turbulent calculations. Fully laminar computations were also performed because of the low Reynolds number of the experiments. In this case, no turbulence model was used.

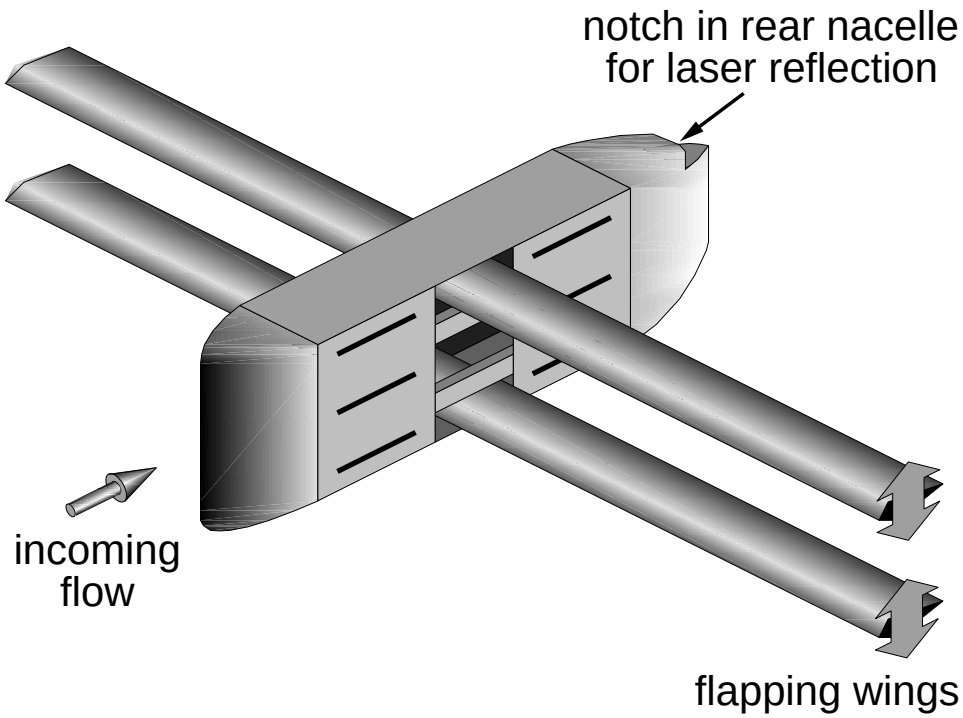

Figure 5.1. Schematic of the Test Model for the Biplane Configuration

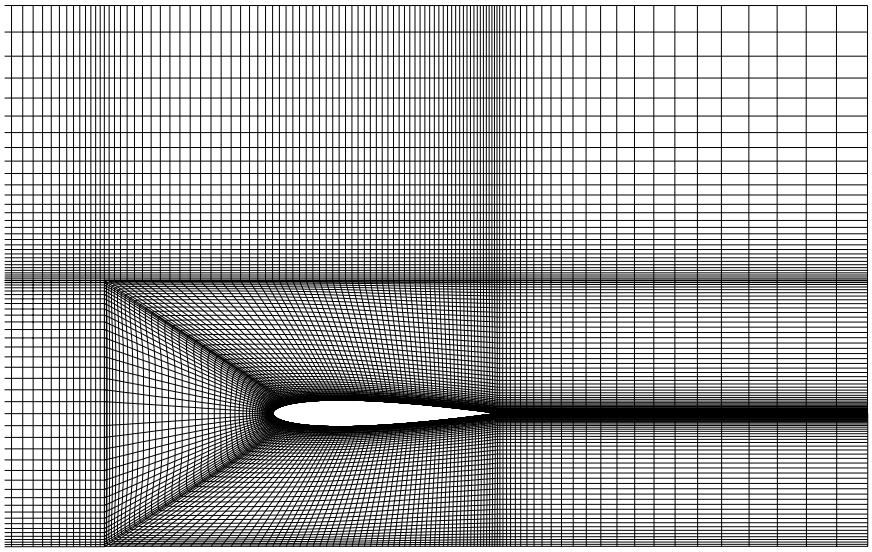

Figure 5.2. Three-Block Grid near the Airfoil Section

No sensitivity analysis to the size of the grid was performed in the present work because of the results obtained by Tuncer et al. [53]. They found that the computed solution was not sensitive to grid sizes of 121×62, 241×61, 241×91, and 311×71. However, a sensitivity study to the time step was performed for some of the unsteady cases of the present work. This study was accomplished by increasing the number of Newton sub-iterations within each physical time step, which was found to be equivalent to reducing the time step. The results of this procedure showed that the parameters computed by means of averaging through a cycle did not change significantly. The prediction of fine detail of the flow-field, such as the frequency of leading edge vortex shedding and the location of the dynamic vortex along the cycle, was more sensitive to the time step. Nevertheless, because the main interest of the present work is on averaged values along the cycle, such as the thrust coefficient and the propulsive efficiency, three Newton sub-iterations were used and the time step was kept within a minimum of $3,500$ steps per cycle.

1. Steady-State Computations

Steady-state solutions are needed to start up unsteady solutions. Another reason for computing them is the need to correct the calculation of the thrust coefficient. In the experiments, one is interested in measuring the thrust due to the oscillation of the wings. This is done by measuring the drag, or thrust, for the entire model, including the wings and fuselage, and subtracting the steady-state drag measured for the same model. The difference is the thrust due to the flapping of the wings.

The consequence of this procedure is that all types of steady-state drag are eliminated, including friction and pressure drag of the wing. Hence, in order to compare numerical and experimental results, the same procedure must be performed. The computed steady-state drag also has to be subtracted from the unsteady values.

Table 5.1. Steady-State Drag Coefficients

h	laminar $M = 0.1$	S-A $M = 0.1$	S-A $M = 0.3$	B-L $M = 0.1$
-0.4	0.0260	0.0038	0.0038	0.0050
-0.2	0.0228	0.0030	0.0030	0.0031
0.0	0.0217	0.0028	0.0028	0.0029
0.2	0.0212	0.0027	0.0027	0.0028
0.4	0.0209	0.0026	0.0026	0.0027

For the biplane configuration, or wing in ground effect, it is known that the drag coefficient is a function of the ground clearance. Consequently, a series of steady-state computations were performed for various values of distances from the ground. The results for these calculations is presented in Table 5.1.

The steady-state solutions for fully turbulent flows were run for a Reynolds number $Re_\infty = 10^6$. This value is much higher than the Reynolds number of the experiment but, in order to use B-L or S-A turbulence models, 10^6 is the minimum value of their range of application. The pressure distributions for these turbulence models are shown in Fig. 5.3 for a distance from the symmetry plane equals to $d = 0.3$, corresponding to the closest position during the sinusoidal motion of the airfoil. The two solutions are very close to each other, showing that, for steady-state computations, the turbulence models do not have a strong influence on the calculations. Furthermore, the pressure distribution is not symmetric anymore. The lift force resulting from the imbalance of pressure is now in the direction of the ground plane.

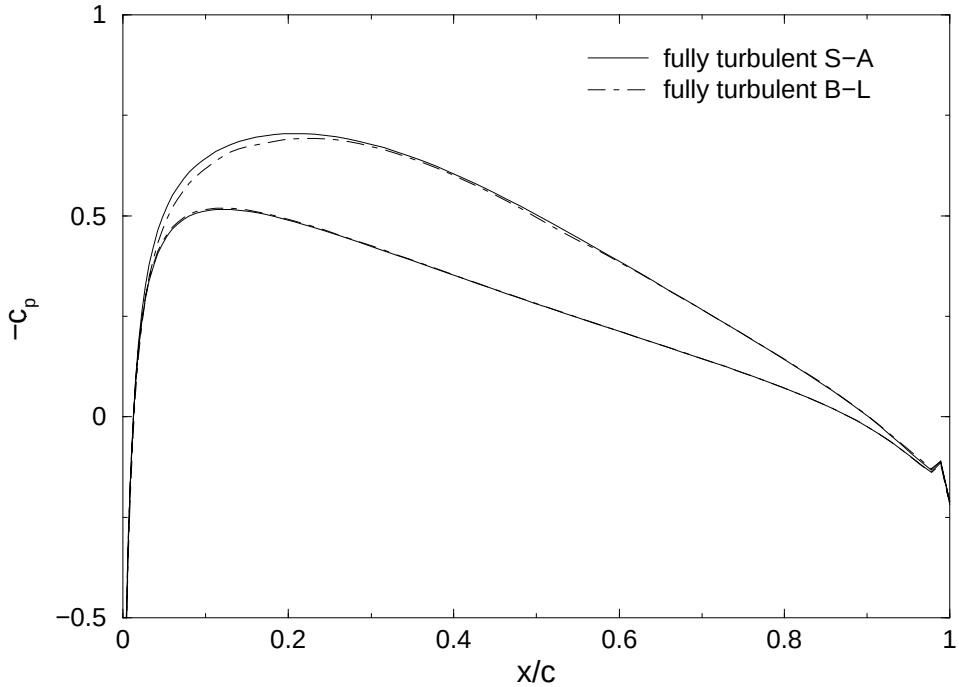

Figure 5.3. Pressure Coefficient Distributions for B-L and S-A Models

The solution for fully laminar flow was performed using $Re_\infty = 10^4$. The pressure distribution over the airfoil for this case is presented in Fig. 5.4. Also shown in this figure is the pressure distribution for the fully turbulent flow using the S-A turbulence model. The two solutions look quite different. The flow for the laminar solution is separated whereas the fully turbulent flow is always attached to the airfoil. A snapshot of the vorticity field for the laminar computation is presented in Fig. 5.5. The boundary layer is quite thick and detaches from the surface of the airfoil, producing vortices that are shed from the trailing edge. This means that even the fixed-airfoil solution has an unsteady behavior for the low Reynolds number in question. This unsteady behavior can also be seen in the history of aerodynamic coefficients shown in Fig. 5.6.

The vortices produced by the detachment of the boundary layer are drag inducing vortices. Their orientation is such that they tend to approach the ground plane. Therefore, the wake is deflected downward and induces a positive (upward) lift on the airfoil.

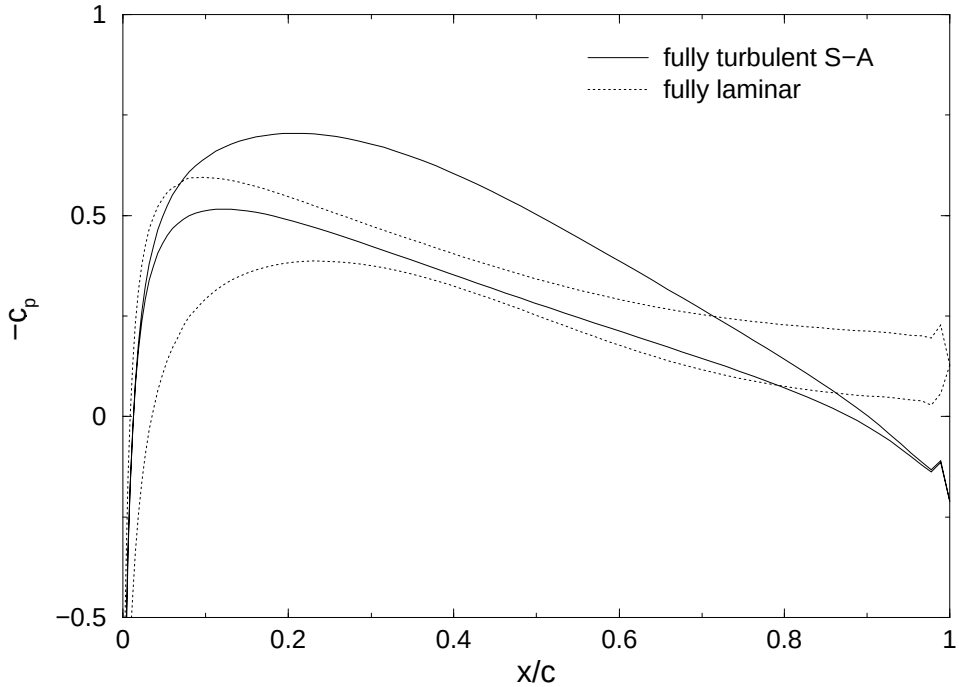

Figure 5.4. Pressure Coefficient Distributions for Laminar and Turbulent Flows

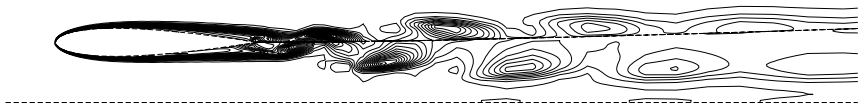

Figure 5.5. Entropy Contour Lines for the Laminar Solution

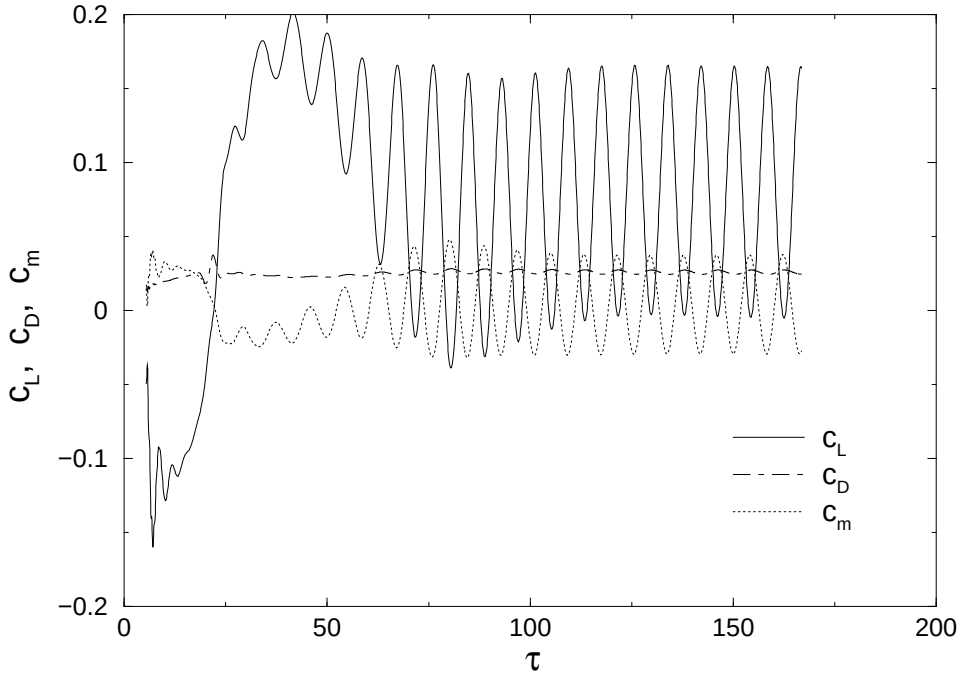

Figure 5.6. History of Aerodynamic Coefficients for the Laminar Flow Solution

The steady-state solutions show that the fully turbulent flow is not influenced significantly by the use of the B-L or the S-A turbulence model. The flow is always attached to the airfoil and the lift force is negative (pointing to the ground plane). On the other hand, the laminar-flow solution yields a relatively thick boundary layer, which detaches from the airfoil and produces an oscillatory behavior for the aerodynamic coefficients.

2. Oscillating Airfoil Computations

In the experiments, the frequency of oscillation of the wings was set to a fixed value, and the speed of the wind tunnel was changed in order to vary the reduced frequency. This means that the free-stream Reynolds number is different for each value of reduced frequency. The range of the free-stream Reynolds number in the experiments was from $Re_\infty = 0$ to $Re_\infty = 45,000$. In the numerical solutions, the Reynolds number was kept fixed for all values of reduced frequency

because of the large number of steady-state solutions that would have to be generated to start up the unsteady computations. The Reynolds number was set equal to $Re_\infty = 10^4$ for the laminar solutions and $Re_\infty = 10^6$ for the fully turbulent computations. It is important to mention that this procedure may induce discrepancies when comparing experimental and numerical data.

The free-stream Mach number is another important issue. Ideally, because of the limitations of the numerical scheme, the minimum free-stream Mach number should be around $M_\infty = 0.3$. However, for this Mach number and values of reduced frequency around $k = 2.0$, the local Mach numbers of the flow-field reach values as high as $M = 1.5$, at which point compressibility effects are severe. The Mach contour lines for these conditions are shown in Fig. 5.7 with the airfoil in a position very close to $h = 0$ during the up stroke. The contour lines go from $M = 0$ to $M = 1.6$ with an increment of $\Delta M = 0.04$. The region where the local flow is supersonic is presented in Fig. 5.8(a). Although this region is not very large, the region where compressibility effects are already significant is much larger. The entropy contour lines are shown in Fig. 5.8(b). It can be seen that the supersonic pocket occurs inside the dynamic vortex which is being generated at the leading edge. Hence, the physics of the dynamic stall are completely altered by compressibility effects. It is also important to mention that the TVD scheme is switched off for the airfoil in ground-effect computations.

A computation for a free-stream Mach of $M_\infty = 0.1$ was performed for the same reduced frequency of $k = 2.0$. The Mach contour lines are presented in Fig. 5.9 with the same increment of $\Delta M = 0.04$. The local Mach number for this case stays below $M = 0.55$ for the whole cycle. Therefore, most of the computations were performed for a free-stream Mach number of $M_\infty = 0.1$. The idea was to eliminate any source of compressibility effects since the Mach numbers of the experiments were much lower.

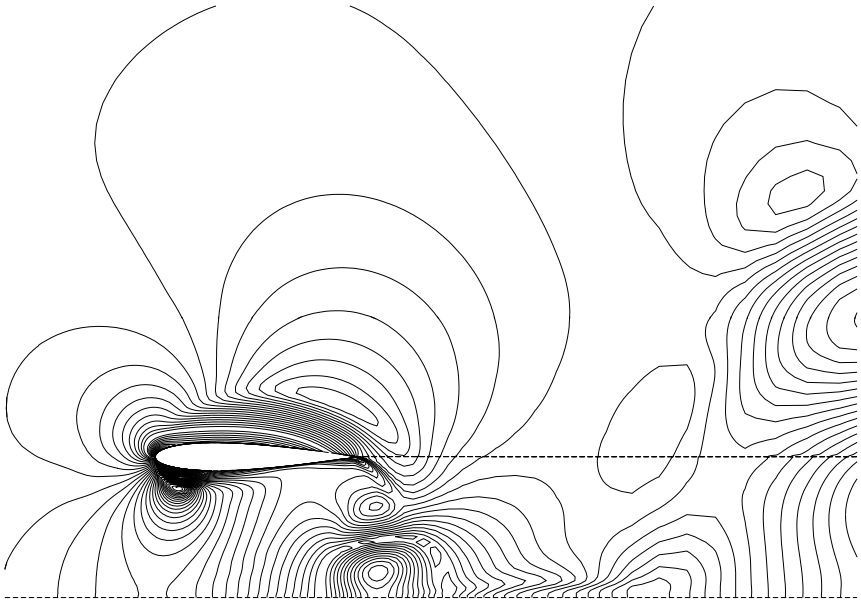

Figure 5.7. Mach Contour Lines for $M_\infty = 0.3$ and $k = 2.0$

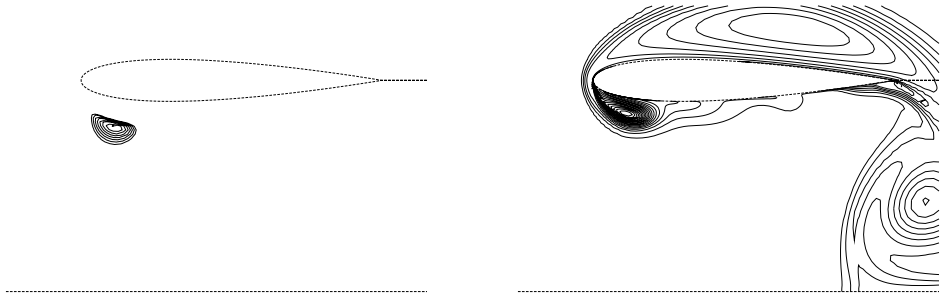

(a) (b)

Figure 5.8. Supersonic Pocket and Entropy Contours for $M_\infty = 0.3$ and $k = 2.0$

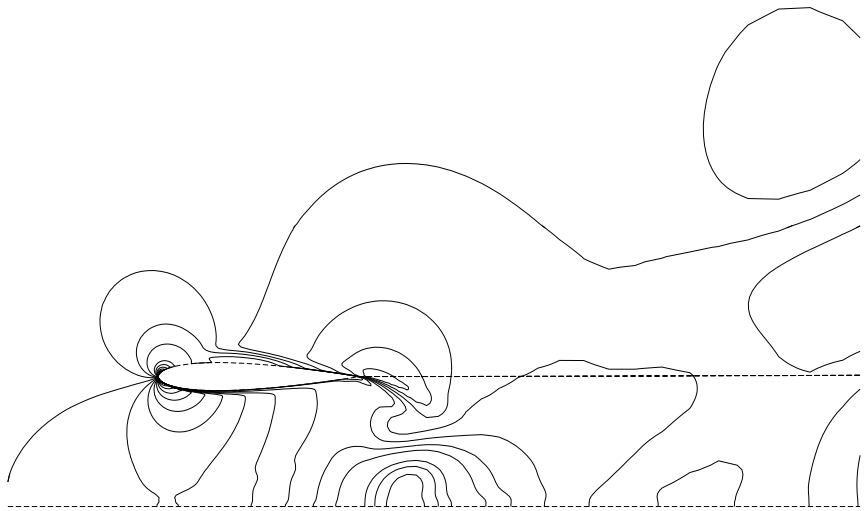

Figure 5.9. Mach Contour Lines for $M_\infty = 0.1$ and $k = 2.0$

The computed thrust coefficient for the airfoil in ground effect configuration and $M_\infty = 0.1$ is presented in Fig. 5.10 as a function of the reduced frequency. The turbulence models used for the fully turbulent solutions were B-L and S-A. The Reynolds number for these cases was $Re_\infty = 10^6$. For the fully laminar solution, the Reynolds number was $Re_\infty = 10^4$. The potential flow solutions for a biplane (USPOT) and a single airfoil (UPOT) configurations and the experimental values obtained by Lund [34] in the NPS wind tunnel are also shown in the same figure.

The thrust coefficient per airfoil is defined by Eq. (5.1):

$$c_T = \frac{T}{1/2\rho_\infty U_\infty^2 c} \tag{5.1}$$

where $T = -D$ is the thrust force generated by the flapping motion of the airfoil, ρ_∞ is the free-stream density and U_∞ is the free-stream velocity of the flow.

Computations for $M_\infty = 0.3$ were also performed for the S-A turbulence model. They are compared with the solutions for the same model and $M_\infty = 0.1$ in Fig. 5.11. For $M_\infty = 0.3$ and values

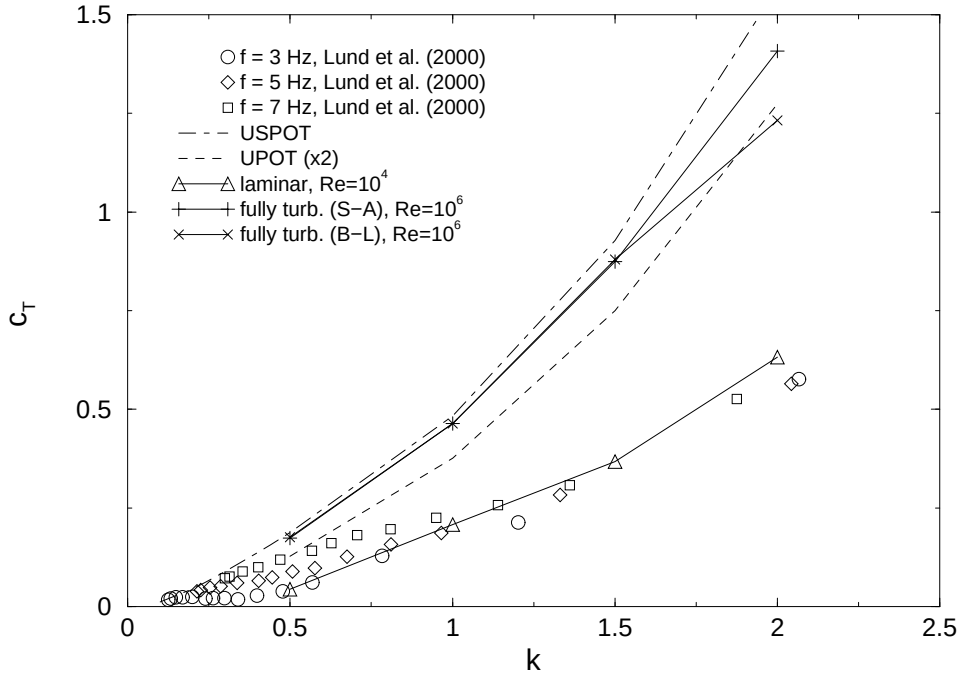

Figure 5.10. Thrust Coefficient for $M_\infty = 0.1$

of reduced frequency higher than $k = 1.0$, compressibility effects clearly change the behavior of the solution dramatically.

The agreement with the experiments of [34] is much better for the laminar than for the fully turbulent solutions, regardless of the turbulence model used for turbulent flow. This is expected because the Reynolds numbers of the experiments are much closer to the Reynolds number of the laminar solution than to the Reynolds number of the fully turbulent computations. At this range of Reynolds numbers, the vortices, which are shed due to the detachment of the boundary layer, dominate the flow over the airfoil, especially for low frequencies. In fact, solutions for S-A and B-L turbulence models, when no vortices are shed, agree better with the USPOT solution. This means that the prediction of the vortices produced by boundary layer detachment or the prediction of the dynamic stall is crucial for simulating correctly the behavior of the flow at this range of Reynolds numbers.

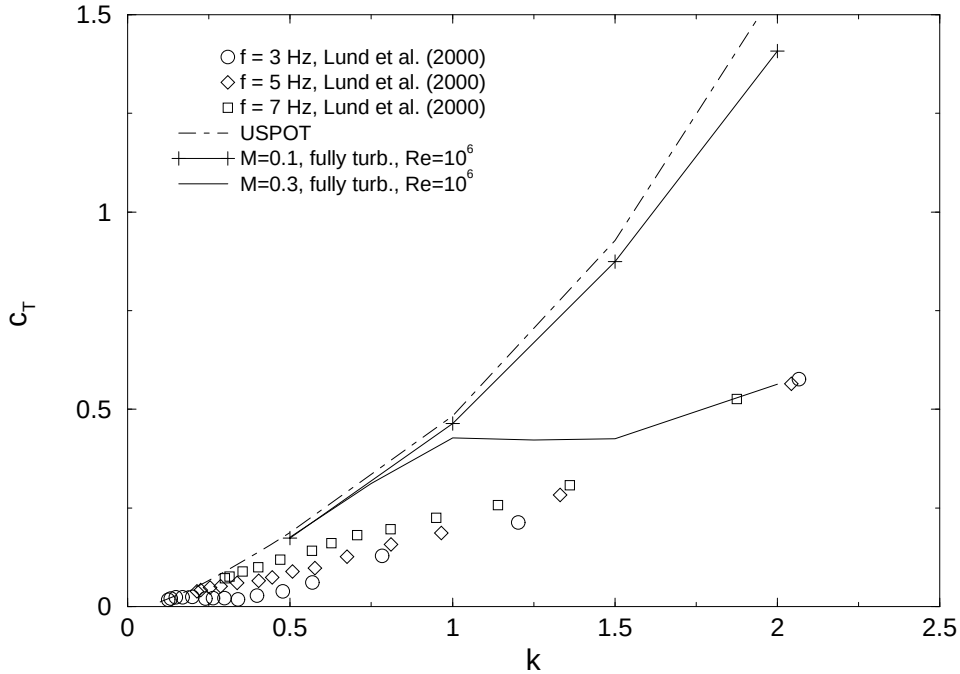

Figure 5.11. Thrust Coefficient for the S-A Turbulence Model

The entropy distribution of the laminar flow field around the airfoil is presented in Fig. 5.12 through a series of frames for different positions along the cycle. The LHS of Fig. 5.12 represents the down stroke whereas the RHS shows the up stroke. The dynamic stall vortices generated during the motion are well captured by the solver, and it is clear that the boundary layer is quite thick for some positions along the cycle. Therefore, reviewing the thin layer assumption of the present solver is essential. This assumption may not hold for positions along the cycle if the boundary layer is relatively thick.

The solutions for turbulent flow are close to the potential flow computations (USPOT) for reduced frequencies up to $k = 1.0$ (S-A and $M_\infty = 0.3$) and $k = 2.0$ (S-A, B-L, and $M_\infty = 0.1$). As stated by Tuncer et al. [53], the limit for separated flows for a single NACA 0012 airfoil is given by the equation $\hat{h}k = 0.35$. According to the discussion presented in Section III.B.3, this limit could be further extended to $\hat{h}k = 0.45$ for the NACA 0014 airfoil. For $\hat{h} = 0.4$, the value of the

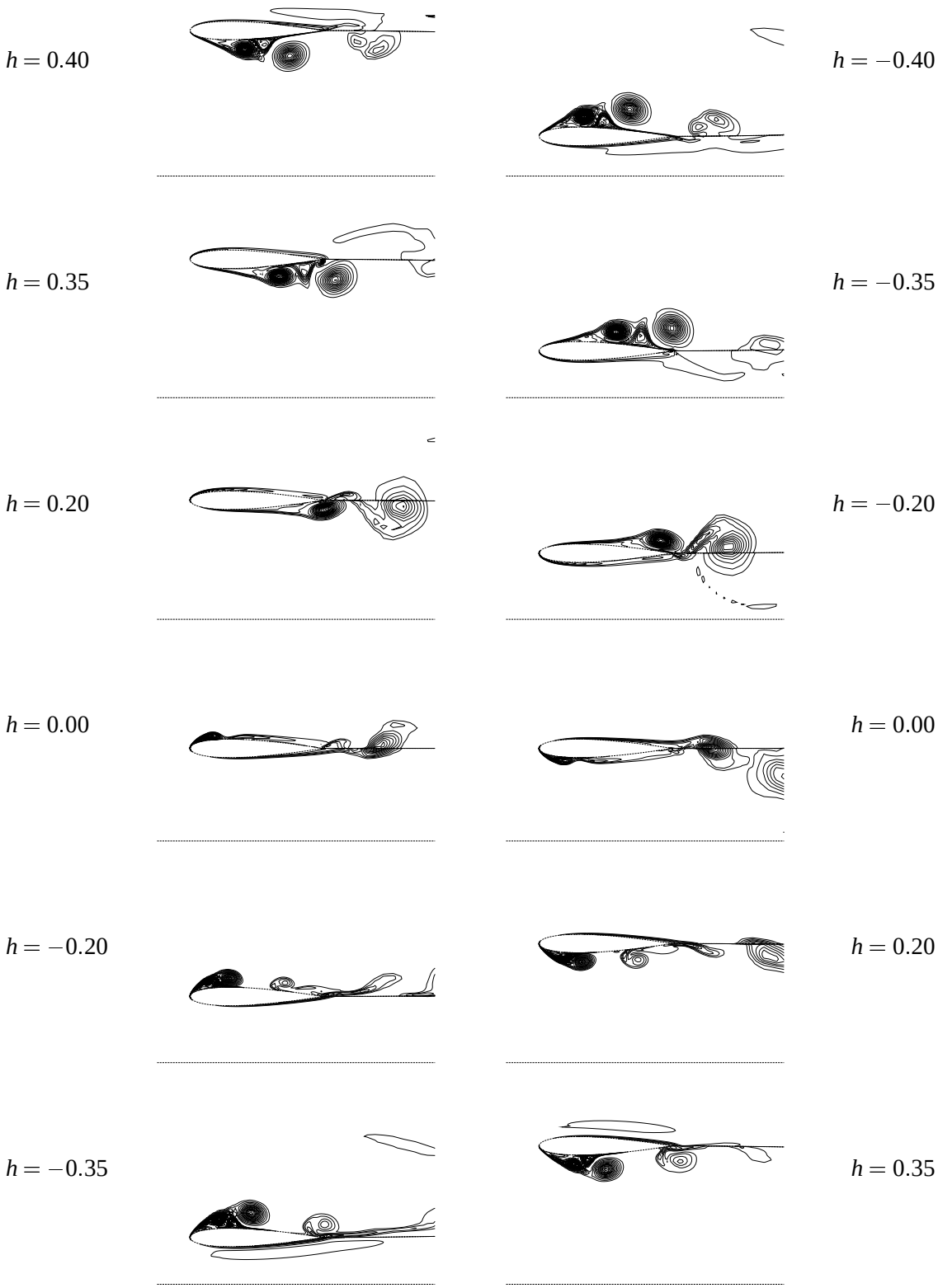

Figure 5.12. Entropy Contour Lines for Laminar Flow, $M_\infty = 0.1$, and $k = 1.0$

reduced frequency for flow separation becomes $k = 1.125$. However, the computed thrust coefficient remains close to the potential flow solution even beyond this dynamic stall limit. In order to assess this behavior, two sequences of entropy contours for $k = 2.0$ and $M_\infty = 0.1$ are given in Figs. 5.13 and 5.14 for the S-A and B-L turbulence models, respectively. For the S-A solution, Fig 5.13, the flow is not completely separated. A recirculation bubble, which convects downstream but only separates from the surface of the airfoil near the trailing edge, is predicted. Furthermore, the bubble predicted for the upper surface is larger than the bubble computed for the lower surface. For the B-L simulation, Fig. 5.14, the dynamic stall vortex is clearly predicted by the solver for both upper and lower surfaces. These solutions suggest that the turbulence model influences the prediction of dynamic stall, and also suggest that the dynamic stall limit for the biplane configuration may be slightly different from the single-wing value.

The propulsive efficiency is defined as the power generated by the thrust force divided by the power necessary to oscillate the airfoil, and it is represented in Eq. (5.2). The computed propulsive efficiency is shown in Fig. 5.15.

$$\eta = \frac{TU_\infty}{P_{req}} \tag{5.2}$$

where $T = -D$ is the thrust force and P_{req} is the power required for oscillating the airfoil.

It is known that the biplane configuration produces more thrust per wing than the single wing. A comparison between computed values of propulsive efficiency and thrust per wing for the biplane and single configurations is shown in Fig. 5.16. It can be seen that the airfoil in ground effect produces more thrust per wing, with almost the same efficiency, than the single airfoil. This behavior was demonstrated previously by Jones et al. [24].

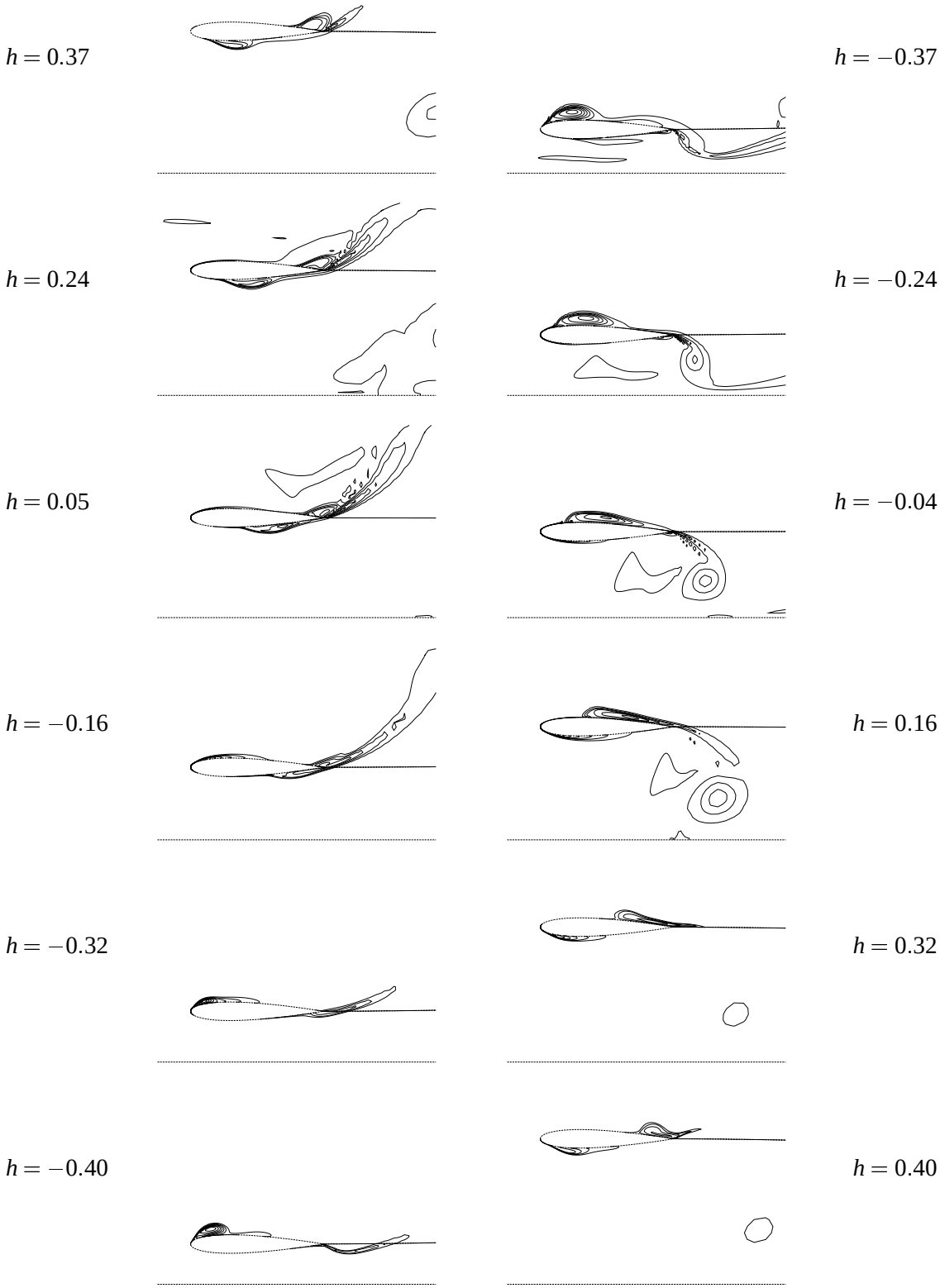

Figure 5.13. Entropy Contour Lines for S-A Turb. Model, $M_\infty = 0.1$, and $k = 2.0$

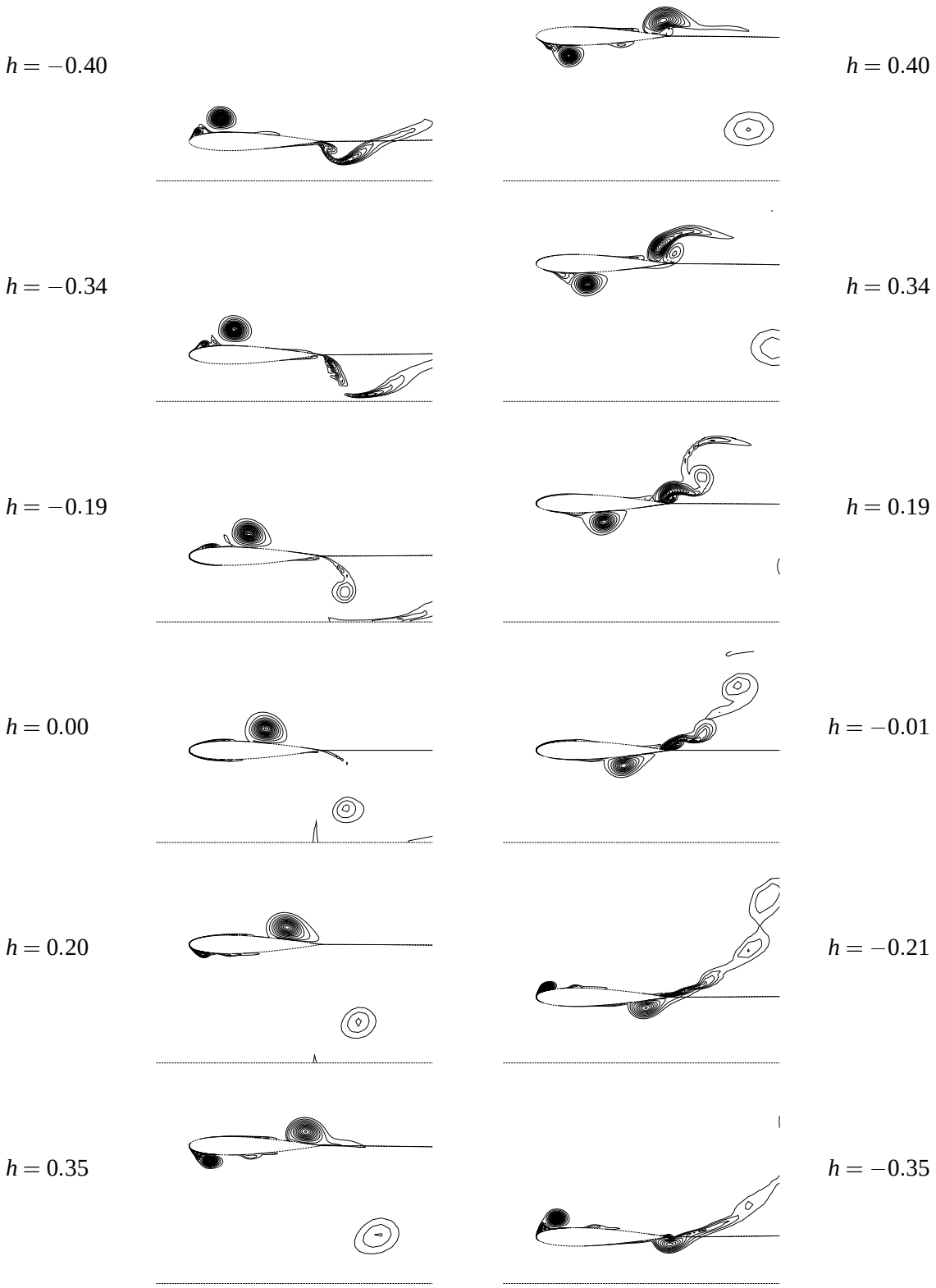

Figure 5.14. Entropy Contour Lines for B-L Turb. Model, $M_\infty = 0.1$, and $k = 2.0$

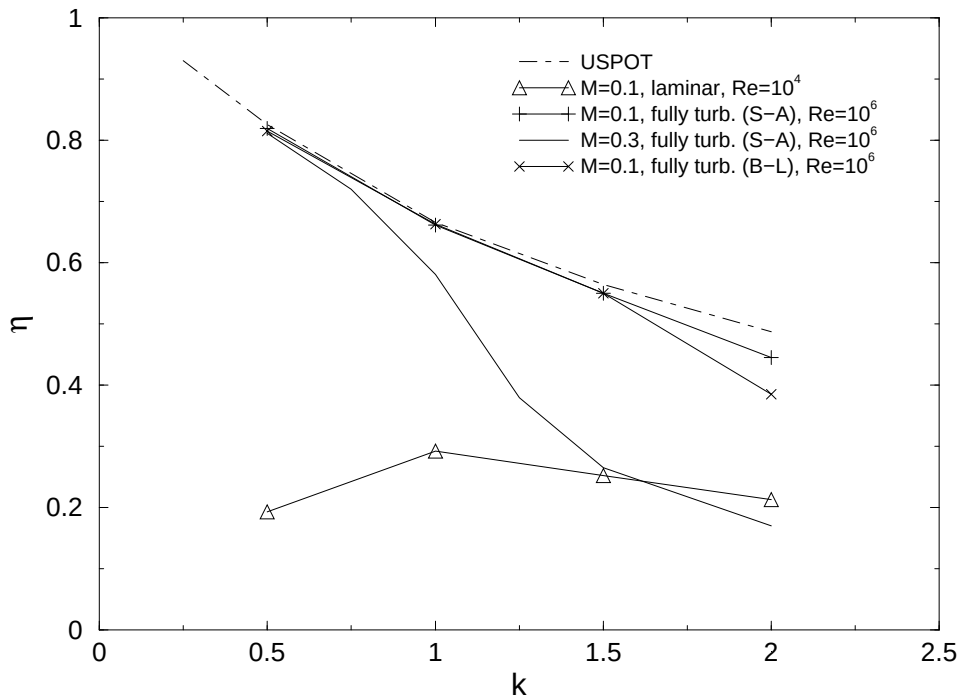

Figure 5.15. Propulsive Efficiency for the Biplane Configuration

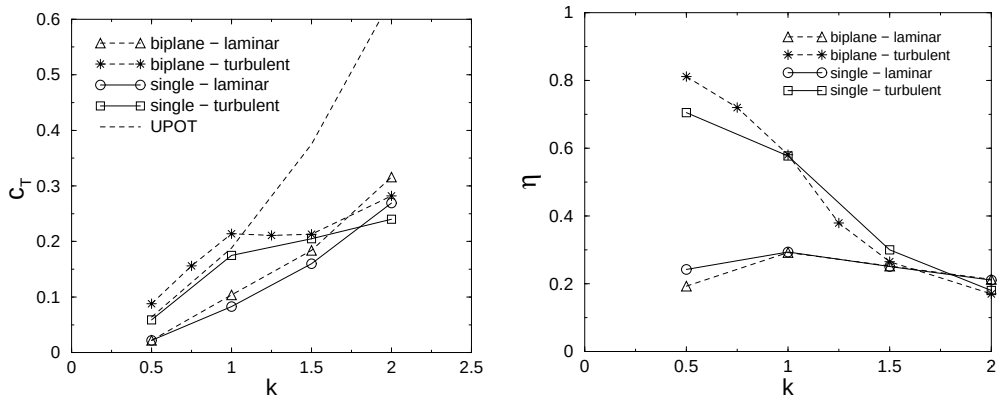

(a) (b)

Figure 5.16. Comparison between the Biplane and the Single-Airfoil Configurations

B. TRANSONIC FLUTTER

A major conclusion by Castro et al. [11] was identifying how significant the porosity of the wind-tunnel walls was on predicting transonic steady and unsteady flow characteristics of the airfoil inside the wind tunnel. The current work was conducted in order to further investigate the effect of porosity of the walls and to improve the method of prescribing such a boundary condition. Therefore, the approach adopted was based on determining a porous boundary condition that yielded a steady-state surface pressure distribution for the NLR 7301 airfoil, in the presence of the wind-tunnel walls, which best agreed with the experiments of Schewe et al. [31]. Once a satisfactory porous boundary condition was determined, the flutter computations were performed. Adjusting other flow parameters of the experiment, such as inflow and outflow boundary conditions, was not attempted since they were not given in [31]. The wind-tunnel test was performed at a Mach number of $M_\infty = 0.768$, an angle of attack of $\alpha = 1.28$ degrees, and a Reynolds number of $Re = 1.727 \times 10^6$. The same flow conditions were used in the present simulation, since no corrections were applied to the experimental data [31]. The plenum pressure was always kept equal to the free-stream pressure ($p_{plenum} = p_\infty$). The results for the steady calculations were used as the start for the unsteady simulations.

All steady-state and unsteady computations were performed using a C-type 281×81 point main-block grid (1), shown in Fig. 5.17, which was generated from the original NLR 7301 airfoil surface data. Blocks (2) and (3) were Cartesian-type and contained 41×41 and 41×61 points along the streamwise and the normal directions, respectively. The Spalart-Allmaras (S-A) and Baldwin-Lomax (B-L) turbulence models were used throughout the course of the unsteady computations for the NLR 7301 airfoil.

All the computations were performed in a time-accurate mode using a constant time step. For fixed angles of incidence, the solution was run for a long time after convergence in residuals

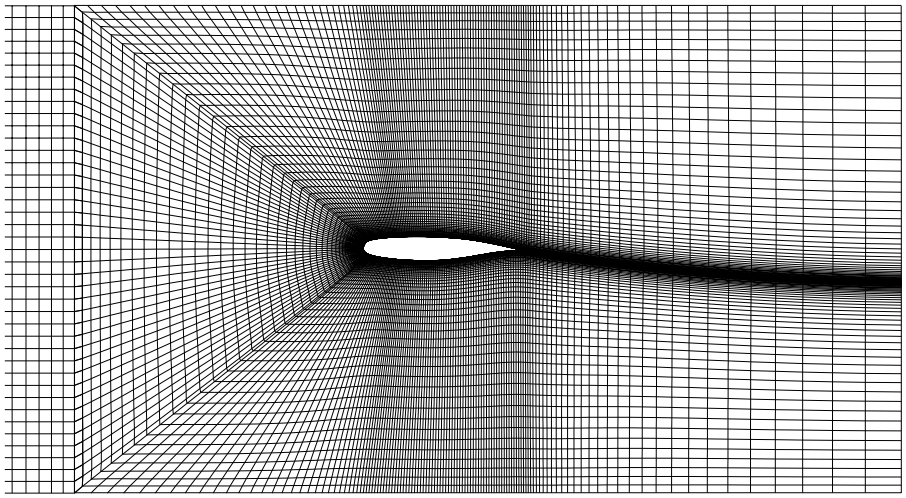

Figure 5.17. C-Type Grid near the NLR 7301 Airfoil

so that variations in all aerodynamic coefficients were reduced to machine zero. This was done in order to ensure that all flow disturbances from the initial transients were swept out of the domain. At convergence, all solutions at fixed angles of incidence did not exhibit any unsteadiness.

A grid-sensitivity study was performed previously by Weber et al. [55] showing that results were not significantly changed for grid sizes of 221×91 with an initial wall spacing of 2×10^{-5}, which yields $y^+ \leq 1.0$, with 40 points in the wake and with the far-field boundary placed 20 chord lengths away from the airfoil surface. Therefore, an initial wall spacing of 1×10^{-5} was chosen to keep $y^+ \approx 1.0$ even for unsteady computations. The grid size of 281×81 chosen for block (1) of the present computations guarantees that there will be 40 points in the wake. Furthermore, because the far-field boundary is placed at the tunnel walls and not 20 chord lengths away from the airfoil, 81 grid points in the ζ direction are sufficient to guarantee a reasonable grid resolution away from the airfoil.

A time-sensitivity analysis was conducted in the present work. The time step used in the present investigation was such that a minimum of $2,400$ iterations per cycle of oscillation was applied to each one of the unsteady cases. The time step of some unsteady computations was divided by two, and no significant change in the flutter frequency or inter-modal phase angle was observed. However, a reduction of approximately 5% on the flutter amplitudes occurred for these cases. As seen later in this section, other parameters influenced the flutter amplitudes much more strongly than the time step. Therefore, most of the effort was concentrated in studying the influence of these parameters rather than the influence of the time step. Furthermore, the computational cost of using a finer time resolution for most of the unsteady simulations would be enormous.

1. Steady-State Computations

First, a computation for a solid wind tunnel wall was performed using the S-A turbulence model. The normal component of the velocity at the walls was set to zero and the other flow variables were extrapolated from the interior points of the grid. The pressure distribution for this case is presented in Fig. 3.16 and compared with the averaged pressure distribution of Schewe et al. [31]. The agreement with the experiment can be further improved, as discussed in the previous work [11], by modeling the porosity of the wind-tunnel walls.

The model for the porosity of the wall, based on the theory presented by Mokry et al. [35], Eq. (3.2), was evaluated next. The pressure distributions for 25% and 50% wall porosity parameters are presented in Fig. 5.18. The porous, inviscid boundary condition was used for these cases. It can be seen that a better agreement with the experiment is achieved for a porous boundary condition than for the solid wall. That the turbulence model has a significant influence on the prediction of the shock location is also clear.

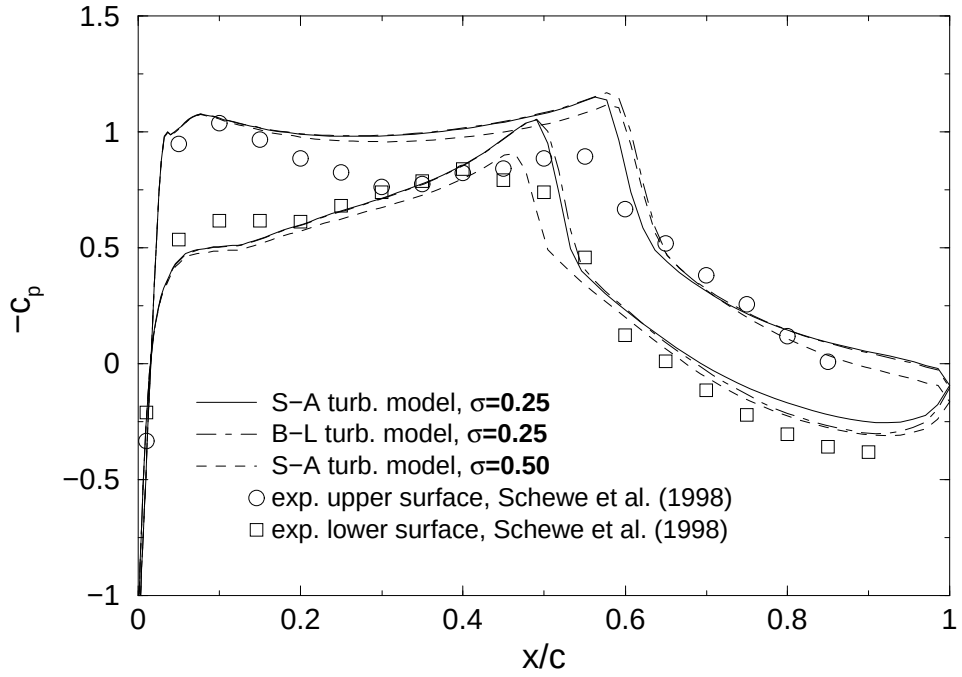

Figure 5.18. Surface Pressure Distribution for a Porous, Inviscid Boundary Condition at the Tunnel Walls

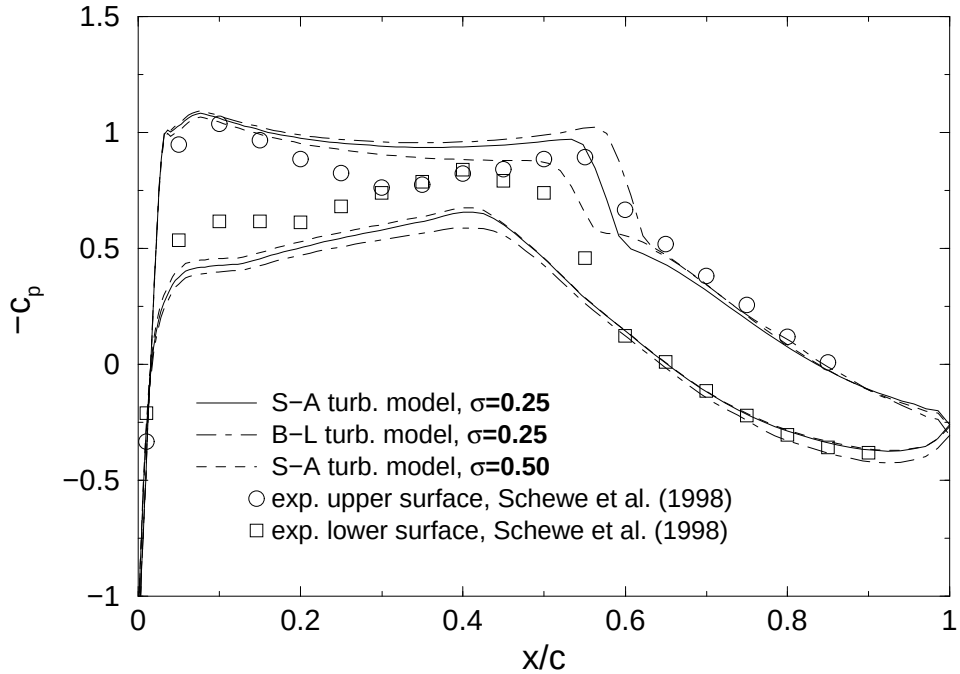

Figure 5.19. Surface Pressure Distribution for a Porous, Viscous Boundary Condition at the Tunnel Walls

The porous, viscous model was also tested for porosity parameters of $\sigma = 0.25$ and $\sigma = 0.50$ and yielded slightly better agreement with the experiment than the porous, inviscid model. The comparison of the pressure distributions with the experimental results for this case are shown in Fig. 5.19. The porosity parameter of $\sigma = 0.25$ seems to yield a better agreement with the time-averaged pressure distribution of [31], predicting a better location for the upper shock. Once again, the turbulence model significantly affects the computed shock location.

In summary, the steady-state computations demonstrate that the porosity of the walls has a very strong influence on the computed flow field around the NLR 7301 airfoil. Additionally, the method of applying the corresponding boundary condition and the turbulence model are influential.

2. Flutter Computations

Based on the conclusions drawn from the steady computations, the flutter simulations were performed using the porous model for the wind-tunnel walls. The nominal conditions of the wind-tunnel test were preserved, namely $M_\infty = 0.768$, $\alpha_i = 1.28$ degrees, and $Re = 1.727 \times 10^6$, as well as the spring-neutral angle of attack $\alpha_0 = 1.91$ degrees. Note that these values were modified in [55], to account for wind-tunnel interference, to $M_\infty = 0.753$, $\alpha_{ic} = -0.08$ degrees, $Re = 1.727 \times 10^6$, and $\alpha_{0c} = 0.635$ degrees. All time-accurate flutter computations were performed assuming fully turbulent flow using the Spalart-Allmaras and Baldwin-Lomax turbulence models. The computations predicted flutter in two degrees of freedom. Limit-cycle oscillations (LCO) were computed in agreement with the wind-tunnel test.

In the experimental test case [31], limit-cycle oscillations in pitch and plunge were reported. The experiment was conducted at a total pressure of 0.45 bar and a dynamic pressure of 0.126 bar. A time-averaged angle of attack of $\bar{\alpha} = 1.28$ degrees was measured for an angle of attack at wind-off condition of $\alpha_0 = 1.91$ degrees, which is equivalent to the spring-neutral angle of attack in the numerical simulation. The porosity parameter associated with the perforated wall of the DLR-Göttingen wind tunnel was stated as $\sigma = 0.25$. The holes in the wall were drilled at an angle of 30 degrees with respect to the surface of the wall. No measurements of the pressure at the wall were performed; therefore, the plenum pressure was assumed to be the free-stream pressure in the present study. The dimensionless structural parameters of the experiment are summarized in Table 5.2. The same parameters were used for the aeroelastic computation.

Initially, the flutter computations were started based on a porosity parameter of $\sigma = 0.25$. Time histories of the angle of attack for a porous, inviscid boundary condition at the tunnel walls are shown in Figs. 5.20 and 5.21 for the S-A and B-L turbulence models, respectively. Note that LCO has not been achieved for both turbulence models. The initial oscillations damp out and the

Table 5.2. Structural Parameters

$x_p =$ 0.2500	$k_\alpha =$ 0.3330
$x_\alpha =$ 0.0484	$k_h =$ 0.2540
$m =$ 946.00	$\delta_\alpha =$ 0.0041
$I_\alpha =$ 33.900	$\delta_h =$ 0.0073

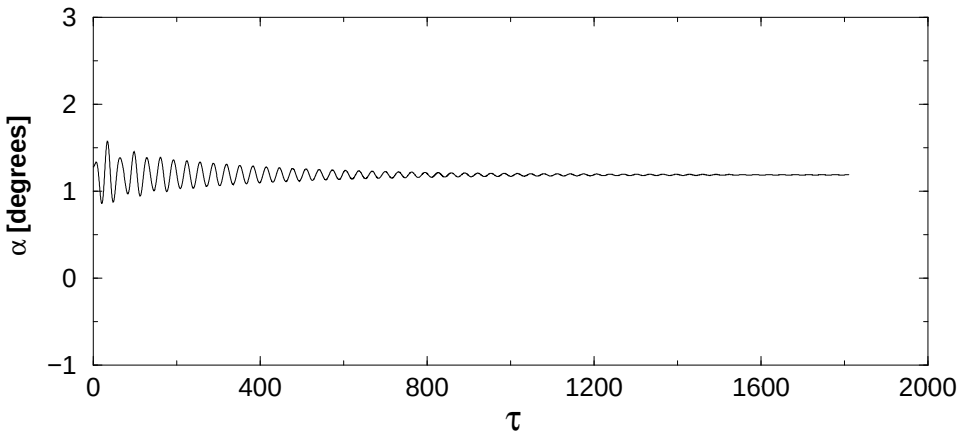

Figure 5.20. Angle-of-Attack History for $\sigma = 0.25$, Porous, Inviscid BC, and S-A Turb. Model

computations converge to a steady value of the angle of attack. For the B-L model, the oscillations are erratic after some time, showing a different behavior from the S-A turbulence model.

Next, a porous, viscous boundary condition was evaluated. Time histories of the angle of attack for this case are presented in Fig. 5.22 and 5.23. For a porous, viscous model, LCO is clearly achieved for both the S-A and B-L turbulence models, but the amplitudes are higher than the reported experimental values of Knipfer et al [31]. The flutter results for the computations are summarized in Table 5.3. Differently from the porous, inviscid model, the behavior of the solutions for the porous, viscous boundary condition is similar for both turbulence models. No erratic oscil-

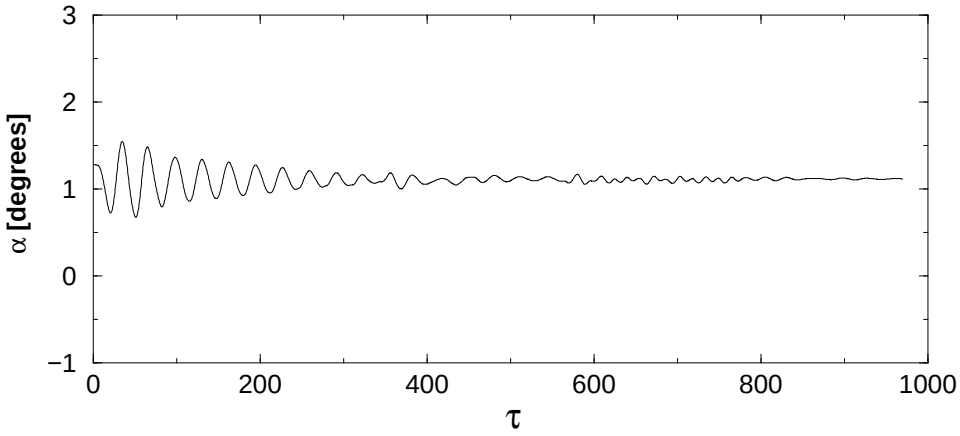

Figure 5.21. Angle-of-Attack History for $\sigma = 0.25$, Porous, Inviscid BC, and B-L Turb. Model

lations are present and the flutter parameters are predicted closely. Therefore, no significant effect of the turbulence model on computations with the porous, viscous model existed.

The computations for $\sigma = 0.25$ show that the type of boundary condition for the porous wall can lead to different unsteady solutions. LCO is obtained for the porous, viscous boundary condition in which the flow is essentially vertical at the wall, but for the porous, inviscid boundary condition, the flow is almost tangent to the wall and the motion is damped. In fact, neither the viscous nor the inviscid boundary condition accurately models the details of the near-wall flow of the experiment. The experiment used holes drilled at 30 degrees imposing a curvature to the flow. The approach adopted in the present work uses two extreme conditions of flow curvature represented by the porous, inviscid and viscous boundary conditions (tangent and normal, respectively). The curvature of the flow in the experiment is between these two extreme values. Fortunately, the experimental LCO amplitudes also lie between the computed amplitudes for the two types of boundary condition. This fact suggests that the porous boundary condition for the wind-tunnel walls significantly improves the computations of LCO for the NLR 7301 inside the DLR-Göttingen wind tunnel.

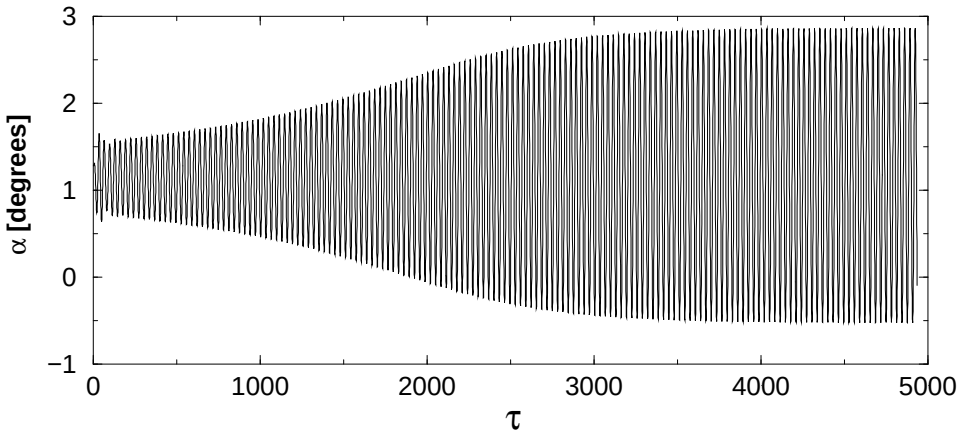

Figure 5.22. Angle-of-Attack History for $\sigma = 0.25$, Porous, Viscous BC, and S-A Turb. Model

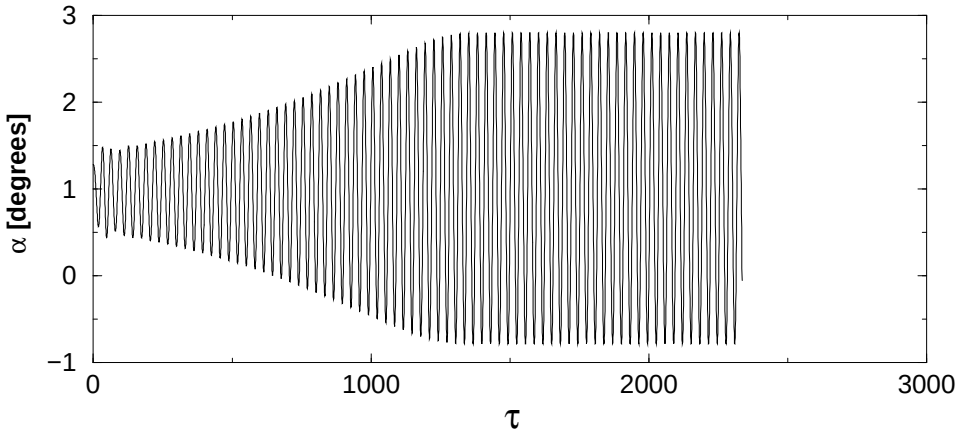

Figure 5.23. Angle-of-Attack History for $\sigma = 0.25$, Porous, Viscous BC, and B-L Turb. Model

Table 5.3. Flutter Results

method	$\bar{\alpha}$ [deg]	$\hat{\alpha}$ [deg]	$\hat{h}$ [mm]	f [Hz]	Φ [deg]
Exp.[a]	1.28	0.18	0.65	32.85	176.7
S-A[b]	1.19	0.00	0.00	34.4	166
S-A[c]	1.15	1.70	4.68	34.5	165
B-L[b]	1.11	0.00	0.00	-	-
B-L[c]	0.98	1.79	5.00	34.6	165
S-A[d]	1.24	0.78	2.9	36.7	149
S-A[e]	0.07	3.78	11.1	32.30	171.8

[a] = without wind-tunnel corrections.

[b] = with porous, inviscid wall; $\sigma = 0.25$.

[c] = with porous, viscous wall; $\sigma = 0.25$.

[d] = previous work; with 50% porosity.

[e] = [55]; fully turbulent (unbounded computation).

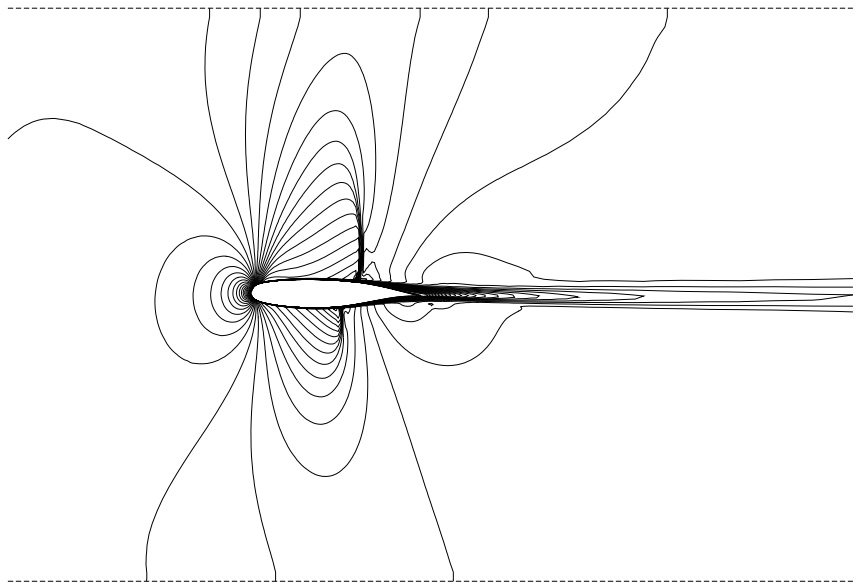

Figure 5.24. Mach Contour Lines for Porosity $\sigma = 0.25$ and Porous, Inviscid Boundary Condition

The Mach contour lines of the flow field near the airfoil for the porous, inviscid and porous, viscous boundary conditions are presented in Figs. 5.24 and 5.25, respectively. The Mach contours lines go from $M = 0$ to $M = 2.0$ with an increment of $\Delta M = 0.05$ for both cases. The flow goes to a relatively low speed near the porous walls for the porous, viscous boundary condition case, as shown in Fig. 5.25. For the porous, inviscid boundary condition, the flow near the tunnel walls remains at a relatively high speed, as shown in Fig. 5.24.

In order to study the influence of the porosity parameter of the wind-tunnel walls in predicting limit-cycle oscillations, a parametric variation of σ was conducted. First, a porous, inviscid boundary condition was used to compute a solution for a porosity parameter of 50%. The time history of the angle of attack shows that the LCO was never achieved and the initial oscillations damp out as illustrated in Fig. 5.26. Next, several cases were run for different values of the porosity parameter using the porous, viscous boundary condition. The LCO amplitudes obtained in those runs

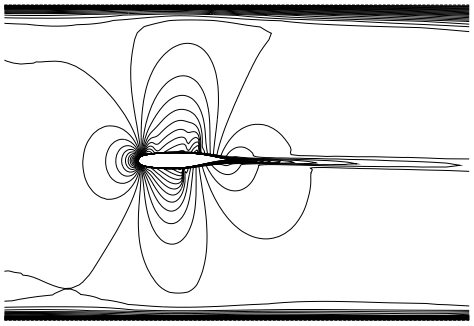

$\alpha = -0.34^o$; $\phi = 0^o$

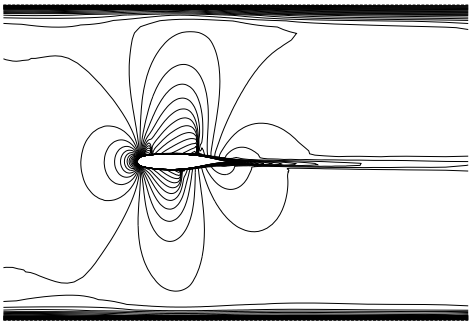

$\alpha = 0.63^o$; $\phi = 60^o$

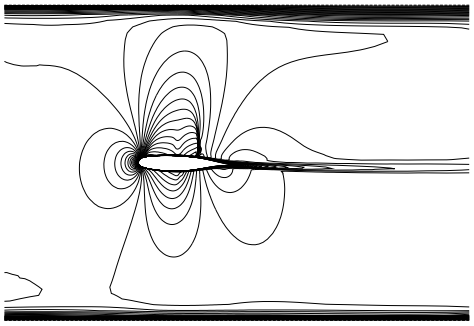

$\alpha = 2.04^o$; $\phi = 120^o$

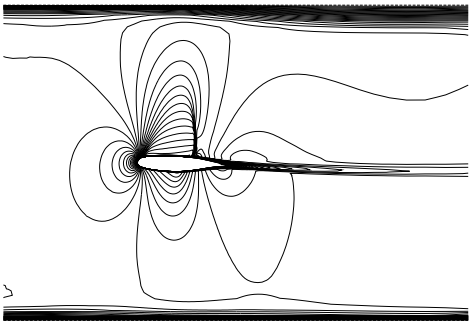

$\alpha = 2.63^o$; $\phi = 180^o$

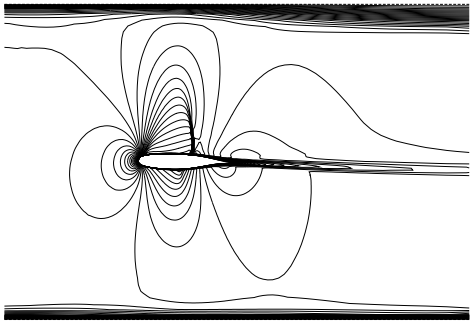

$\alpha = 1.64^o$; $\phi = 240^o$

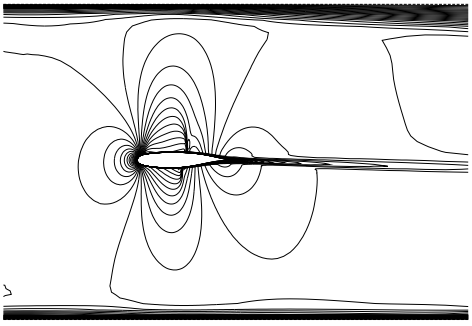

$\alpha = 0.14^o$; $\phi = 300^o$

Figure 5.25. Mach Contour Lines for Porosity $\sigma = 0.25$ and Porous, Viscous Boundary Condition

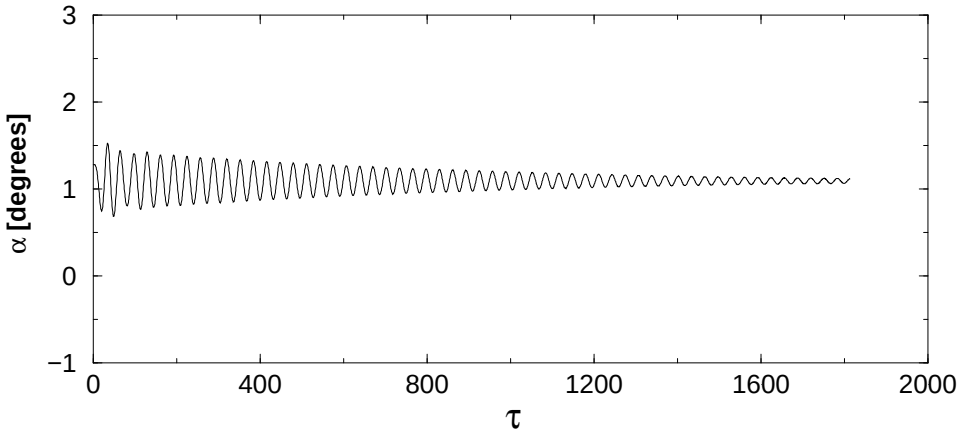

Figure 5.26. Angle-of-Attack History for $\sigma = 0.50$, Porous, Inviscid BC, and S-A Turb. Model

are shown in Fig. 5.27. These results are also provided in Table 5.4. That the porosity parameter also has a significant influence on the LCO amplitudes is clear. Because of the flow curvature at the porous walls, the LCO amplitudes are expected to be smaller than the ones presented in Fig. 5.27 and Table 5.4. Nevertheless, the influence of the porosity parameter is believed to be the same. Final results for the flutter computations, including flutter frequency, phase, amplitudes $\hat{\alpha}$ and $\hat{h}$, and mean angle of attack $\bar{\alpha}$, are shown in Tables 5.3 and 5.4.

The influence of the tunnel blockage was also investigated. Three more cases were run with different heights of the wind-tunnel test section, H. The nominal condition for the experiment was $H = 1.0m$, which yields $H/c = 3.33$. The additional cases represented $H/c = 5.00$, $H/c = 6.67$, and $H/c = \infty$ (unbounded flow). All nominal values of the experiment were preserved. Note that the unbounded solution, in this case, is different from the results obtained in [55], due to the corrected free-stream conditions they used. The history of the angle-of-attack amplitude for these cases can be seen in Fig. 5.28. The porous, viscous boundary condition with $\sigma = 0.25$ was used at the tunnel walls in all the cases except the unbounded flow. The results show a tendency of decreasing the LCO amplitudes as the height of the test section H is increased. For $H/c = 5.00$, the oscillations

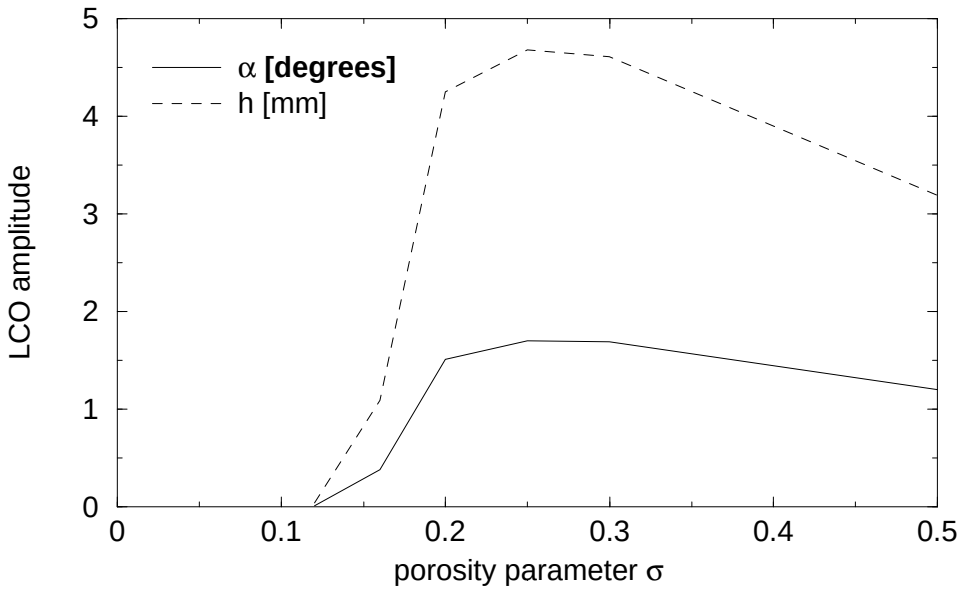

Figure 5.27. Variation of LCO Amplitudes with the Porosity Parameter

Table 5.4. LCO Computations

σ	$\bar{\alpha}$ [deg]	$\hat{\alpha}$ [deg]	$\hat{h}$ [mm]	f [Hz]	Φ [deg]
0.12	1.10	0.01	0.04	34.7	164
0.16	1.11	0.38	1.09	34.5	165
0.20	1.12	1.51	4.25	34.6	165
0.25	1.15	1.70	4.68	34.5	165
0.30	1.17	1.69	4.61	34.3	167
0.50	1.17	1.20	3.19	34.5	166

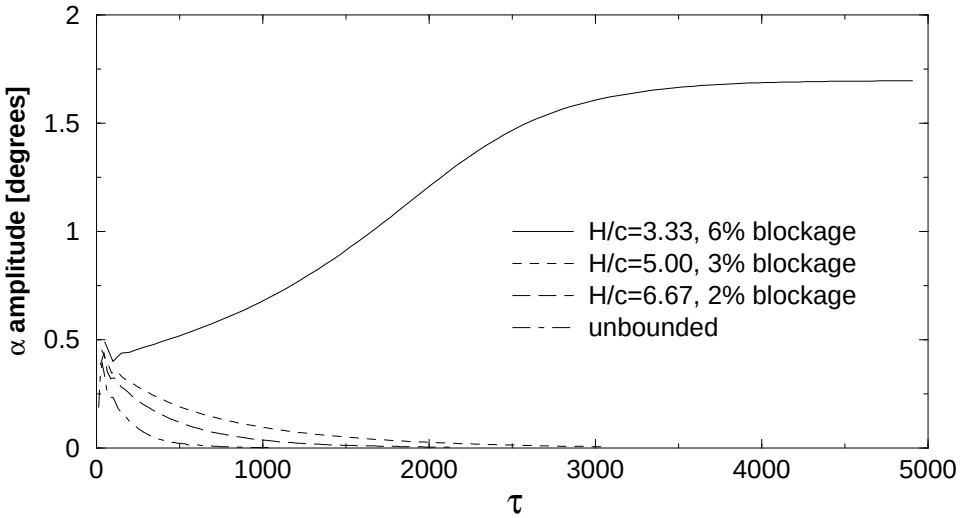

Figure 5.28. Variation of LCO Amplitudes with the Solid Blockage

are already damped out as in the unbounded flow solution. As expected, the results tend to approach the unbounded flow solution as H/c is increased. These results also show that, depending on the value of H/c chosen for the wind-tunnel test, the flutter characteristics of the measurements may differ significantly from the free-flight situation. Moreover, apparently, the variation of the LCO amplitudes with the tunnel blockage is rather non-linear.

The influence of the Mach number on the flutter characteristics of the NLR 7301 airfoil including tunnel walls was studied as well. In order to save computational efforts, the porous, inviscid wall boundary condition was used. This type of wall boundary condition requires a much shorter computational time to achieve LCO. The time history of the angle-of-attack amplitudes for some Mach numbers is presented in Fig. 5.29 for both tunnel and unbounded solutions. The amplitudes for wind-tunnel solutions were always higher than the amplitudes for unbounded flow in the Mach number range of the computations.

The results obtained in this work show that the porosity parameter, the solid blockage of the test section, and the Mach number all have a strong influence on the prediction of the transonic

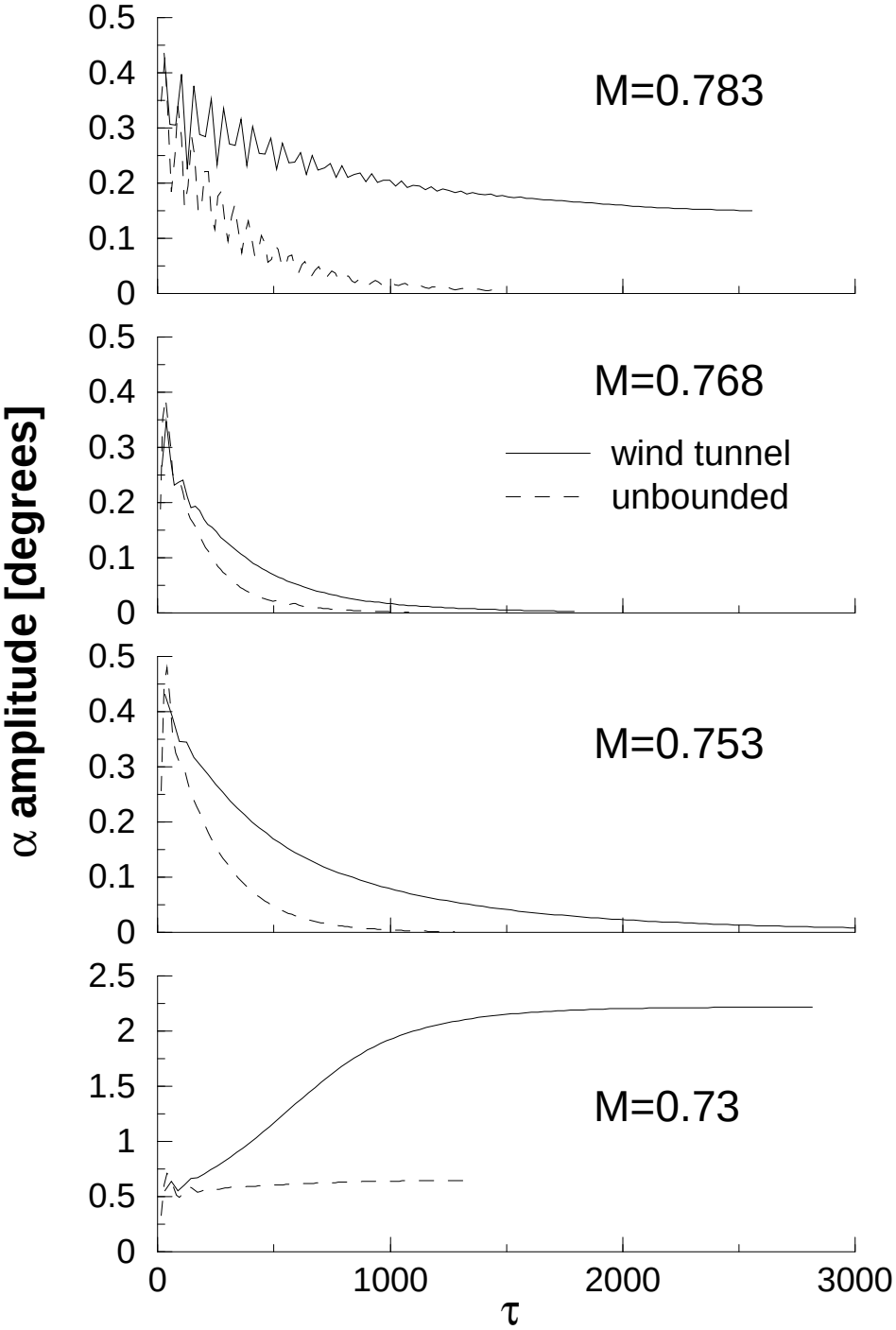

Figure 5.29. Variation of Angle-of-Attack Amplitudes with Mach Number

flutter characteristics of the NLR 7301 airfoil, as indicated in Figs. 5.20 through 5.29. The type of boundary condition used for the porous wind-tunnel wall is also influential. The computed amplitudes of $\hat{\alpha}$ and $\hat{h}$ are larger than the ones measured in the experiment [31] for a porous, viscous boundary condition but lower for a porous, inviscid boundary condition. The type of boundary condition has only a small effect on predicting the flutter frequency and the inter-modal phase angle. These values were predicted more closely in the present work than in [11]. Therefore, it is considered that an improvement was obtained with respect to the previous work [11]. The predicted flutter frequency deviates from the experimental value by 4.9% and the inter-modal phase angle by 11 degrees. Nonetheless, these parameters were predicted more closely by the unbounded flow computations of Weber et al [55]. The values of frequencies, amplitudes, and phase angles were calculated by means of a DFT-analysis of the last 10 cycles.

Although the amplitudes were overpredicted or underpredicted depending on the type of wall boundary condition, the limit-cycle oscillation phenomenon was correctly predicted and the frequency and the inter-modal phase angle were computed within a reasonable accuracy. It must be kept in mind that the plenum chamber pressure was assumed to be the free-stream pressure. Also, inevitably, other uncertain factors exist. It appears, then, that the wind-tunnel porosity model used in the present computations significantly improves the prediction of flutter characteristics of wind-tunnel flows.

VI. CONCLUSIONS AND RECOMMENDATIONS

A parallel version of the solver was implemented and compared with the single-processor version. The parallel code reduced the wall-clock time required for a solution and yielded identical results to the single-processor solution for both steady-state and unsteady computations. A cluster of Linux PC's was used to conduct the computations for both problems under investigation in this work.

The reason for studying the airfoil-in-ground-effect problem is to understand the physics of the low-speed flow over the opposed-plunge biplane of the NPS's micro-air vehicle. When using a compressible solver for high reduced frequencies, the local Mach number may reach supersonic values at which compressibility effects are dominant, as discussed in Chapter V. Since the micro-air vehicle will fly at much lower Mach regimes, predictions using compressible solvers may not capture the correct physics of this problem. Furthermore, as indicated by Anderson [3], it appears that dynamic-stall-vortex capture at high reduced-frequencies makes thrust generation more efficient. Hence, in order to investigate numerically motions with high reduced-frequencies, the use of an incompressible solver would be more appropriate because it would avoid compressibility effects.

Another important issue is the thin-boundary-layer assumption. Micro-air vehicles fly at low Reynolds numbers and, in such case, this assumption is questionable because boundary layers are relatively thick at this regime. Therefore, it is more appropriate to use an incompressible, full Navier-Stokes code to study numerically the unsteady flow over the biplane wing of the NPS's micro-air vehicle for low Mach and Reynolds numbers.

The Spalart-Allmaras turbulence model was modified so that it would work with moving and deforming grids. This change is important because this model was developed for fixed grids

and the convection of vorticity was not correctly predicted for moving or changing grids. This change alone is insufficient to work with moving and deforming grids. The turbulence model must also be solved with the same time step as the conservation equations. In some solvers, a relaxation scheme is used in which the time step for the turbulence model is different from the time step used for the conservation equations. Since relaxation is used in the present solver, the Spalart-Allmaras turbulence model must be further modified to be time accurate.

It was found that assuming fully laminar flow for the airfoil-in-ground-effect problem delivered the best agreement with the experiments conducted by Lund [34]. Despite the limitations of the solver, the agreement of the numerical predictions with the experiments was good for reduced frequencies up to $k = 2.0$. Beyond this value, compressibility effects played a major role in the numerical predictions. Therefore, computations were not attempted for values of reduced frequency beyond $k = 2.0$.

A study of the trailing-edge boundary condition revealed that the manner in which it is implemented in the flow solver is influential when there are non-linearities in the flow field. For unsteady flows with low induced angles of attack, where the flow is always attached to the airfoil, almost no difference was found in the computations when using the free or the averaged TE boundary conditions. However, if the induced angle of attack was high enough to generate dynamic stall, the computed solution was sensitive to the TE boundary condition. When non-linearities are present, the predicted solution is no longer periodic. Instead, the predicted solution follows an attractor, as shown in Chapter III. Although the fine detail of the solution is dependent on the type of TE boundary condition, the attractor followed by the solution is apparently not significantly influenced. A similar behavior was found regarding the influence of the turbulence model. When non-linearities are present, the solution is significantly affected by the use of the S-A or the B-L turbulence models.

In the present solver, the boundary conditions are computed explicitly. The grid-cut boundary conditions are obtained by means of linear interpolation and the airfoil surface boundary conditions are performed using a first-order extrapolation for Euler computations and zeroth-order extrapolations for Navier-Stokes calculations. An improvement on the accuracy of the solver could be obtained by computing the cut boundary conditions implicitly and using higher-order extrapolations for the airfoil surface boundary conditions.

An improved method of modeling the porosity of the wind tunnel walls was implemented. Two different models were tested. One adopted the approach presented by Mokry et al. [35], in which the normal velocity through the porous region was proportional to the pressure difference between the plenum chamber and the test section. The other consisted of a viscous approach assuming the same normal velocity but no tangential component at the porous region of the wind-tunnel walls. The modeling of the tunnel wall porosity and the way the corresponding boundary condition was applied (viscous or inviscid) were both found to affect the numerical predictions of the steady-state and flutter characteristics significantly. The improved porosity models also allowed more flexibility for the generation of the grid because the requirement for an almost equally spaced grid at the porous region of the walls was no longer necessary.

The transonic two-degree-of-freedom bending/torsion flutter analysis of the NLR 7301 supercritical airfoil section was performed with tunnel walls modeled with an improved porosity boundary condition. This model showed that the porosity parameter influences significantly the prediction of the limit-cycle amplitudes. On the other hand, the computed phase angle between pitch and plunge motions and the flutter frequency were not significantly affected by the porosity parameter.

The main conclusion for the wind-tunnel interference problem is that the limit-cycle flutter amplitudes can be quite sensitive to the chosen wind-tunnel wall porosity. In fact, flutter may

be suppressed completely for a sufficiently small value of the porosity parameter. Furthermore, the free-flight flutter behavior may differ substantially from the behavior found in a porous wind tunnel, depending on the chosen porosity and blockage ratio. Consequently, further investigation is necessary to assess the modeling of the porous wall boundary condition and the correlation between wind-tunnel tests and free-flight conditions.

APPENDIX A: DEFORMING GRID EQUATIONS

Navier-Stokes equations in non-dimensional form:

$$\frac{\partial Q}{\partial t} + \frac{\partial F}{\partial x} + \frac{\partial G}{\partial z} = Re^{-1}\left(\frac{\partial F}{\partial x} + \frac{\partial G}{\partial z}\right) \tag{A.1}$$

where $Q = (\rho, \rho u, \rho w, e)^T$.

For the LHS of Eq. (A.1):

$$\begin{aligned}
Q = Q(x,z,t) = Q(\xi,\zeta,\tau) &\Rightarrow \tfrac{\partial Q}{\partial t} = \tfrac{\partial \xi}{\partial t}\tfrac{\partial Q}{\partial \xi} + \tfrac{\partial \zeta}{\partial t}\tfrac{\partial Q}{\partial \zeta} + \tfrac{\partial \tau}{\partial t}\tfrac{\partial Q}{\partial \tau} = \xi_t Q_\xi + \zeta_t Q_\zeta + Q_\tau \\
F = F(x,z,t) = F(\xi,\zeta,\tau) &\Rightarrow \tfrac{\partial F}{\partial x} = \tfrac{\partial \xi}{\partial x}\tfrac{\partial F}{\partial \xi} + \tfrac{\partial \zeta}{\partial x}\tfrac{\partial F}{\partial \zeta} + \tfrac{\partial \tau}{\partial x}\tfrac{\partial F}{\partial \tau} = \xi_x F_\xi + \zeta_x F_\zeta \\
G = G(x,z,t) = G(\xi,\zeta,\tau) &\Rightarrow \tfrac{\partial G}{\partial z} = \tfrac{\partial \xi}{\partial z}\tfrac{\partial G}{\partial \xi} + \tfrac{\partial \zeta}{\partial z}\tfrac{\partial G}{\partial \zeta} + \tfrac{\partial \tau}{\partial z}\tfrac{\partial G}{\partial \tau} = \xi_z G_\xi + \zeta_z G_\zeta
\end{aligned} \tag{A.2}$$

Similarly:

$$\frac{\partial R}{\partial x} = \xi_x R_\xi + \zeta_x R_\zeta \quad \text{and} \quad \frac{\partial S}{\partial z} = \xi_z S_\xi + \zeta_z S_\zeta \tag{A.3}$$

Substituting Eqs. (A.2) and (A.3) into Eq. (A.1):

$$\xi_t Q_\xi + \zeta_t Q_\zeta + Q_\tau + \xi_x F_\xi + \zeta_x F_\zeta + \xi_z G_\xi + \zeta_z G_\zeta = Re^{-1}(\xi_x R_\xi + \zeta_x R_\zeta + \xi_z S_\xi + \zeta_z S_\zeta) \tag{A.4}$$

Let Q be rescaled by the Jacobian by defining $\hat{Q} = J^{-1}Q$. Then:

$$
\begin{aligned}
(J^{-1}Q)_\tau &= J^{-1}Q_\tau + (J^{-1})_\tau Q \Rightarrow Q_\tau = J[(J^{-1}Q)_\tau - (J^{-1})_\tau Q] \\
(J^{-1}\xi_t Q)_\xi &= J^{-1}\xi_t Q_\xi + (J^{-1}\xi_t)_\xi Q \Rightarrow \xi_t Q_\xi = J[(J^{-1}\xi_t Q)_\xi - (J^{-1}\xi_t)_\xi Q] \\
(J^{-1}\zeta_t Q)_\zeta &= J^{-1}\zeta_t Q_\zeta + (J^{-1}\zeta_t)_\zeta Q \Rightarrow \zeta_t Q_\zeta = J[(J^{-1}\zeta_t Q)_\zeta - (J^{-1}\zeta_t)_\zeta Q] \\
(J^{-1}\xi_x F)_\xi &= J^{-1}\xi_x F_\xi + (J^{-1}\xi_x)_\xi F \Rightarrow \xi_x F_\xi = J[(J^{-1}\xi_x F)_\xi - (J^{-1}\xi_x)_\xi F] \\
(J^{-1}\zeta_x F)_\zeta &= J^{-1}\zeta_x F_\zeta + (J^{-1}\zeta_x)_\zeta F \Rightarrow \zeta_x F_\zeta = J[(J^{-1}\zeta_x F)_\zeta - (J^{-1}\zeta_x)_\zeta F] \\
(J^{-1}\xi_z G)_\xi &= J^{-1}\xi_z G_\xi + (J^{-1}\xi_z)_\xi G \Rightarrow \xi_z G_\xi = J[(J^{-1}\xi_z G)_\xi - (J^{-1}\xi_z)_\xi G] \\
(J^{-1}\zeta_z G)_\zeta &= J^{-1}\zeta_z G_\zeta + (J^{-1}\zeta_z)_\zeta G \Rightarrow \zeta_z G_\zeta = J[(J^{-1}\zeta_z G)_\zeta - (J^{-1}\zeta_z)_\zeta G] \\
(J^{-1}\xi_x R)_\xi &= J^{-1}\xi_x R_\xi + (J^{-1}\xi_x)_\xi R \Rightarrow \xi_x R_\xi = J[(J^{-1}\xi_x R)_\xi - (J^{-1}\xi_x)_\xi R] \\
(J^{-1}\zeta_x R)_\zeta &= J^{-1}\zeta_x R_\zeta + (J^{-1}\zeta_x)_\zeta R \Rightarrow \zeta_x R_\zeta = J[(J^{-1}\zeta_x R)_\zeta - (J^{-1}\zeta_x)_\zeta R] \\
(J^{-1}\xi_z S)_\xi &= J^{-1}\xi_z S_\xi + (J^{-1}\xi_z)_\xi S \Rightarrow \xi_z S_\xi = J[(J^{-1}\xi_z S)_\xi - (J^{-1}\xi_z)_\xi S] \\
(J^{-1}\zeta_z S)_\zeta &= J^{-1}\zeta_z S_\zeta + (J^{-1}\zeta_z)_\zeta S \Rightarrow \zeta_z S_\zeta = J[(J^{-1}\zeta_z S)_\zeta - (J^{-1}\zeta_z)_\zeta S]
\end{aligned}
\tag{A.5}
$$

Substituting Eq. (A.5) into Eq. (A.4) and dividing by J:

$$
\begin{aligned}
& (J^{-1}Q)_\tau - (J^{-1})_\tau Q + (J^{-1}\xi_t Q)_\xi - (J^{-1}\xi_t)_\xi Q + (J^{-1}\zeta_t Q)_\zeta - (J^{-1}\zeta_t)_\zeta Q \\
& + (J^{-1}\xi_x F)_\xi - (J^{-1}\xi_x)_\xi F + (J^{-1}\zeta_x F)_\zeta - (J^{-1}\zeta_x)_\zeta F \\
& + (J^{-1}\xi_z G)_\xi - (J^{-1}\xi_z)_\xi G + (J^{-1}\zeta_z G)_\zeta - (J^{-1}\zeta_z)_\zeta G \\
= \; & Re^{-1}[(J^{-1}\xi_x R)_\xi - (J^{-1}\xi_x)_\xi R + (J^{-1}\zeta_x R)_\zeta - (J^{-1}\zeta_x)_\zeta R \\
& + (J^{-1}\xi_z S)_\xi - (J^{-1}\xi_z)_\xi S + (J^{-1}\zeta_z S)_\zeta - (J^{-1}\zeta_z)_\zeta S]
\end{aligned}
\tag{A.6}
$$

Rearranging terms in Eq. (A.6) and using the definitions of $\hat{Q}$, $\hat{\xi}$ and $\hat{\zeta}$:

$$
\begin{aligned}
& (\hat{Q})_\tau - Q[(J^{-1})_\tau + (\hat{\xi}_t)_\xi + (\hat{\zeta}_t)_\zeta] + (\hat{\xi}_t Q + \hat{\xi}_x F + \hat{\xi}_z G)_\xi + (\hat{\zeta}_t Q + \hat{\zeta}_x F + \hat{\zeta}_z G)_\zeta \\
& - F[(\hat{\xi}_x)_\xi + (\hat{\zeta}_x)_\zeta] - G[(\hat{\xi}_z)_\xi + (\hat{\zeta}_z)_\zeta] \\
= \; & Re^{-1}\{(\hat{\xi}_x R + \hat{\xi}_z S)_\xi + (\hat{\zeta}_x R + \hat{\zeta}_z S)_\zeta - R[(\hat{\xi}_x)_\xi + (\hat{\zeta}_x)_\zeta] - S[(\hat{\xi}_z)_\xi + (\hat{\zeta}_z)_\zeta]\}
\end{aligned}
\tag{A.7}
$$

Expanding some terms:

$$(J^{-1})_\tau = (x_\xi z_\zeta - x_\zeta z_\xi)_\tau = x_{\xi\tau} z_\zeta + x_\xi z_{\zeta\tau} - x_{\zeta\tau} z_\xi - x_\zeta z_{\xi\tau} \tag{A.8}$$

$$(\hat{\xi}_t)_\xi = (x_\zeta z_\tau - x_\tau z_\zeta)_\xi = x_{\xi\zeta} z_\tau + x_\zeta z_{\xi\tau} - x_{\xi\tau} z_\zeta - x_\tau z_{\xi\zeta} \tag{A.9}$$

$$(\hat{\zeta}_t)_\zeta = (x_\tau z_\xi - x_\xi z_\tau)_\zeta = x_{\zeta\tau} z_\xi + x_\tau z_{\xi\zeta} - x_{\xi\zeta} z_\tau - x_\xi z_{\zeta\tau} \tag{A.10}$$

Combining Eqs. (A.8), (A.9), and (A.10):

$$(J^{-1})_\tau + (\hat{\xi}_t)_\xi + (\hat{\zeta}_t)_\zeta = 0 \tag{A.11}$$

Important to note that Eq. (A.11) is known as the Geometric Conservation Law (GCL). It will be derived again in Appendix B to show that it actually represents the conservation of volume as the grid is changed in time.

Although the RHS of Eq. (A.11) is mathematically zero, it is not the same numerically. The assumption of orthogonality is no longer valid for a deforming grid. Consequently, one should expect some error in the solution when the deformation of the grid is relatively large.

Expanding more terms:

$$\begin{aligned} (\hat{\xi}_x)_\xi &= (z_\zeta)_\xi = z_{\xi\zeta} \\ (\hat{\zeta}_x)_\zeta &= (-z_\xi)_\zeta = -z_{\xi\zeta} \end{aligned} \quad \Rightarrow (\hat{\xi}_x)_\xi + (\hat{\zeta}_x)_\zeta = 0 \tag{A.12}$$

$$\begin{aligned} (\hat{\xi}_z)_\xi &= (-x_\zeta)_\xi = -x_{\xi\zeta} \\ (\hat{\zeta}_z)_\zeta &= (x_\xi)_\zeta = x_{\xi\zeta} \end{aligned} \quad \Rightarrow (\hat{\xi}_z)_\xi + (\hat{\zeta}_z)_\zeta = 0 \tag{A.13}$$

Plugging Eqs. (A.12) and (A.13) into Eq. (A.7):

$$\begin{aligned} & (\hat{Q})_\tau + (\hat{\xi}_t Q + \hat{\xi}_x F + \hat{\xi}_z G)_\xi + (\hat{\zeta}_t Q + \hat{\zeta}_x F + \hat{\zeta}_z G)_\zeta \\ = \quad & Re^{-1}[(\hat{\xi}_x R + \hat{\xi}_z S)_\xi + (\hat{\zeta}_x R + \hat{\zeta}_z S)_\zeta] \end{aligned} \tag{A.14}$$

Defining:

$$\begin{aligned} \hat{F} &= \hat{\xi}_t Q + \hat{\xi}_x F + \hat{\xi}_z G \quad \hat{R} = \hat{\xi}_x R + \hat{\xi}_z S \\ \hat{G} &= \hat{\zeta}_t Q + \hat{\zeta}_x F + \hat{\zeta}_z G \quad \hat{S} = \hat{\zeta}_x R + \hat{\zeta}_z S \end{aligned} \tag{A.15}$$

Substituting Eqs. (A.15) into Eq. (A.14):

$$\hat{Q}_\tau + \hat{F}_\xi + \hat{G}_\zeta = Re^{-1}(\hat{R}_\xi + \hat{S}_\zeta) \tag{A.16}$$

Equation (A.16) represents the Navier-Stokes equations in non-dimensional form and written in terms of the computational domain variables. It is important to note that the Navier-Stokes equations are valid for a changing grid because the Jacobian was considered to be a function of time.

APPENDIX B: GEOMETRIC CONSERVATION LAW

The velocity of the grid points on a surface S can be described by $\mathbf{W}_S = (x_\tau, z_\tau)$ for $(x,z) \in S$ and the velocity of all grid points is given by the field $\mathbf{W} = (x_\tau, z_\tau)$.

Geometric Conservation Law (GCL):

$$\frac{d}{dt}\int_V dV = \int_S \mathbf{W}_S \cdot d\mathbf{S} \tag{B.1}$$

Applying the Divergence Theorem:

$$\frac{d}{dt}\int_V dV = \int_V (\nabla \cdot \mathbf{W})\, dV \tag{B.2}$$

But:

$$dV = dx\,dz\,(1) = J^{-1}\,d\xi\,d\zeta\,(1) \Rightarrow \frac{d}{dt}\int_\vartheta J^{-1}\,d\xi\,d\zeta = \int_\vartheta (\nabla \cdot \mathbf{W})\, J^{-1}\,d\xi\,d\zeta \tag{B.3}$$

Expanding the term $(\nabla \cdot \mathbf{W})$:

$$J^{-1}(\nabla \cdot \mathbf{W}) = J^{-1}\left(\frac{\partial u}{\partial x} + \frac{\partial w}{\partial z}\right) = J^{-1}\left(\frac{\partial \xi}{\partial x}\frac{\partial u}{\partial \xi} + \frac{\partial \zeta}{\partial x}\frac{\partial u}{\partial \zeta} + \frac{\partial \xi}{\partial z}\frac{\partial w}{\partial \xi} + \frac{\partial \zeta}{\partial z}\frac{\partial w}{\partial \zeta}\right) \tag{B.4}$$

Rearranging the terms:

$$J^{-1}(\nabla \cdot \mathbf{W}) = J^{-1}(\nabla\xi \cdot \mathbf{W}_\xi + \nabla\zeta \cdot \mathbf{W}_\zeta) \tag{B.5}$$

But:

$$
\begin{aligned}
&(J^{-1}\nabla\xi\cdot\mathbf{W})_\xi = (J^{-1}\nabla\xi)_\xi\cdot\mathbf{W} + J^{-1}\nabla\xi\cdot\mathbf{W}_\xi \\
&\Rightarrow J^{-1}\nabla\xi\cdot\mathbf{W}_\xi = (J^{-1}\nabla\xi\cdot\mathbf{W})_\xi - (J^{-1}\nabla\xi)_\xi\cdot\mathbf{W} \\
&(J^{-1}\nabla\zeta\cdot\mathbf{W})_\zeta = (J^{-1}\nabla\zeta)_\zeta\cdot\mathbf{W} + J^{-1}\nabla\zeta\cdot\mathbf{W}_\zeta \\
&\Rightarrow J^{-1}\nabla\zeta\cdot\mathbf{W}_\zeta = (J^{-1}\nabla\zeta\cdot\mathbf{W})_\zeta - (J^{-1}\nabla\zeta)_\zeta\cdot\mathbf{W}
\end{aligned}
\tag{B.6}
$$

Substituting Eq. (B.6) into Eq. (B.5):

$$
J^{-1}(\nabla\cdot\mathbf{W}) = (J^{-1}\nabla\xi\cdot\mathbf{W})_\xi + (J^{-1}\nabla\zeta\cdot\mathbf{W})_\zeta - \mathbf{W}\cdot[(J^{-1}\nabla\xi)_\xi + (J^{-1}\nabla\zeta)_\zeta] \tag{B.7}
$$

It is also known that:

$$
\begin{aligned}
\nabla\xi\cdot\mathbf{W} &= \left(\tfrac{\partial\xi}{\partial x}\mathbf{i} + \tfrac{\partial\xi}{\partial z}\mathbf{k}\right)\cdot(x_\tau\mathbf{i} + z_\tau\mathbf{k}) = \xi_x x_\tau + \xi_z z_\tau = -J\big(x_\zeta z_\tau - x_\tau z_\zeta\big) = -\xi_t \\
\nabla\zeta\cdot\mathbf{W} &= \left(\tfrac{\partial\zeta}{\partial x}\mathbf{i} + \tfrac{\partial\zeta}{\partial z}\mathbf{k}\right)\cdot(x_\tau\mathbf{i} + z_\tau\mathbf{k}) = \zeta_x x_\tau + \zeta_z z_\tau = -J\big(x_\tau z_\xi - x_\xi z_\tau\big) = -\zeta_t
\end{aligned}
\tag{B.8}
$$

Plugging Eq. (B.8) into Eq. (B.7):

$$
\begin{aligned}
J^{-1}(\nabla\cdot\mathbf{W}) = \quad & -(J^{-1}\xi_t)_\xi - (J^{-1}\zeta_t)_\zeta \\
& -\mathbf{W}\cdot\{[(J^{-1}\xi_x)_\xi + (J^{-1}\zeta_x)_\zeta]\mathbf{i} + [(J^{-1}\xi_z)_\xi + (J^{-1}\zeta_z)_\zeta]\mathbf{k}\}
\end{aligned}
\tag{B.9}
$$

Rearranging terms, performing the dot product and using $\hat{\xi} = J^{-1}\xi$ and $\hat{\zeta} = J^{-1}\zeta$:

$$
\begin{aligned}
J^{-1}(\nabla\cdot\mathbf{W}) \quad &= -(\hat{\xi}_t)_\xi - (\hat{\zeta}_t)_\zeta - x_\tau[(\hat{\xi}_x)_\xi + (\hat{\zeta}_x)_\zeta] - z_\tau[(\hat{\xi}_z)_\xi + (\hat{\zeta}_z)_\zeta] \\
&= -(\hat{\xi}_t)_\xi - (\hat{\zeta}_t)_\zeta - x_\tau[(z_\zeta)_\xi - (z_\xi)_\zeta] - z_\tau[-(x_\zeta)_\xi + (x_\xi)_\zeta] \\
&= -(\hat{\xi}_t)_\xi - (\hat{\zeta}_t)_\zeta
\end{aligned}
\tag{B.10}
$$

Substituting Eq. (B.10) into Eq. (B.3) and assuming that the Jacobian varies continuously:

$$\int_{\vartheta} \partial_\tau(J^{-1})\, d\xi\, d\zeta = \int_{\vartheta} [-(\hat{\xi}_t)_\xi - (\hat{\zeta}_t)_\zeta]\, d\xi\, d\zeta \Rightarrow \int_{\vartheta} [\partial_\tau(J^{-1}) + (\hat{\xi}_t)_\xi + (\hat{\zeta}_t)_\zeta]\, d\xi\, d\zeta = 0 \qquad \text{(B.11)}$$

Hence:

$$\partial_\tau(J^{-1}) + (\hat{\xi}_t)_\xi + (\hat{\zeta}_t)_\zeta = 0 \qquad \text{(B.12)}$$

THIS PAGE INTENTIONALLY LEFT BLANK

APPENDIX C: JACOBIAN MATRICES

A. Matrices $\hat{A}$, $\hat{B}$, and $\hat{M}$

It is necessary to know the matrices $\hat{A}^+$, $\hat{A}^-$, $\hat{B}^+$, $\hat{B}^-$, and $\hat{M}$ in order to apply the numerical method discussed in Chapter II. Matrices $\hat{A}^+$, $\hat{A}^-$, $\hat{B}^+$, and $\hat{B}^-$ are obtained by assuming flux splitting. These matrices arise because matrices $\hat{A}$ and $\hat{B}$ can be written in terms of an eigenvalue factorization:

$$\hat{A} = \Sigma_A \Lambda_A \Sigma_A^{-1} \qquad \text{and} \qquad \hat{B} = \Sigma_B \Lambda_B \Sigma_B^{-1} \tag{C.1}$$

where:

$$\Lambda_A = \begin{bmatrix} \lambda_1^A & 0 & 0 & 0 \\ 0 & \lambda_2^A & 0 & 0 \\ 0 & 0 & \lambda_3^A & 0 \\ 0 & 0 & 0 & \lambda_4^A \end{bmatrix} \qquad \text{and} \qquad \Lambda_B = \begin{bmatrix} \lambda_1^B & 0 & 0 & 0 \\ 0 & \lambda_2^B & 0 & 0 \\ 0 & 0 & \lambda_3^B & 0 \\ 0 & 0 & 0 & \lambda_4^B \end{bmatrix} \tag{C.2}$$

Also, the diagonal matrices Λ_A and Λ_B can be split into the summation of two parts:

$$\lambda_i^A = \lambda_i^{A+} + \lambda_i^{A-} \qquad \text{and} \qquad \lambda_i^B = \lambda_i^{B+} + \lambda_i^{B-} \tag{C.3}$$

where:

$$\lambda_i^+ = \frac{\lambda_i + |\lambda_i|}{2} \qquad \text{and} \qquad \lambda_i^- = \frac{\lambda_i - |\lambda_i|}{2} \tag{C.4}$$

In doing this, matrices $\hat{A}$ and $\hat{B}$ can be written as:

$$\hat{A} = \Sigma_A (\Lambda_A^+ + \Lambda_A^-) \Sigma_A^{-1} \qquad \text{and} \qquad \hat{B} = \Sigma_B (\Lambda_B^+ + \Lambda_B^-) \Sigma_B^{-1} \tag{C.5}$$

1. Matrix $\hat{M}$

$$\hat{M} = \frac{\partial \hat{S}}{\partial \hat{Q}} = \begin{bmatrix} 0 & 0 & 0 & 0 \\ m_{21} & \alpha_1 (1/\rho)_\zeta & \alpha_2 (1/\rho)_\zeta & 0 \\ m_{31} & \alpha_2 (1/\rho)_\zeta & \alpha_3 (1/\rho)_\zeta & 0 \\ m_{41} & m_{42} & m_{43} & \alpha_4 (1/\rho)_\zeta \end{bmatrix} \tag{C.6}$$

where:

$$\begin{gathered} m_{21} = -\alpha_1 (u/\rho)_\zeta - \alpha_2 (w/\rho)_\zeta \qquad m_{31} = -\alpha_2 (u/\rho)_\zeta - \alpha_3 (w/\rho)_\zeta \\ m_{41} = \alpha_4 \left[-e/\rho^2 + (u^2 + w^2)/\rho \right]_\zeta - \alpha_1 (u^2/\rho)_\zeta - 2\alpha_2 (uw/\rho)_\zeta - \alpha_3 (w^2/\rho)_\zeta \\ m_{42} = -\alpha_4 (u/\rho)_\zeta - m_{21} \qquad m_{43} = -\alpha_4 (w/\rho)_\zeta - m_{31} \end{gathered} \tag{C.7}$$

and

$$\alpha_1 = \mu \left(\frac{4}{3} \zeta_x^2 + \zeta_z^2 \right) \quad \alpha_2 = \frac{\mu}{3} \zeta_x \zeta_z \quad \alpha_3 = \mu \left(\zeta_x^2 + \frac{4}{3} \zeta_z^2 \right) \quad \alpha_4 = \frac{\gamma \mu}{Pr} \left(\zeta_x^2 + \zeta_z^2 \right) \tag{C.8}$$

LIST OF REFERENCES

[1] Personal correspondence with Dr. Steven Allmaras, March 2001.

[2] J. M. Anderson, K. Streitlien, D. S. Barrett, and M. S. Triantafyllou. Oscillation Foils of High Propulsive Efficiency. *J. Fluid Mech.*, 360:41–72, 1998.

[3] Jamie M. Anderson. *Vorticity Control for Efficient Propulsion.* PhD thesis, Massachusetts Inst. of Tech. Cambridge, February 1996.

[4] B. S. Baldwin and H. Lomax. Thin–Layer Approximation and Algebraic Model for Separated Turbulent Flows. *AIAA Paper 78–0257*, January 1978.

[5] W. F. Ballhaus and P. M. Goorjian. Computation of Unsteady Transonic Flows by the Indicial Method. *AIAA Journal*, 16:117–124, February 1978.

[6] P. S. Beran and S. Morton. A Continuation Method for the Calculation of Airfoil Flutter Boundaries. *AIAA Paper 97-0574*, January 6–10 1997. Reno, Nevada.

[7] A. Betz. Ein Beitrag zur Erklärung des Segelfluges. *Zeitschrift für Flugtechnik und Motorluftschiffahrt*, 3:269–272, January 1912.

[8] W. Birnbaum. Der Schlagflügelpropeller und die kleinen Schwingungen elastisch befestigter Tragflügel. *Zeitschrift für Flugtechnik und Motorluftschiffahrt*, 15:128–134, 1924.

[9] R. L. Bisplinghoff, H. Ashley, and R. L. Halfman. *Aeroelasticity.* Dover Publications, New York, 1955. ISBN 0-486-69189-6.

[10] B. J. Buxton and P. S. Beran. Validation of Two Shock-Capturing Methods for Calculations of Transonic Airfoil Flutter. *AIAA Paper 97-0834*, January 6–10 1997. Reno, Nevada.

[11] B. M. Castro, J. A. Ekaterinaris, and M. F. Platzer. Transonic Flutter Computations for the NLR7301 Airfoil inside a Wind Tunnel. *AIAA Paper 2000–0984*, January 10–13 2000. Reno, Nevada.

[12] T. Cebeci and J. Cousteix. *Modeling and Computation of Boundary-Layer Flows*. Horizons Publishing, 1998. ISBN 0-9668461-0-9.

[13] S. R. Chakravarthy and S. Osher. Numerical Experiments with the Osher Upwind Scheme for the Euler Equations. *AIAA Journal*, 21(9):1241–1248, September 1983.

[14] M. H. Dickinson, F. O. Lehmann, and S. P. Sane. Wing Rotation and the Aerodynamic Basis of Insect Flight. *Science*, 284:1954–1960, 18 June 1999.

[15] J. A. Ekaterinaris, A. S. Cricelli, and M. F. Platzer. A Zonal Method for Unsteady, Viscous, Compressible Airfoil Flows. *Journal of Fluids and Structures*, 8:107–123, 1994.

[16] J. A. Ekaterinaris and F. R. Menter. Computation of Oscillating Airfoil Flows with One– and Two–Equation Turbulence Models. *AIAA Journal*, 32(12):2359–2365, 1994.

[17] J. A. Ekaterinaris and M. F. Platzer. Numerical Investigation of Stall Flutter. *Journal of Turbomachinery*, 118:197–203, April 1996.

[18] J. A. Ekaterinaris, N. N. Sorensen, and F. Rasmussen. Numerical Investigation of Airfoil Dynamic Stall in Simultaneous Harmonic Oscillatory and Translatory Motion. *ASME Journal of Solar Energy Engineering*, 120:75–83, 1998.

[19] I. E. Garrick. Propulsion of a Flapping and Oscillating Airfoil. Technical Report 567, NACA, 1936.

[20] J. P. Gostelow, N. Melwani, and G. J. Walker. Effects of a Streamwise Pressure Gradient on Turbulent Spot Development. *ASME Journal of Turbomachinery*, 118:737–743, 1996.

[21] K. Isogai, Y. Shinmoto, and Y. Watanabe. Effects of Dynamic Stall Phenomena on Propulsive Efficiency and Thrust of Flapping Airfoil. *AIAA Journal*, 37(10):1145–1151, October 1999.

[22] K. D. Jones, S. Davids, and M. F. Platzer. Oscillating-Wing Power Generation. In *Proceedings of the 3rd ASME/JSME Joint Fluids Engineering Conference*, July 18-23 1999. San Francisco, CA.

[23] K. D. Jones, C. M. Dohring, and M. F. Platzer. Experimental and Computational Investigation of the Knoller-Betz Effect. *AIAA Journal*, 36(7):1240–1246, July 1998.

[24] K. D. Jones, T. C. Lund, and M. F. Platzer. Experimental and Computational Investigation of Flapping-Wing Propulsion for Micro-Air Vehicles. Unpublished.

[25] K. D. Jones and M. F. Platzer. Time-Domain Analysis of Low-Speed Airfoil Flutter. *AIAA Journal*, 34(5):1027–1033, May 1996.

[26] K. D. Jones and M. F. Platzer. On the Prediction of Dynamic Stall Onset on Airfoils in Low Speed Flow. In *Proceedings of 8th Int. Symp. of "Unsteady Aerodynamics and Aeroelasticity of Turbomachines,"* pages 797–812, 14-18 Sept 1997. Stockholm, Sweden.

[27] K. D. Jones and M. F. Platzer. Airfoil Geometry and Flow Compressibility Effects on Wing and Blade Flutter. *AIAA Paper 98-0517*, 1998.

[28] K. D. Jones and M. F. Platzer. An Experimental and Numerical Investigation of Flapping-Wing Propulsion. *37th AIAA Aerospace Sciences Meeting and Exhibit*, January 11-14 1999. Reno, NV.

[29] R. Katzmayr. Effect of Periodic Changes of Angles of Attack on Behavior of Airfoils. Technical Report 147, NACA Report, October 1922. translated from Zeitschrift für Flugtechnik und Motorluftschiffahrt, March 31, pp. 80–82, and April 13, 1922, pp. 95–101.

[30] M. Khalid and M. Mokry. NPARC Study of Two-Dimensional Transonic Wall Interference. *Journal of Aircraft*, 33(5):906–912, September–October 1996.

[31] A. Knipfer, G. Schewe, and V. Wendt. Numerische und Experimentelle Undersuchungen an einem Schwingenden NLR 7301-Profil in Transsonischer Stroemung, Teil 1: Flattern und Erzwungene Schwingungen. Technical Report IB 232–98 J 05, DLR Bericht, 1998.

[32] R. Knoller. Die Gesetze des Luftwiderstandes. *Flug- und Motortechnik (Wien)*, 3(21):1–7, 1909.

[33] C. E. Lan. The Unsteady Quasi-Vortex-Lattice Method with Applications to Animal Propulsion. *Journal of Fluid Mechanics*, 93:747–765, 1979.

[34] T. C. Lund. Experimental and Computational Investigation of Flapping-Wing Propulsion for Micro-Air Vehicles. Master's thesis, Naval Postgraduate School, 2000.

[35] M. Mokry, Y. Y. Chan, and D. J. Jones. Two-Dimensional Wind Tunnel Wall Interference. Technical Report 281, AGARDograph, 0000.

[36] S. A. Morton and P. S. Beran. Hopf-Bifurcation Analysis of Airfoil Flutter at Transonic Speeds. *Journal of Aircraft*, 36(2):421–429, March–April 1999.

[37] C. K. Pang. A Computer Code for Unsteady Incompressible Flow past Two Airfoils. Aeronautical Engineer's thesis, Naval Postgraduate School, September 1988.

[38] J. Petree. Strange Attractor in Chaos Theory. [http://www.wfu.edu/˜petrejh4/Attractor.htm], 1999.

[39] M. M. Rai and S. R. Chakravarthy. An Implicit Form for the Osher Upwind Scheme. *AIAA Journal*, 24(5):735–743, May 1986.

[40] R. Ramamurti and W. Sandberg. Simulation of Flow about Flapping Airfoils Using Finite Element Incompressible Flow Solver. *AIAA Journal*, 39(2):253–260, February 2001.

[41] K. V. Rozhdestvensky. *Aerodynamics of a Lifting System in Extreme Ground Effect*. Springer, 2000. ISBN 3-540-66277-4.

[42] W. Sanz and M. F. Platzer. Numerical Investigation of the Stall Onset Behavior of the GA(W)-1 Airfoil. *Computers & Fluids*, 27(5–6):681–687, 1998.

[43] W. Sanz and M. F. Platzer. On the Navier-Stokes Calculation of Separation Bubbles with a New Transition Model. *Journal of Turbomachinery*, 120:36–42, January 1998.

[44] G. Schewe and H. Deyhle. Experiments on Transonic Flutter of a Two-Dimensional Supercritical Wing with Emphasis on the Non-Linear Effect. In *Proceedings of the Royal Aeronautical Society Conference on Unsteady Aerodynamics*, 1996. London.

[45] P. R. Spalart and S. R. Allmaras. A One–Equation Turbulence Model for Aerodynamic Flows. *AIAA Paper 92–0439*, January 6–9 1992. Reno, Nevada.

[46] J. L. Steger and R. F. Warming. Flux Vector Splitting of the Inviscid Gasdynamic Equations with Application to Finite-Difference Methods. *Journal of Computational Physics*, 40:263–293, 1981.

[47] Y. Tamura and K. Fujii. Conservation Law for Moving and Transformed Grids. *AIAA Paper 93-3365*, July 6–9 1993. Orlando, FL.

[48] T. Theodorsen. General Theory of Aerodynamic Instability and the Mechanism of Flutter. Technical Report 496, NACA, 1935.

[49] P. D. Thomas and C. K. Lombard. Geometric Conservation Law and Its Application to Flow Computations on Moving Grids. *AIAA Journal*, 17(10):1030–1037, October 1979.

[50] I. H. Tuncer and M. Kaya. A Computational Study of Flapping Airfoils in Biplane Configuration. Submitted to the 7th International Congress of Fluid Dynamics and Propulsion, Dec. 19-21, 2001.

[51] I. H. Tuncer and M. F. Platzer. Thrust Generation due to Airfoil Flapping. *AIAA Journal*, 34(2):324–331, February 1996.

[52] I. H. Tuncer and M. F. Platzer. A Computational Study of Flow Separation Characteristics and Wake Profiles behind a Flapping Airfoil. *37th AIAA Aerospace Sciences Meeting and Exhibit*, January 11-14 1999. Reno, NV.

[53] I. H. Tuncer, R. Walz, and M. F. Platzer. A Computational Study on the Dynamic Stall of a Flapping Airfoil. *16th AIAA Applied Aerodynamics Conference - AIAA-98-2519*, pages 219–225, Jun. 15-18 1998. Albuquerque, New Mexico.

[54] S. Weber, H. Benetschik, D. Peitsch, and H. E. Gallus. A Numerical Approach to Unstalled and Stalled Flutter Phenomena in Turbomachinery Cascades. *ASME International Gas Turbine & Aeroengine Congress & Exhibition*, June 2-5 1997. Orlando, Florida.

[55] S. Weber, K. D. Jones, J. A. Ekaterinaris, and M. F. Platzer. Transonic Flutter Computations for a 2-D Supercritical Wing. *37th AIAA Aerospace Sciences Meeting and Exhibit*, January 11-14 1999. Reno, NV.

INITIAL DISTRIBUTION LIST

1. Defense Technical Information Center

   Fort Belvoir, Virginia

2. Dudley Knox Library

   Naval Postgraduate School

   Monterey, California

3. CTA/IAE/ASB

   Sao Jose dos Campos - SP - Brazil

   everton@iae.cta.br

4. CTA/ITA Biblioteca

   Sao Jose dos Campos - SP - Brazil

   iab@bibl.ita.cta.br

5. Prof. Max F. Platzer

   Chair, Department of Aeronautics & Astronautics - Naval Postgraduate School

   platzer@aa.nps.navy.mil

6. Prof. Oscar Biblarz

   Department of Aeronautics & Astronautics - Naval Postgraduate School

   biblarz@aa.nps.navy.mil

7. Prof. Garth Hobson

   Department of Aeronautics & Astronautics - Naval Postgraduate School

   garth@aa.nps.navy.mil

8. Prof. Clyde Scandrett

   Department of Mathematics - Naval Postgraduate School

   cscand@nps.navy.mil

9. Prof. Kevin D. Jones

   Department of Aeronautics & Astronautics - Naval Postgraduate School

   jones4@aa.nps.navy.mil

10. Prof. John A. Ekaterinaris

    Foundation for Research & Technology Hellas - Greece

    ekaterin@iacm.forth.gr

11. Dr. Stefan Weber

    MTU Aero Engine Design - Germany

    stefan.weber@muc.mtu.de